ELECTRON POSITRON ANNIHILATION INTO GAMMA RAYS AT THE PETRA ACCELERATOR

Stephen Francis Yarker

A thesis presented for the Degree of Doctor of Philosophy in the University of London.

Imperial College

April 1983

ABSTRACT

This thesis describes an experiment at the electron positron storage ring PETRA, using the TASSO spectrometer.

The spectrometer is described and a detailed description of the construction and performance of the lead-scintillator shower counters is given.

The QED reactions $e^+e^- \to e^+e^-$ and $e^+e^- \to \gamma\gamma$ are analysed at centre of mass energies in the range $12 \leq W \leq 36.6$ GeV. A comparison of the data with the predictions of QED is made.

PREFACE

The experiment described in this thesis was performed by a collaboration of physicists from Aachen, Bonn, DESY, Hamburg, Imperial College, Oxford, Rutherford, Weizmann and Wisconsin, using the TASSO spectrometer. The author became a research student at Imperial College in October 1978 and worked with this group at DESY from July 1979, returning to Britain in February 1981 to analyse the data.

The author was not involved in the general planning of the experiment but was involved with the construction, installation, commissioning and some of the testing of the lead-scintillator shower counters and subsequently in the off-line analysis of experimental data.

Chapter 1 contains a brief summary of the physics studied in e^+e^- interactions. This is followed by a description of the PETRA accelerator and the TASSO spectrometer in Chapter 2 and by a description of the trigger system, data acquisition system and the off-line data reduction procedures in Chapter 3. The authors contribution starts in Chapter 4 with a description of the shower counters. Chapter 5 is a short chapter listing the separate data reduction procedures used for the shower counters and the liquid argon barrel counters. The analysis of Bhabha scattering ($e^+e^- \rightarrow e^+e^-$) is presented in Chapter 6 and the analysis of electron positron annihilation into gamma rays ($e^+e^- \rightarrow \gamma\gamma$) is presented in Chapter 7.

CONTENTS

		Page
ABSTRACT		1
PREFACE		2
CONTENTS		3
CHAPTER 1	INTRODUCTION	6
	1.1 Introduction	6
	1.2 Hadron production	6
	1.3 Heavy lepton production	8
	1.4 Photon-Photon scattering	8
	1.5 Quantum electrodynamics	9
	1.6 Electroweak effects	9
	1.7 Bhabha scattering	10
	1.8 Pair annihilation into gamma rays	11
CHAPTER 2	THE PETRA ACCELERATOR AND THE TASSO DETECTOR	19
	2.1 Introduction	19
	2.2 PETRA	19
	2.3 Machine dependent backgrounds	21
	2.4 The TASSO coordinate system	23
	2.5 The TASSO detector	23
CHAPTER 3	TRIGGER SYSTEM, DATA ACQUISITION AND OFFLINE DATA REDUCTION	36
	3.1 Introduction	36
	3.2 Trigger system	36
	3.3 DATA acquisition system	40
	3.4 Off-line data reduction	41

			Page
CHAPTER 4	SHOWER COUNTERS		49
	4.1	Introduction	49
	4.2	Physics motivation	49
	4.3	Design requirements	49
	4.4	The "Wavelength shifting" technique	50
	4.5	Description of the shower counter	52
	4.6	Position of the counters in TASSO	56
	4.7	Granularity of the shower counters	56
	4.8	Electronics	57
	4.9	Online calibration of the shower counters	59
	4.10	Offline calibration of the shower counters	61
	4.11	Tests and performance	61
CHAPTER 5	SHOWER COUNTER AND LABC ANALYSIS ROUTINES		77
	5.1	Introduction	77
	5.2	Shower counter analysis package	77
	5.3	LABC analysis package	81
CHAPTER 6	BHABHA SCATTERING		85
	6.1	Introduction	85
	6.2	Event selection	89
	6.3	Background estimation	91
	6.4	Monte Carlo simulation of Bhabha scattering	92
	6.5	Data analysis	95
	6.6	Conclusions	98

		Page
CHAPTER 7	ELECTRON POSITRON ANNIHILATION INTO GAMMA RAYS	115
	7.1 Introduction	115
	7.2 Data selection	119
	7.3 Background estimation	123
	7.4 Selection of Bhabha events	126
	7.5 Shower counter geometrical acceptance	127
	7.6 Shower counter trigger efficiency	128
	7.7 Monte Carlo simulation of class A events	128
	7.8 Monte Carlo simulation of class B events	131
	7.9 Data analysis	132
	7.10 Conclusions	137
APPENDIX A	SIMULATION OF ELECTROMAGNETIC SHOWERS	161
APPENDIX B	PHOTON RECONSTRUCTION PROGRAM	165
APPENDIX C	MEMBERS OF THE TASSO COLLABORATION	168
REFERENCES		170
ACKNOWLEDGEMENTS		175

CHAPTER 1

INTRODUCTION

1.1 Introduction

In recent years the study of e^+e^- annihilation processes has provided a great deal of information on the fundamental constituents of matter and their interactions[1]. The reason for this is that e^+e^- annihilation proceeds via the exchange of a time like virtual photon which can couple to all flavours of quarks and leptons, which are produced at comparable rates.

The importance of the results obtained from e^+e^- experiments has led to a rapid growth in the number and size of e^+e^- machines. Table 1.1 gives a summary of past, present and future e^+e^- colliders.

In this chapter a brief summary of the physics studied in e^+e^- interactions is given. Bhabha scattering and electron-positron annihilation into gamma rays are also discussed.

1.2 Hadron production

Hadron production proceeds via the one photon annihilation channel, shown in Fig 1.1. The intermediate virtual photon has the quantum numbers ($J^{PC} = 1^{--}$) and can couple directly to vector mesons which have the same quantum numbers. At centre of mass energies, W, below ~ 1 GeV the cross-section is dominated by the production of ρ, ω and ϕ mesons[2]. At higher energies, W ~ 5 GeV the total cross-section was found to have a very weak energy dependence. The discovery of the J/ψ at BNL[3] and SPEAR[4] at a mass of 3.1 GeV and of related states at higher energies[5] was explained by interpreting the new states as bound $Q\bar{Q}$ systems of a new heavy quark Q. The most natural choice was to identify Q with the charmed quark c, which had been proposed to achieve symmetry between quarks and leptons[6] and to explain the absence of strangeness changing

neutral currents via the GIM mechanism[7]. This was verified by the later observation of states with open charm[8]. After the discovery at SPEAR of the tau lepton[9] a third generation of quarks was expected to achieve symmetry between quarks and leptons. The discovery of the Υ at FNAL[10] and the observation of related states at DORIS[11] and CESR[12] was interpreted as due to the bottom quark b of this third generation. The top quark t the partner of the b quark has yet to be discovered and it is hoped that it will soon be observed at PETRA.

In the quark-parton model hadron production proceeds by the production of a quark-antiquark pair where the quarks subsequently fragment into jets of hadrons, Fig 1.1. Evidence for jets was first obtained at SPEAR[13] by studying the topology of events using the quantity sphericity (S). At PETRA/PEP energies the jets of hadrons are clearly visible, Fig 1.2 shows a 2-jet event observed in the TASSO detector. Any field theory of the interactions of quarks must incorporate field quanta 'gluons'. A prediction of the theory is that a small fraction of events will have hard gluon radiation, Fig 1.3, which leads to planar events with three well separated hadron jets. At PETRA 3-jet events were observed for the first time[14] and Fig 1.4 shows a 3-jet event observed in the TASSO detector. Detailed measurements including a measurement of the gluon spin[15] (= 1) are consistent with QCD[16] the favoured theory of the strong interaction.

The cross-section for $e^+e^- \rightarrow$ hadrons is expressed through the quantity R

$$R = \frac{\sigma(e^+e^- \rightarrow \text{hadrons})}{\sigma(e^+e^- - \mu^+\mu^-)} = 3 \sum_{i=1,5} q_i^2 \left(1 + \frac{\alpha_s}{\pi}\right) \qquad - 1.2.1$$

where q_i is the charge of quark i. The factor 3 arises from colour and the factor $(1 + \frac{\alpha_s}{\pi})$ is the lowest order QCD correction which arises from gluon bremsstrahlung. Fig 1.5 shows the value of R as a function of

centre of mass energy W. Assuming five quark flavours and including first order QCD corrections the value of R at W = 20 GeV is predicted to be 3.92 which agrees well with the measured value of R = 3.97 ± 0.06[17].

Evidence that the partons produced in e^+e^- annihilations are charged has come from the observation of long range charge correlations in hadronic final states[18].

1.3 Heavy lepton production

At the e^+e^- storage ring SPEAR a new lepton, the tau, with a mass of 1.782 GeV/c^2 was discovered[9] through the observation of an anomalous number of eμ events. The tau has been shown to behave as a standard sequential point like lepton[19].

Observation of a new charged lepton would indicate the presence of a new generation of fermions. No evidence has been found for a new sequential lepton of mass $\leq$ 17 GeV/c^2, scalar leptons have also been excluded with mass $\leq$ 16 GeV/c^2[20].

1.4 Photon-Photon scattering

Electron positron collisions are also a source of photon-photon scattering events, represented by the diagram shown in Fig 1.6. The first events were seen at ADONE[21] and some measurements were obtained at DORIS and SPEAR[22]. Although the process is of order (α^4) it becomes increasingly important at high energy as its cross-section depends logarithmically on beam energy W/2 whereas the cross-section for 1-γ annihilation processes depends on $1/W^2$. Both Hadronic final states and lepton-antilepton pairs can be produced. Hadrons with even charge conjugation can be produced[23].

Resonance[22,24] and continum[25] production have been studied and the reaction $\gamma\gamma \rightarrow \rho^0\rho^0$ has been observed[26]. The photon structure function has been measured and measurements of jet production in photon-photon scattering events have been reported[27].

1.5 Quantum electrodynamics

Quantum electrodynamics (QED), the theory of the electromagnetic interaction of leptons and photons has been tested and verified by a wide variety of experiments[28].

At low momentum transfers QED has been tested by measurements of the anomalous magnetic moment of the electron[29] and muon[30].

Using storage rings the theory has been tested at high momentum transfers by measurements of Möller scattering ($e^-e^- \rightarrow e^-e^-$), Bhabha scattering ($e^+e^- \rightarrow e^+e^-$), muon and tau pair production ($e^+e^- \rightarrow \mu^+\mu^-$ ($\tau^+\tau^-$)) and electron positron annihilation into gamma rays ($e^+e^- \rightarrow \gamma\gamma$). The first result, a measurement of the cross-section for Möller scattering was published in 1966[31]. Measurements at high momentum transfer test the assumption that leptons are pointlike particles without excited states. Results obtained before the advent of PETRA[32] confirmed that leptons are pointlike to distances of $\sim 4 \times 10^{-15}$ cm. At PETRA QED has been tested up to momentum transfers ($Q^2 \sim 1300$ GeV^2)[33] confirming that leptons are pointlike to distances of $\sim 2 \times 10^{-16}$ cm. No significant deviations from the theory have been observed.

1.6 Electroweak effects

At the highest PETRA energies effects caused by the interference of the weak and electromagnetic currents start to be visible. The weak interaction contributes to the QED processes and to hadron production through diagrams involving the exchange of the Z^0 boson, shown in Fig 1.7. The weak contribution changes the cross-section for lepton pair production and leads to a forward-background asymmetry in the angular distribution of the final state leptons. The change in the cross-section for the standard model[34] is too small to be observed at present energies ($\Delta\sigma/\sigma \approx 0.5\%$ for $\sin^2 \theta_W = 0.23$)[35], but the asymmetry is measurable. Measurements of the asymmetry are consistent with the prediction obtained from the standard

model. Combined data have been used[36] to determine the leptonic weak coupling constants g_V^2 and g_A^2 and to determine $\sin^2\theta_W$, where θ_W is the free parameter of the standard model. The standard model can be extended[37] to models[38] based on an enlarged symmetry group, which differ from the standard model by having more than one neutral weak boson. The combined data have been used to place lower limits on the masses of such bosons[36].

1.7 Bhabha scattering

The lowest order diagrams contributing to Bhabha scattering are shown in Fig 1.8, where Fig 1.8 b) represents the exchange of a time like and Fig 1.8 a) represents the exchange of a space like virtual photon respectively. Higher order (α^3) diagrams shown in Fig 1.9 modify the lowest order (α^2) cross-section. In particular the initial state radiation and large angle final state radiation corrections lead to an acollinearity of the final state electron and positron.

At PETRA energies the point like nature of the electron can be tested to the maximum available momentum transfer $Q^2 \sim 1300\ \text{GeV}^2$ through a measurement of the cross-section, $\frac{d\sigma}{d\Omega}(e^+e^- \to e^+e^-)$. The Q^2 available at PETRA is much greater than the Q^2 available for previous QED tests at SPEAR and DORIS[33] ($Q^2 \sim 50\ \text{GeV}^2$) allowing more stringent limits to be set.

Additional diagrams shown in Fig 1.10 arise from the weak interaction through Z^0 exchange. At the maximum PETRA energies the corrections from these diagrams are ~ 1-2%[39]. The weak contributions to the cross-section depend on s in comparison to the QED contributions which depend on $^1/s$ and will eventually dominate the cross-section at sufficiently high energies[40]. The angular distribution[41] can be used to obtain information on the weak coupling constants.

1.8 Electron-Positron annihilation into gamma rays

The lowest order diagrams contributing to the annihilation of an electron and a positron into gamma rays are shown in Fig 1.11. In contrast to the reactions $e^+e^- \to l\bar{l}$ ($l = e,\mu,\tau$), mediated by the exchange of a virtual photon, the reaction $e^+e^- \to \gamma\gamma$ involves the exchange of a virtual electron. Both diagrams are required by Bose statistics to make the total amplitude symmetric to the interchange of the two photons. Higher order (α^3) diagrams shown in Fig 1.12 modify the cross-section with the initial state radiation correction leading to an acollinearity of the final state photons. In some cases the 3 photons are sufficiently energetic to be observable. A measurement of the 3 photon final state enables QED to be tested to order (α^3) at large Q^2.

At PETRA energies tests of QED can be made through a measurement of the cross-section, $\frac{d\sigma}{d\Omega}$ ($e^+e^- \to \gamma\gamma$), to the maximum available momentum transfer $Q^2 \sim 1300$ GeV^2[33]. The cross-section can be used to search for the presence of "seagull diagrams"[42], or for the existence of an excited electron as the exchange particle[43]. The electron propagator is not tested by this reaction, it can only be tested through closed loop effects[42].

The reaction ($e^+e^- \to \gamma\gamma$) can be used to test QED at higher energies in a more direct way as it does not involve additional electroweak interference contributions in contrast to the reactions $e^+e^- \to l\bar{l}$ ($l = e,\mu,\tau$). In this reaction the weak interaction does not contribute to the lowest order (α^2) and higher order (α^3) cross-section[44] and neither does hadron vacuum polarisation.

Name	Location	first beams	maximum beam energy (GeV)
AdA	Frascati	1961	0·25
Princeton-Stanford	Stanford	1962	0·55
ACO	Orsay	1966	0·55
VEPP-2	Novosibirsk	1966	0·55
ADONE	Frascati	1969	1·55
BYPASS	Cambridge (USA)	1970	3·50
VEPP-3	Novosibirsk	1970	3·50
SPEAR	Stanford	1972	3·90
DORIS	Hamburg	1974	5·00
VEPP-2M	Novosibirsk	1975	0·67
DCI	Orsay	1976	1·80
PETRA	Hamburg	1978	19·00
CESR	Cornell	1979	8·00
VEPP-4	Novosibirsk	1979	5·50
PEP	Stanford	1980	18·00
SLC	Stanford	(1985)	50·00
LEP	Geneva	(1986)	130·00
TRISTAN	KEK	(1986)	30·00
Cornell 50×50	Cornell	(1986)	50·00
VLEPP	Novosibirsk	(1989)	300·00

Table 1·1 past, present and proposed high energy e^+e^- colliders

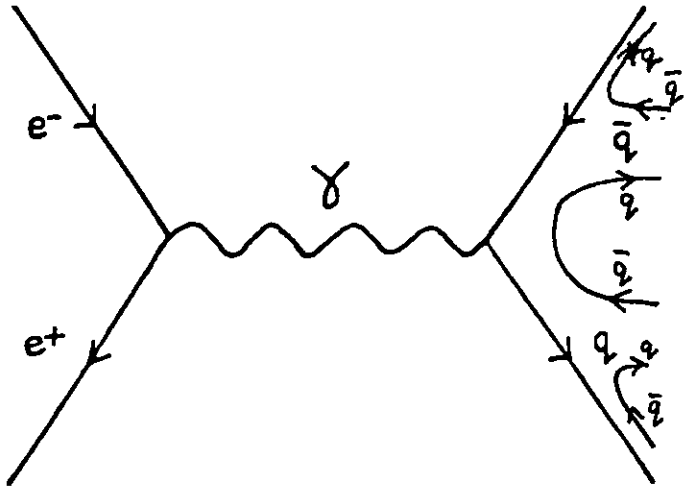


Fig 1·1 hadron production via the one photon annihilation channel

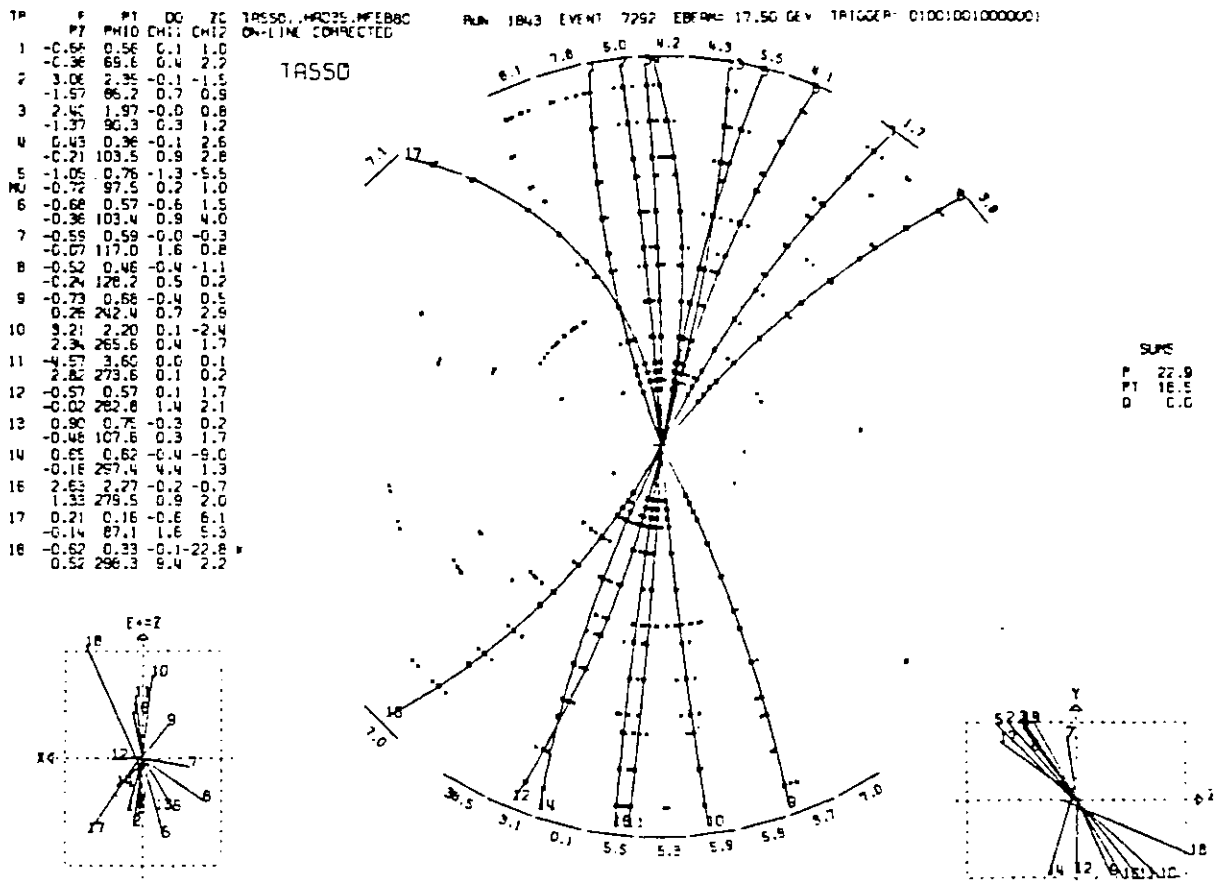


Fig 1·2 two-jet event observed with the TASSO detector

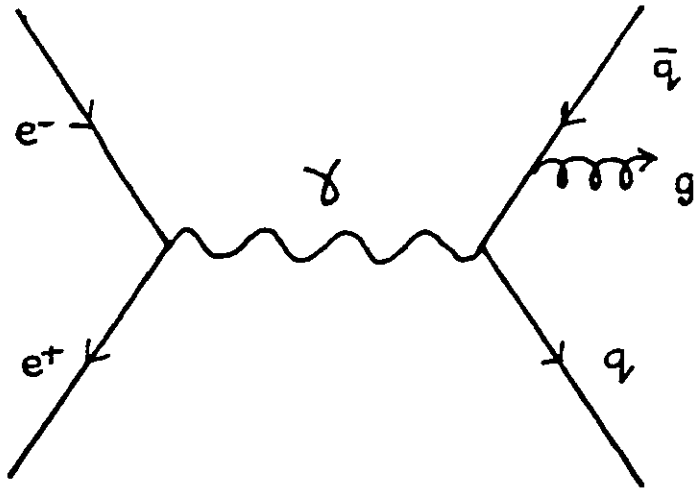


Fig 1·3 hadron production via the one photon annihilation channel with hard gluon bremsstrahlung in the final state

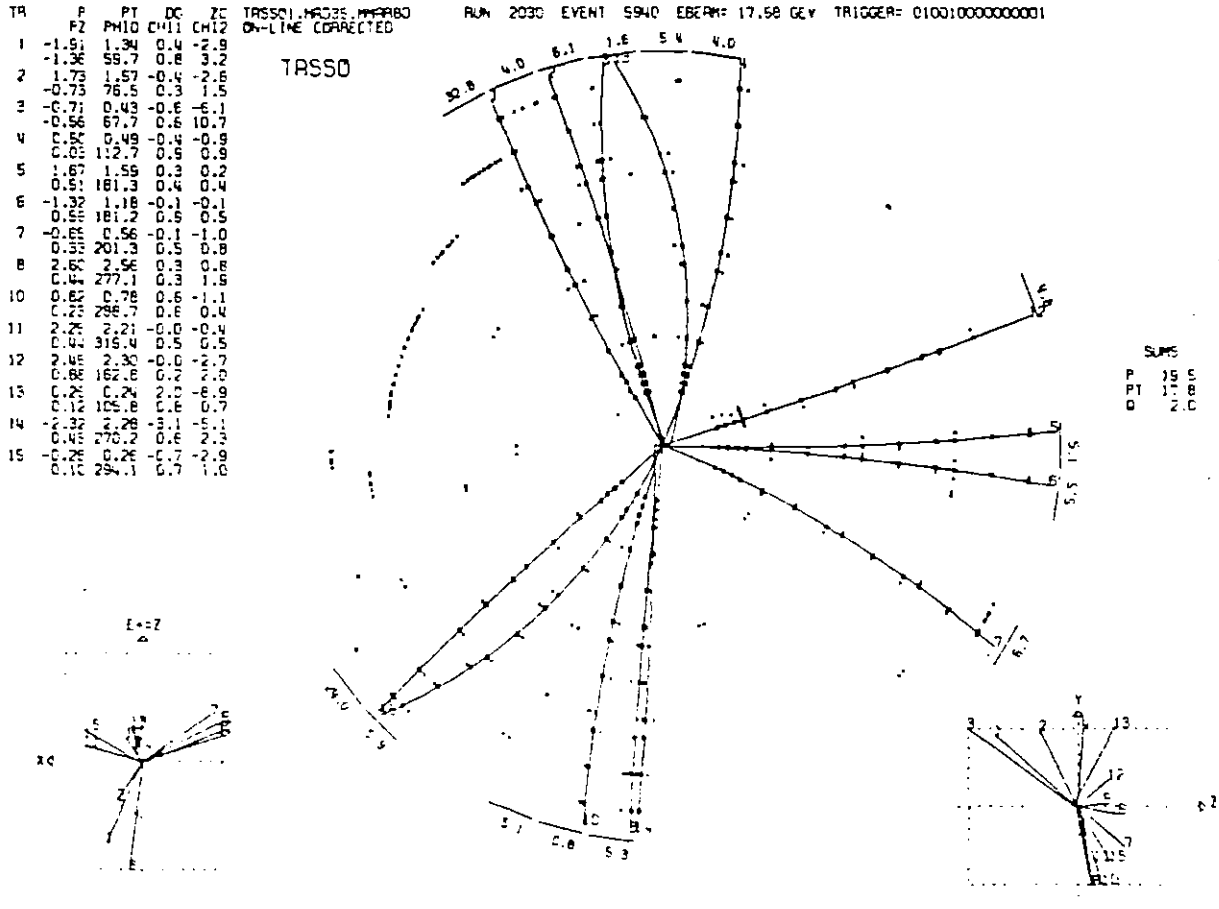


Fig 1·4 three-jet event observed with the TASSO detector

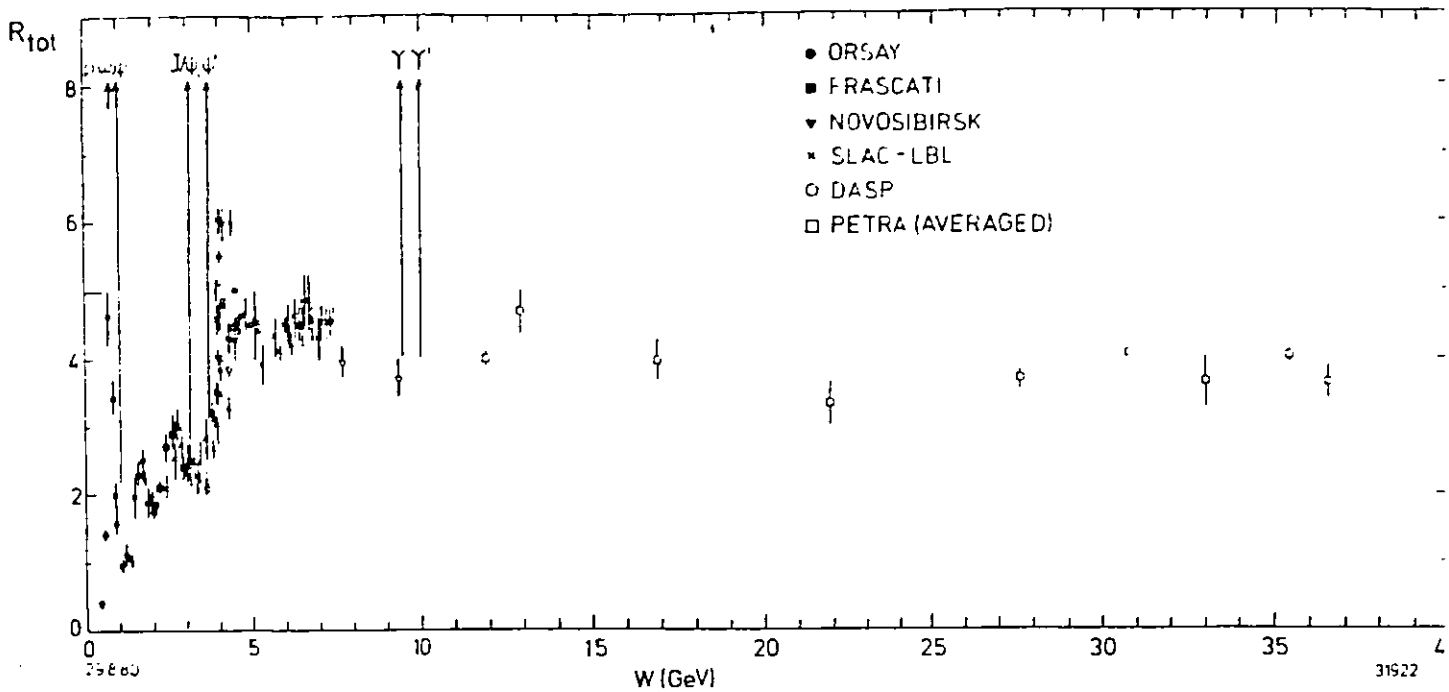


Fig 1·5 total cross-section, R, v. centre of mass energy, W

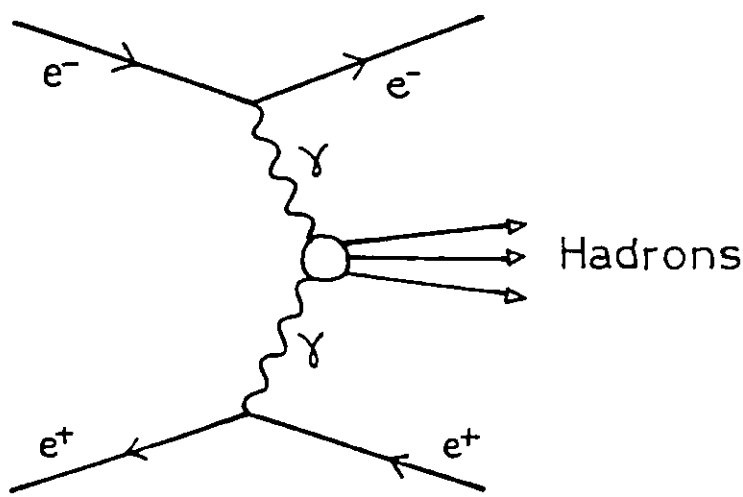


Fig 1·6 hadron production via photon-photon scattering

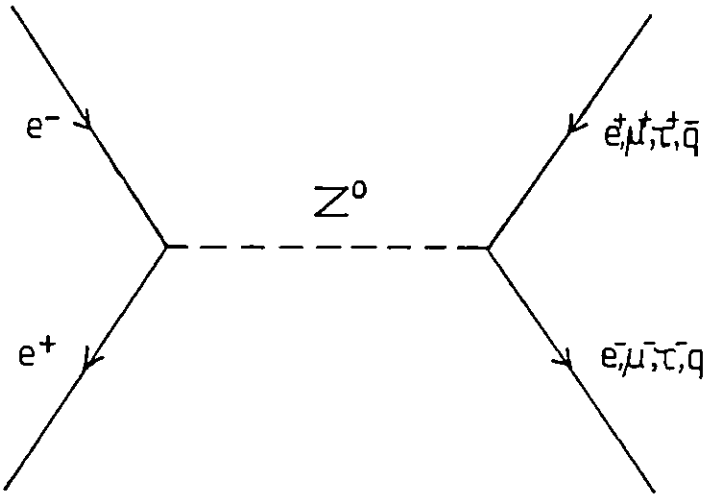


Fig 1·7 fermion-antifermion production mediated by the Z^0 boson

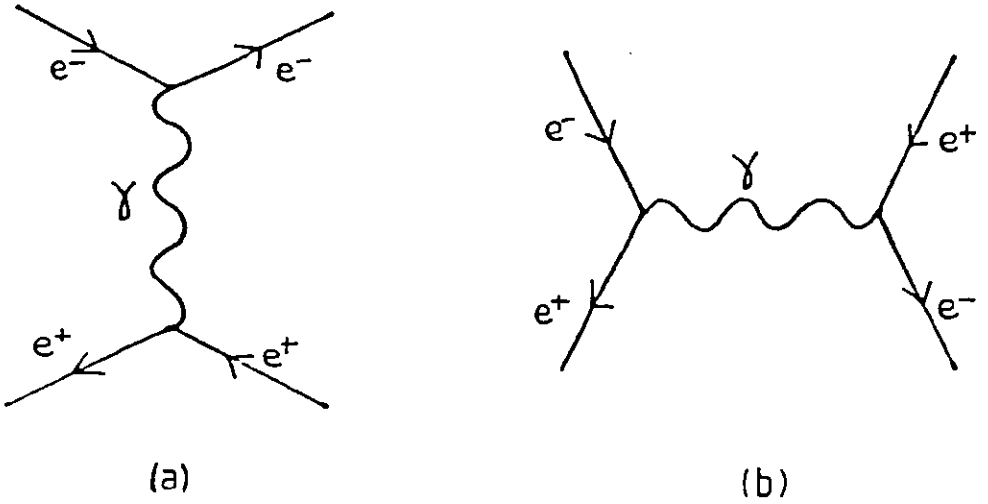


Fig 1·8 lowest order diagrams for Bhabha scattering

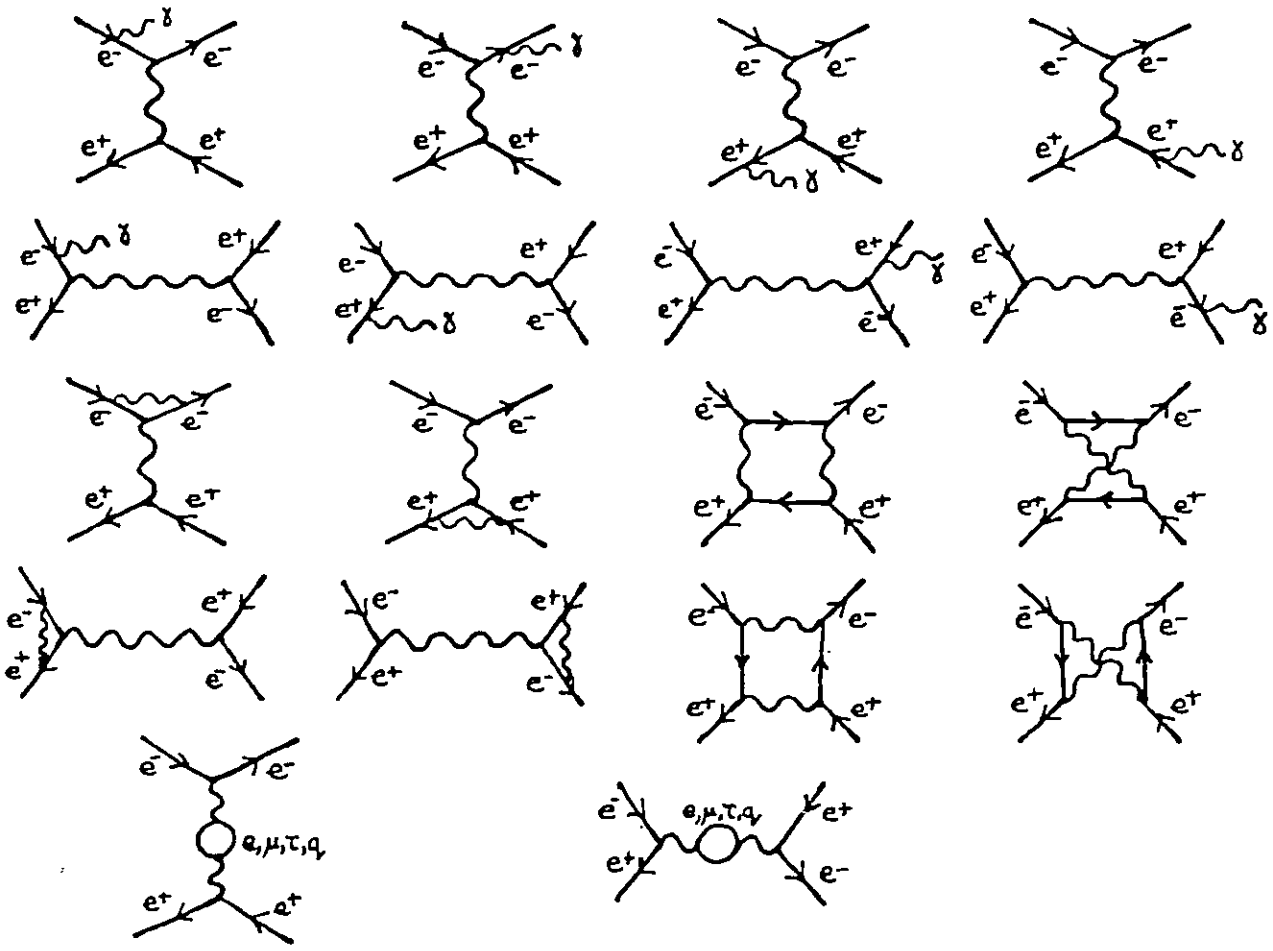


Fig 1·9 higher order diagrams for Bhabha scattering

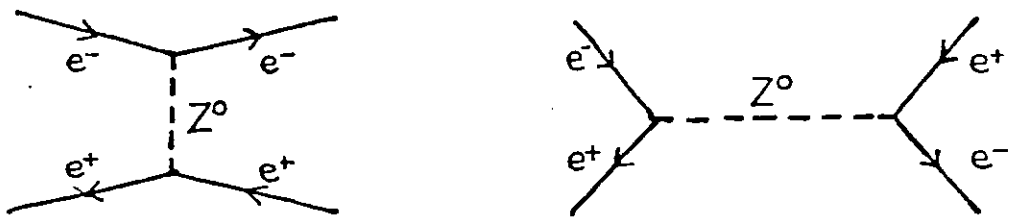


Fig 1·10 lowest order diagrams for Bhabha scattering mediated by the Z^0 boson

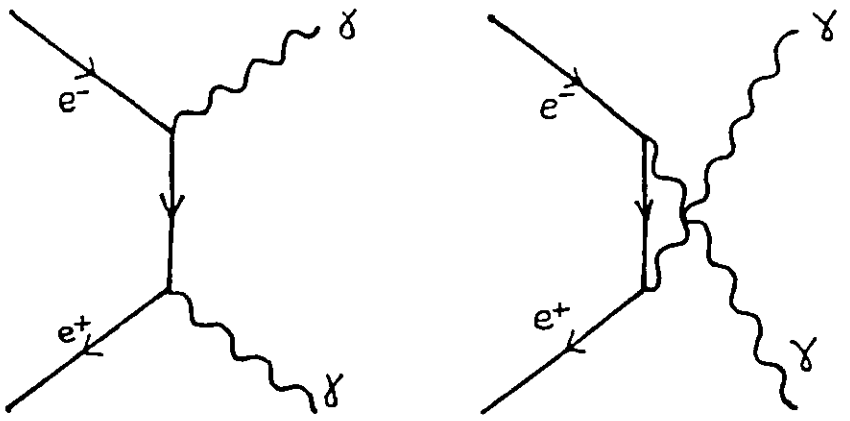


Fig 1·11 lowest order diagrams for electron-positron annihilation into gamma rays

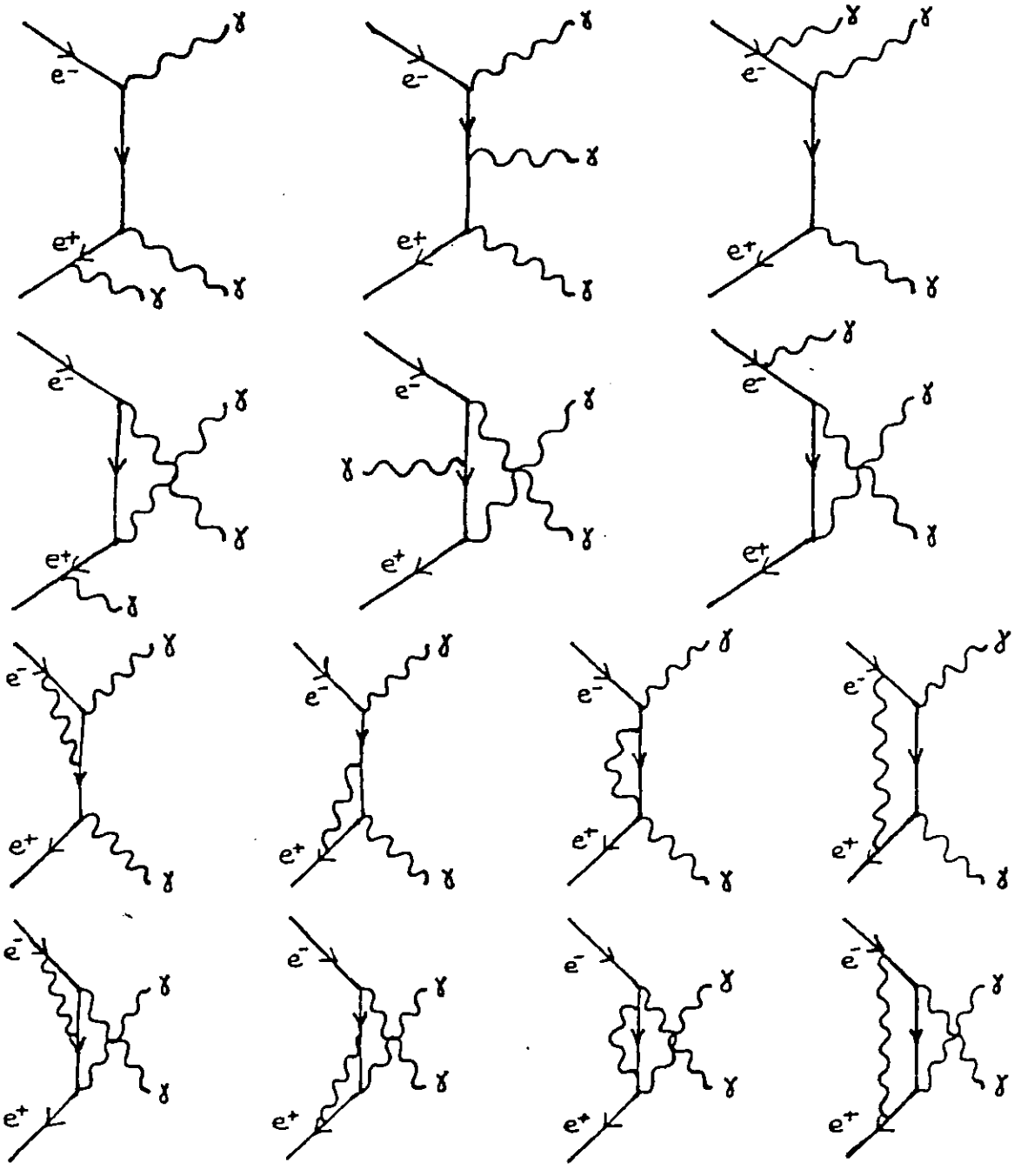


Fig 1·12 higher order diagrams for electron-positron annihilation into gamma rays

CHAPTER 2

THE PETRA ACCELERATOR AND THE TASSO DETECTOR

2.1 Introduction

The electron positron storage ring PETRA and the TASSO detector are described in this chapter.

2.2 PETRA

The PETRA† accelerator[45], shown in Fig 2.1, is designed to store circulating beams of electrons and positrons at high energies. It has a circumference of 2.3 km and consists of 8 bending regions separated by straight sections. The bending regions have a radius of 256 m and maintain the beam particles orbit within the vacuum chamber. Electrostatic separators which are installed on each side of the straight sections enable a separation of the beams at the interaction points during injection and acceleration.

The circulating beams consist of bunches of particles with dimensions of $(\sigma_x,\sigma_y,\sigma_z) \simeq 0.1 \times 0.01 \times 1.0\ cm^3$. PETRA is designed to operate with a maximum of 4 particle bunches in each beam which allows interactions to take place at up to 8 intersection regions.

The energy to accelerate the beams and to replace the energy lost by synchrotron radiation is supplied from radio frequency (R.F.) cavities which are installed at the north and south straight sections. Eight klystrons each supply a maximum of 600 kW to 64 cavities driven at 500 MHz. A maximum energy of ~ 19 GeV was expected with the available power, but so far only a maximum energy of 18.3 GeV has been attained.

The vacuum chamber is maintained at a pressure of 5×10^{-9} Torr. A low pressure is essential as collisions between beam particles and gas molecules inside the vacuum chamber produce background in the interaction regions and limit the lifetime of the beams. Pressures smaller than 5×10^{-9} Torr are difficult to achieve as synchrotron radiation causes

† (Positron Electron Tandem Ring Accelerator)

outgassing of gas molecules trapped in the surface layer of the vacuum chamber.

2.2.1 Luminosity

The event rate for a cross-section σ is given by

$$N = \frac{n^+ n^- f B \sigma}{F} \qquad - 2.2.1$$

where $n^+(n^-)$ is the number of positrons (electrons) per bunch, B is the number of bunches per beam, f is the rotation frequency and F is the beam cross-section.

The luminosity L is then defined to be

$$L = N/\sigma \quad cm^{-2}\ sec^{-1} \qquad - 2.2.2$$

Expressing the number of particles $n^+(n^-)$ in terms of the beam currents $i^+(i^-)$, where e is the electron charge and

$$i = nefB \qquad - 2.2.3$$

$$L = \frac{i^+ i^-}{e^2 FfB} \qquad - 2.2.4$$

The luminosity is maximised by having the largest possible beam currents and the smallest possible beam cross-section at the interaction points.

The luminosity depends strongly on energy. At low beam energies it is limited by beam-beam interactions and increases with beam energy with an energy dependence like E^4. The maximum luminosity is reached when the energy loss through synchrotron radiation has reached the limit of available power and above this energy it falls rapidly with an energy dependence like E^{-10}.

With PETRA operating at beam energies around 15 GeV a peak differential luminosity of 3×10^{-31} cm^2 sec^{-1} and bunch currents of 5 mA were achieved, with an average differential luminosity over a single run of 1.5×10^{-31} cm^2 sec^{-1}.

2.3 Machine Dependent Backgrounds

2.3.1 Synchrotron Radiation

Synchrotron radiation is produced when charged particles are deflected and therefore accelerated by magnetic fields. In PETRA the beam particles radiate a large flux of low energy photons as they pass through the bending and focusing magnets of the ring. The main sources of synchrotron radiation seen at the interaction point are the final bending magnets and the strong focusing quadrupole magnets on each side of the interaction point. The final two bending magnets in each of the bending regions on each side of the interaction point have a smaller magnetic field, 83% and 17% of the magnetic field of the remaining bending magnets. This reduces the sychrotron radiation background from the final two bending magnets as the characteristic energy of the photons produced there is reduced. The usefulness of this technique is limited by the large flux caused by the interaction region quadrupole magnets, in particular a poor beam position here results in a large rate.

Synchrotron radiation photons interact by compton scattering and the photoelectric effect producing electrons which cause random hits in the detector. There is no evidence that synchrotron radiation results in a significant data taking rate.

2.3.2 Beam Gas Scattering

Beam gas scattering is the interaction of beam particles with the residual gas molecules that remain in the vacuum chamber and the interaction rate is therefore dependent on their density and on the number of beam particles.

Beam gas scattering occurs along the whole length of the vacuum chamber and so the rate seen by any detector also depends on the length enclosed by the detector.

There are several characteristic features of these events. They

have:

a) a small visible energy, much less than the beam energy

b) a net positive charge, this is due to interactions with protons of the gas nuclei

c) a low multiplicity

d) the tracks are in one hemisphere with the summed momentum vector close to the beam axis

e) the interaction vertex can be anywhere along the beam axis.

As these events have small visible energy they are easily separated from hadronic events due to one photon annihilation, but are not always distinguishable from photon-photon scattering events.

The background from beam gas scattering can be estimated by observing the number produced at large distances from the interaction point along the beam direction and extrapolating to the interaction region assuming a flat background. These events trigger TASSO at $\lesssim$ 0.1 Hz.

A beam gas scattering event is shown in Fig 2.2.

2.3.3 Beam pipe interactions

Beam pipe interactions occur when a beam particle loses energy by beam gas bremsstrahlung and enters an unstable orbit. Eventually it will strike the wall of the vacuum chamber producing a shower of particles.

There are several characteristics of these interactions:

a) the vertex is off axis and can occur at large distances from the interaction point along the beam direction

b) a net positive charge is observed

c) most of the particles are produced in one z-direction

d) there is a high number of secondary particles produced.

As the vertex is off axis many of the tracks of produced particles will not reconstruct to the interaction point and consequently have larger values of the fitting parameters† d_0 and z_0 than tracks from the

† these parameters are defined in section 3.4.2

interaction point.

The TASSO trigger rate for this process is ~ 0.5 Hz. A beam pipe interaction event is shown in Fig 2.3.

2.4 The TASSO coordinate system

The beam beam intersection point is defined as the origin of coordinates. The z-axis is defined as the direction of the positron beam in the accelerator, the x-axis is in the plane of the accelerator directed inwards from the origin to the centre and the y-axis is normal to the accelerator plane directed upwards from the origin. The x,y and z axes form a right handed coordinate system which is shown in Fig 2.4.

2.5 The TASSO detector

The two arm spectrometer solenoid (TASSO)[46] detector is designed to detect particles produced by high energy electron positron collisions. There are three parts of the detector, the central and forward detectors and the hadron arms.

The central detector consists of a 4 layer cylindrical proportional chamber, a 15 layer cylindrical drift chamber and a layer of time of flight counters enclosed in a conventional solenoidal magnet, to measure charged particle momenta and to provide some particle identification. Lead-liquid argon calorimeters provide information on the energy of electrons and detect photons.

The forward detector comprises two identical modules on either side of the interaction point, each consists of a lead glass shower counter and scintillation counters. It is used to monitor luminosity and to tag electrons from photon photon scattering events.

Each hadron arm consists of a planar drift chamber to detect particles leaving the magnet coil followed by 3 different threshold cerenkov counters and a time of flight counter array for detailed particle identification. A lead-scintillator shower counter array follows to detect photons and

measure the energy of electrons.

The flux return yoke of the solenoid and an iron wall supporting the time of flight and shower counters in each hadron arm act as hadron absorbers behind which muons are identified using proportional tube arrays.

The TASSO detector is shown in Fig 2.5.

A brief description of the individual components is given below.

2.5.1 Beam pipe

The vacuum chamber at the interaction point is a 4mm thick, cylindrical aluminium pipe of radius 13 cm. At either end of the detector the beam pipe expands into large cones, which minimise the amount of material a particle passes through before reaching the forward detector. Cooling pipes and 4 quadrant scintillation counters surround the beam pipe, the scintillation counters are not used during data taking runs.

2.5.2 Cylindrical proportional chamber (CPC)

The CPC[47] consists of 4 concentric layers, each consisting of a 480 wire anode plane spaced equally between 2 cathode planes of 120 helical copper strips. The anode wires provide information on tracks in the R-ϕ plane while the cathode strips provide information on the Z coordinate of tracks. The CPC has a low mass construction to minimise photon conversions and the multiple scattering of particles passing through it. The chamber has an active length of 140 cm and extends radially from 18 cms to 29 cms. The chamber uses a "magic gas" mixture.

2.5.3 Drift chamber (DC)

The cylindrical DC[48] contains 15 concentric layers of drift cells, it extends radially from 36.7 cm to 122.2 cm and has an active length of 323 cm. Nine layers have their sense wires parallel to the beam axis and provide information on tracks in the R-ϕ plane, while 6 layers have their sense wires at $\pm$ 4° with respect to the beam axis and provide information on the z coordinate of tracks.

There are a total of 2340 identical drift cells of radial dimension 1.2 cm and azimuthal dimension 3.2 cm. Each cell consists of a 30 μm sense wire and a triplet of 120 μm field wires.

The DC has been operated with a mixture of 90% Argon and 10% methane, and also a mixture of 50% Argon and 50% Ethane. The second gas mixture was adopted in preference to the first as the DC was found to draw a smaller current.

The DC is equipped with single hit electronics. The resolution of the DC was ~ 200μ.

2.5.4 Inner time of flight (ITOF) scintillation counters

48 scintillation counters line the inner wall of the coil at a radius of 132 cm, they have a length of 390 cm, a width of 17.4 cm and a thickness of 2 cm. Each counter is viewed at each end by a photomultiplier tube.

The ITOF counters are used in the experimental trigger and define the acceptance of the inner detector to be $|\cos\theta| < .83$. The resolution of the ITOF counters was 300 - 450 psec.

2.5.5 The magnet

The CPC and DC are enclosed by a solenoidal magnet of length 4.4 m, its aluminium wall is approximately 1.1 Xo thick with an inner radius of 1.35 m. The warm coil produces a maximum field of 4.9 kgauss axially in the +ve z-direction. The magnetic field deflects charged particles as they pass through the tracking chambers allowing a measurement of their momenta to be made.

The magnet flux return yoke consist of 60 cm thick laminated iron plates at each end of the coil and 80 cm thick iron bars at the top and bottom; it is open at both sides. Retractable plugs cut into the endplates allow easy access to components within the solenoid.

Two smaller solenoids are placed symmetrically about the main solenoid at a distance of 4.75 m with their fields arranged so that the total

integrated field along the beam axis is zero. The fields of the solenoid and the two compensating solenoids were mapped using a Hall probe; this showed that the field in the region covered by the central tracking chambers is uniform to ~ 6%.

During data taking the magnet is always run at full field strength.

2.5.6 Liquid Argon Barrel Calorimeter (LABC)

The LABC[49] is designed to identify electrons and photons and to measure their energies in the energy range 100 MeV to ~ 20 GeV. It consists of 4 modules each consisting of an argon tank that contains 2 stacks of lead, suspended in a vacuum tank. The LABC covers a solid angle of 42% of 4π steradian.

In each stack, of dimensions 398 x 95 x 45 cm^3, liquid argon is the active medium while lead plates serve as the electrodes and as the showering medium. The lead is arranged in towers of square cross-section, where a tower is a longitudinal group of plates which have their signals capacitively coupled together. Segmentation into towers aids the disentangling of closely spaced showers. The spatial location of showers is measured by layers of strip electrodes running through the towers in two orthogonal directions. Each stack is separated longitudinally into 2 regions to improve the efficiency for measuring low energy photons and to give a better electron hadron discrimination. In the front region the towers of dimension 7 x 7 cm^2 at a distance of 179 cm from the interaction point have a depth of 6.1 radiation lengths and cover a solid angle of 1.5 mster. In the back region the towers have a depth of 7.6 radiation lengths and cover a solid angle of 6 mster, where each back tower covers the same solid angle as the 4 front towers before it. The axes of the front and back towers are directed towards the interaction point. Each stack has 35 active layers, each consisting of 0.5 cm of liquid argon between 2 lead plates of thickness 0.2 cm.

The layers of strip electrodes are made from low density copper plated epoxy plates etched with a strip pattern where the strip width is 2 cm. Three layers of ϕ strips, at depths of 0.3, 1.7 and 3.1 radiation lengths and 2 layers of Z strips at depths of 1.7 and 3.1 radiation lengths are used, where the ϕ strips run parallel to the beam axis and the Z strips are orthogonal to the ϕ strips. The ϕ strips in each layer are electrically connected vertically in groups of 3, and the z strips are electrically connected vertically in groups of 2.

A separate system of z strips provides dE/dx information on particles entering the stack and detects interactions in the material of the detector before the stack. It consists of 2 layers of strips at a depth of 0.3 radiation lengths which are independently read out.

In an electron test beam an energy resolution of $\sigma/E = 0.16/\sqrt{E}$ for $E = 0.2$ GeV has been measured falling to $\sigma/E = 0.9/\sqrt{E}$ for $E > 0.8$ GeV[50], without extra material to simulate the material of the TASSO detector preceding it. The energy resolution for photons is comparable with this. The angular resolution for electrons of $E > 10$ GeV is $\sigma_\phi \simeq \sigma_\theta = 3$mrad.

2.5.7 Muon counters

Muons are identified if they penetrate a large thickness of iron and give signals in proportional tube arrays.

The Muon detector[51] consists of 4 layers of proportional tubes with a tube cross-section of 4 x 4 cm^2. The tubes are aligned in two orthogonal directions with 2 layers in each direction and are offset by 2 cm to give a position resolution of 6 mm. Eight separate arrays provide muon identification in 45% of 4π steradian.

For muons with momenta above 2 GeV/c a tagging efficiency of > 99% is measured when a requirement of 3 out of 4 layers firing within 3 standard deviations of the position of an extrapolated track is made. Below ~ 1 GeV/c muons do not penetrate the absorber.

2.5.8 Forward Detector and luminosity monitor

The Forward Detector[52] is designed to measure small angle (θ~50 mrad) Bhabha scattering with a high precision. At small angles the 4-momentum Q^2 is small and corresponds to a region where QED has been well established; the event rate is also large enough to provide a statistically significant measurement. The electrons and positrons from photon-photon scattering, which are produced predominantly at small angles, are also tagged by the forward detector.

The detector consists of 8 counter telescopes arranged symmetrically around the beam pipe in the verical and horizontal planes, 6 m from the interaction point, with 4 on each side of the interaction point. This arrangement means that to a good approximation the luminosity measurement is insensitive to the exact position of the interaction, which can vary on the positions of the beams and on the bunch size[53]. The detector is shown in Fig 2.6.

Each telescope consists of a small piece of scintillator 'A' to define acceptance, of dimension 4 x 16 cm^2 and a larger piece of scintillator 'C' of dimension 9 x 19 cm^2 in front of a matrix of 36 lead-glass shower counters 12 radiation lengths thick.

The signal for a Bhabha scattering event is a signal in counter 'A' in coincidence with the 'C' counter in the diagonally opposite telescope together with a large pulse height in both lead glass arrays. There are a total of 8 possible coincidences.

The geometrical acceptance of the system is 1.4 x 10^{-3} steradian.

For an average luminosity of 1.5 x 10^{30} cm^{-2} sec^{-1} a counting rate ~ 1 Hz is observed. The measured luminosity has radiative corrections of order (α^3) included and has a small statistical error; the systematic error in the luminosity measurement is estimated as ± 4%.

2.5.9 Endcap counters

Liquid Argon endcap calorimeters[54] and TOF counter arrays are installed at the endcap regions. These detectors will not be described as they were not used in the analysis described in this thesis.

2.5.10 Hadron Arms

The hadron arm shower counters are described in detail in chapter 4. The Cerenkov counters[55], hadron arm TOF counters[56] and planar drift chamber were not used in the analysis described in this thesis and will not be described.

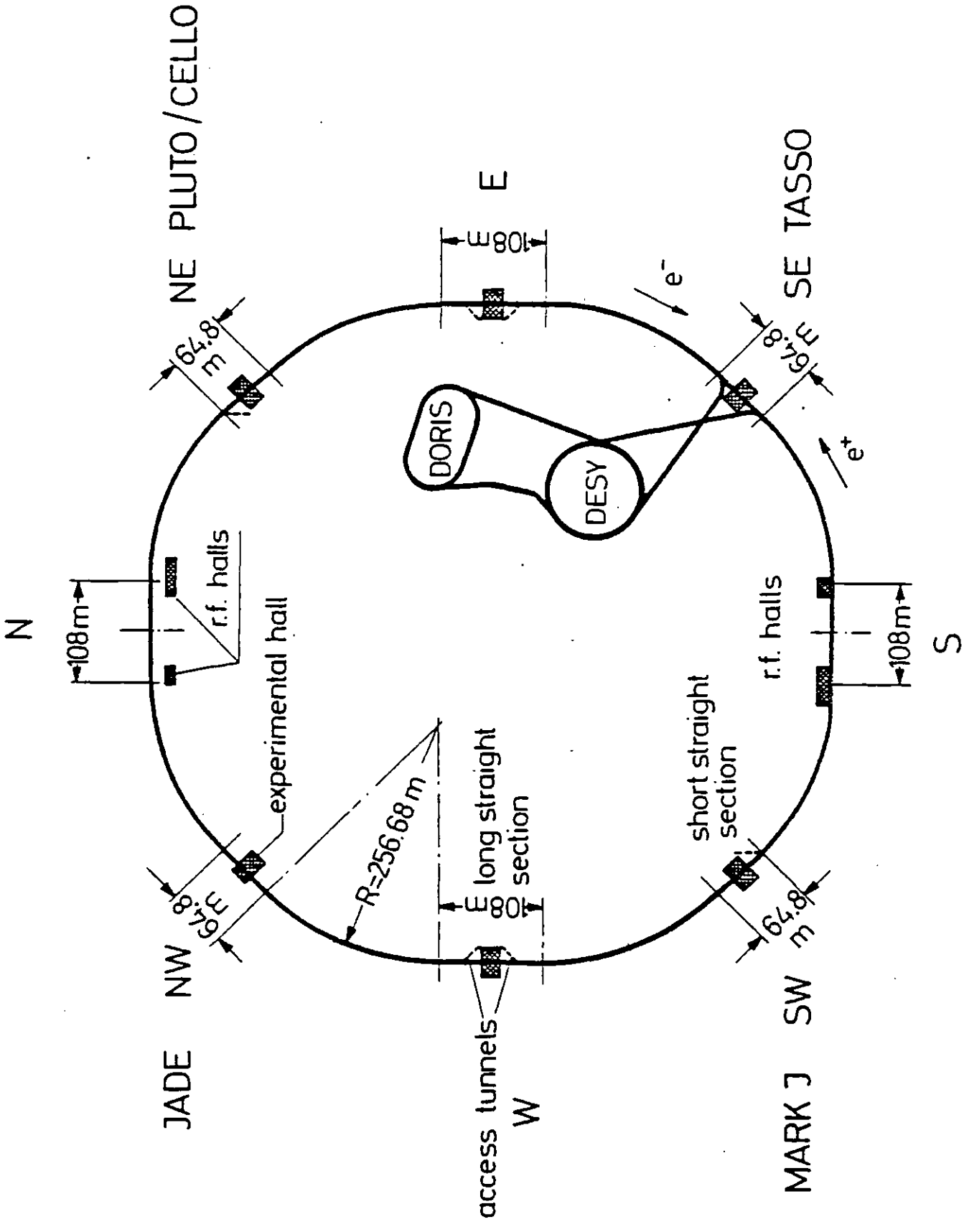


Fig 2·1 schematic diagram showing the layout of the PETRA storage ring

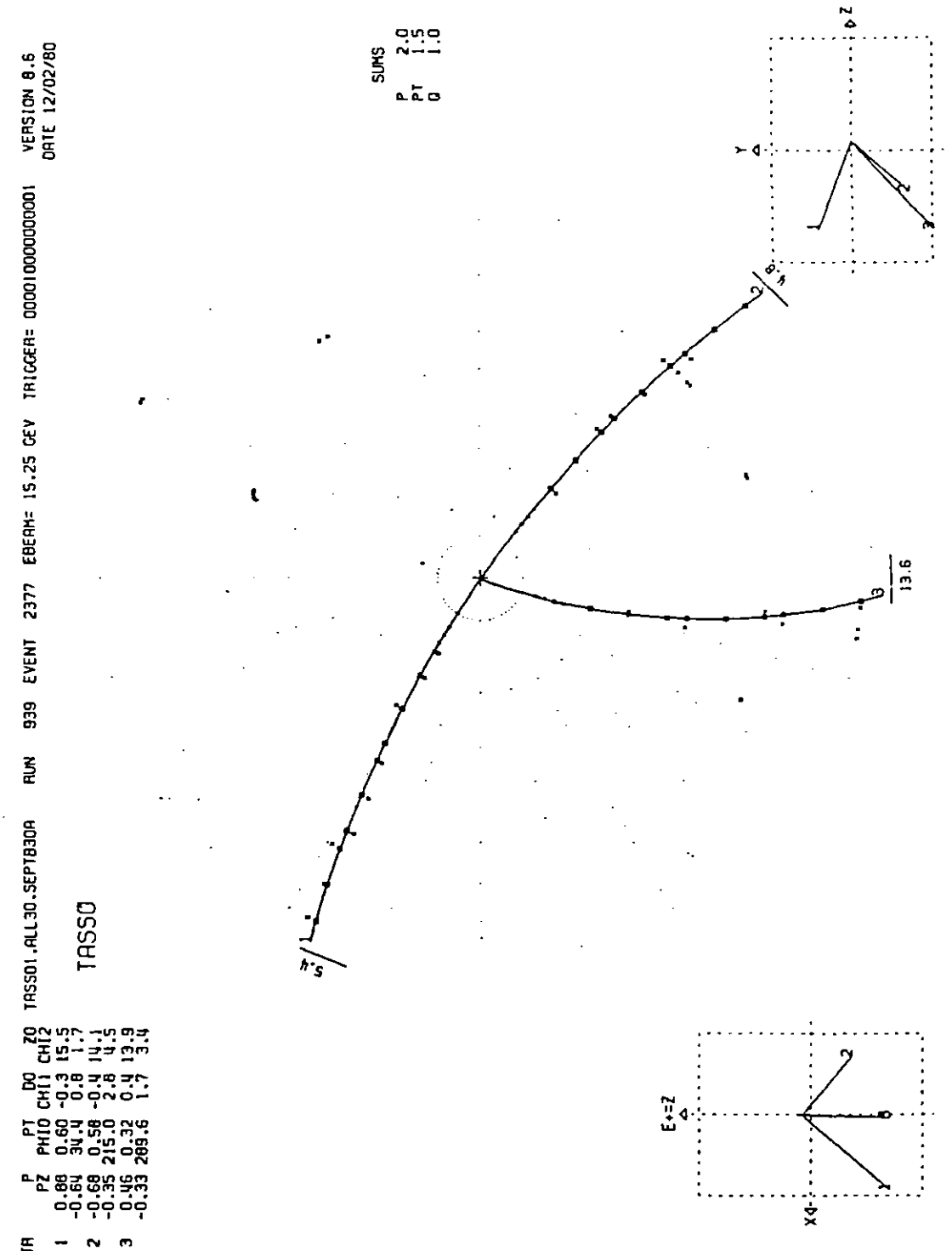


Fig 2·2 beam gas scattering event

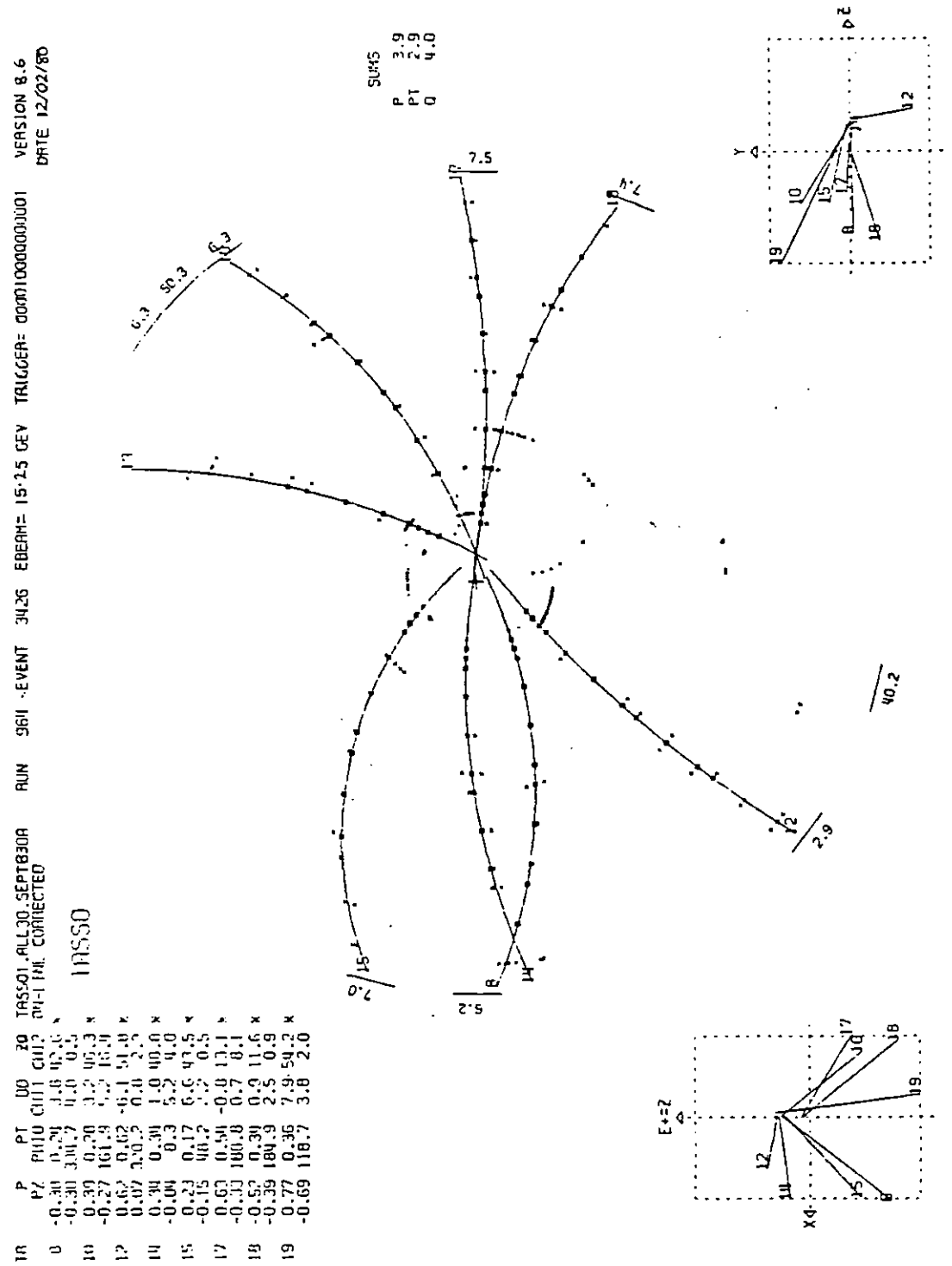


Fig 2·3 beam pipe interaction event

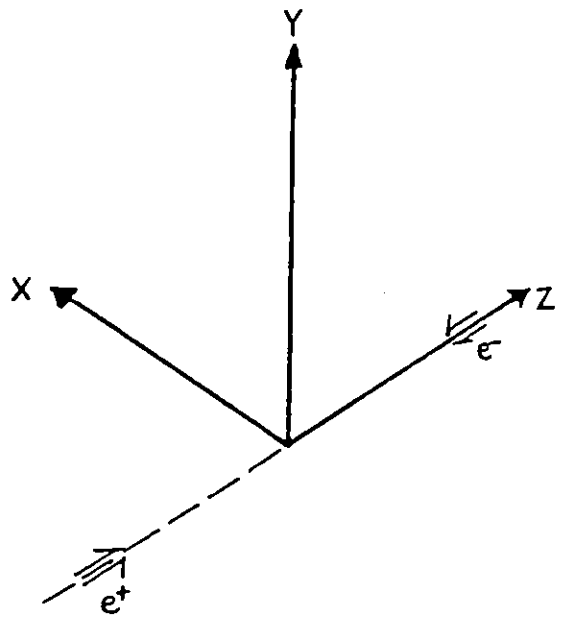
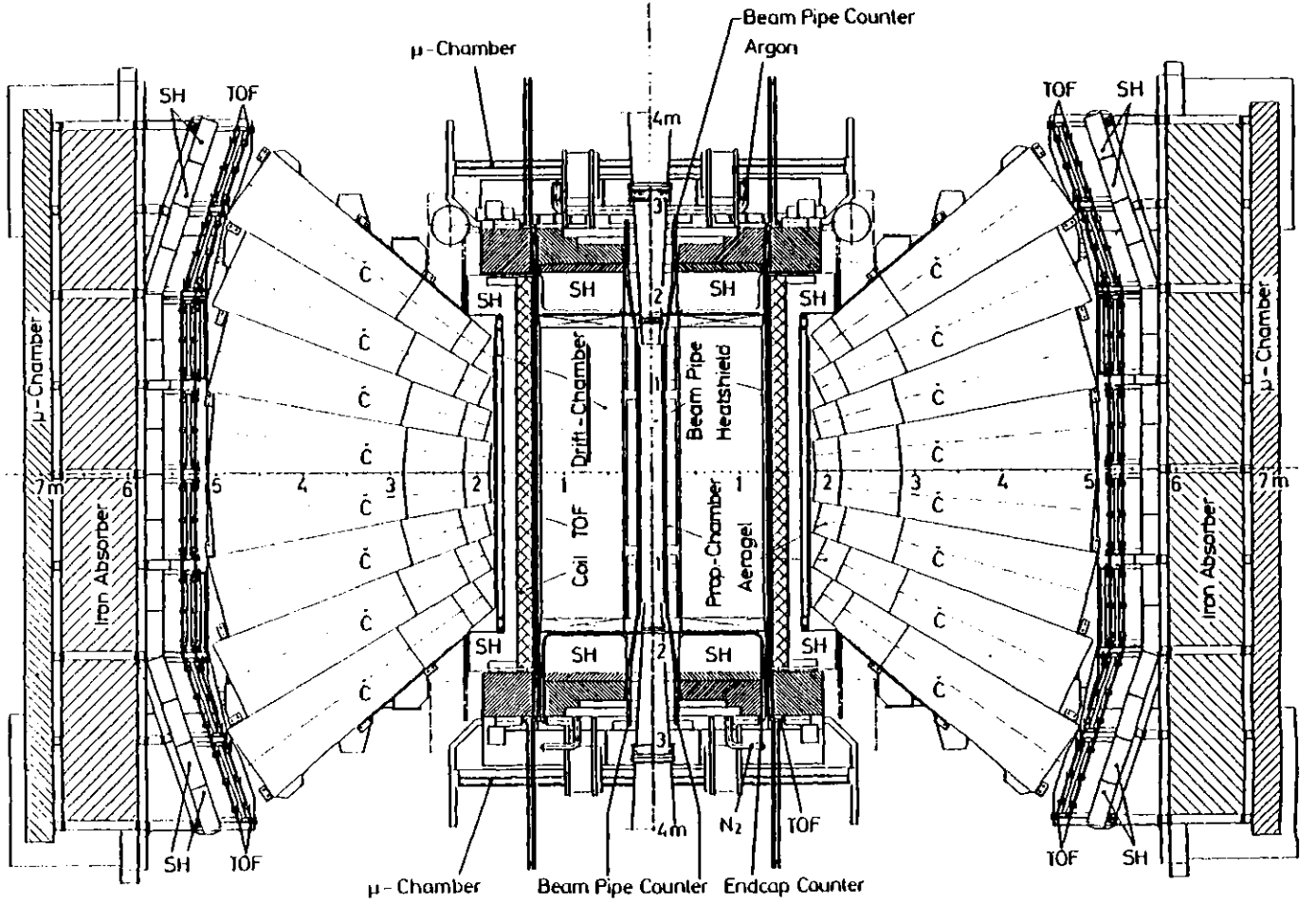


Fig 2·4 the TASSO coordinate system



TASSO

22.5.80

30151

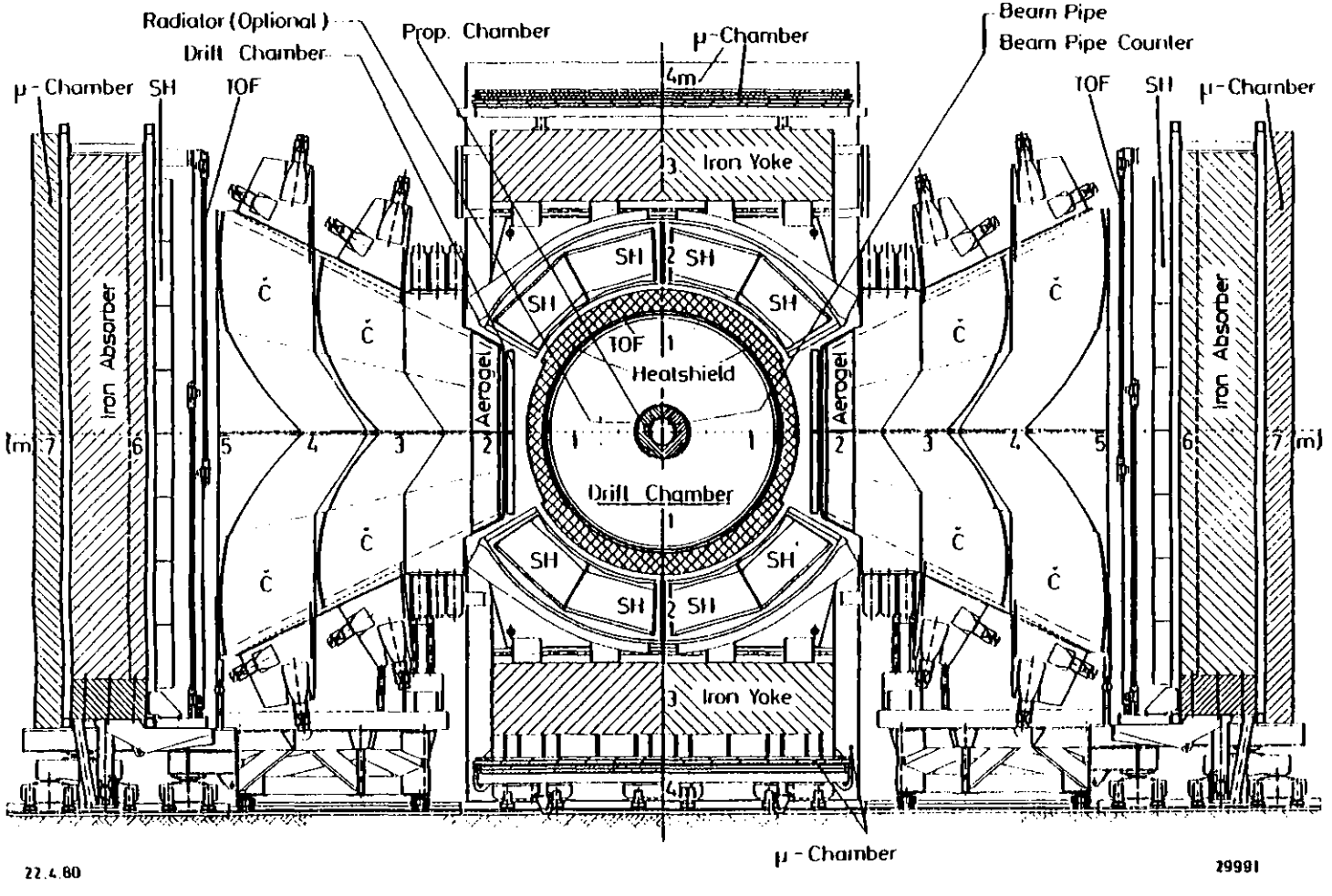


Fig 2.5 the TASSO detector

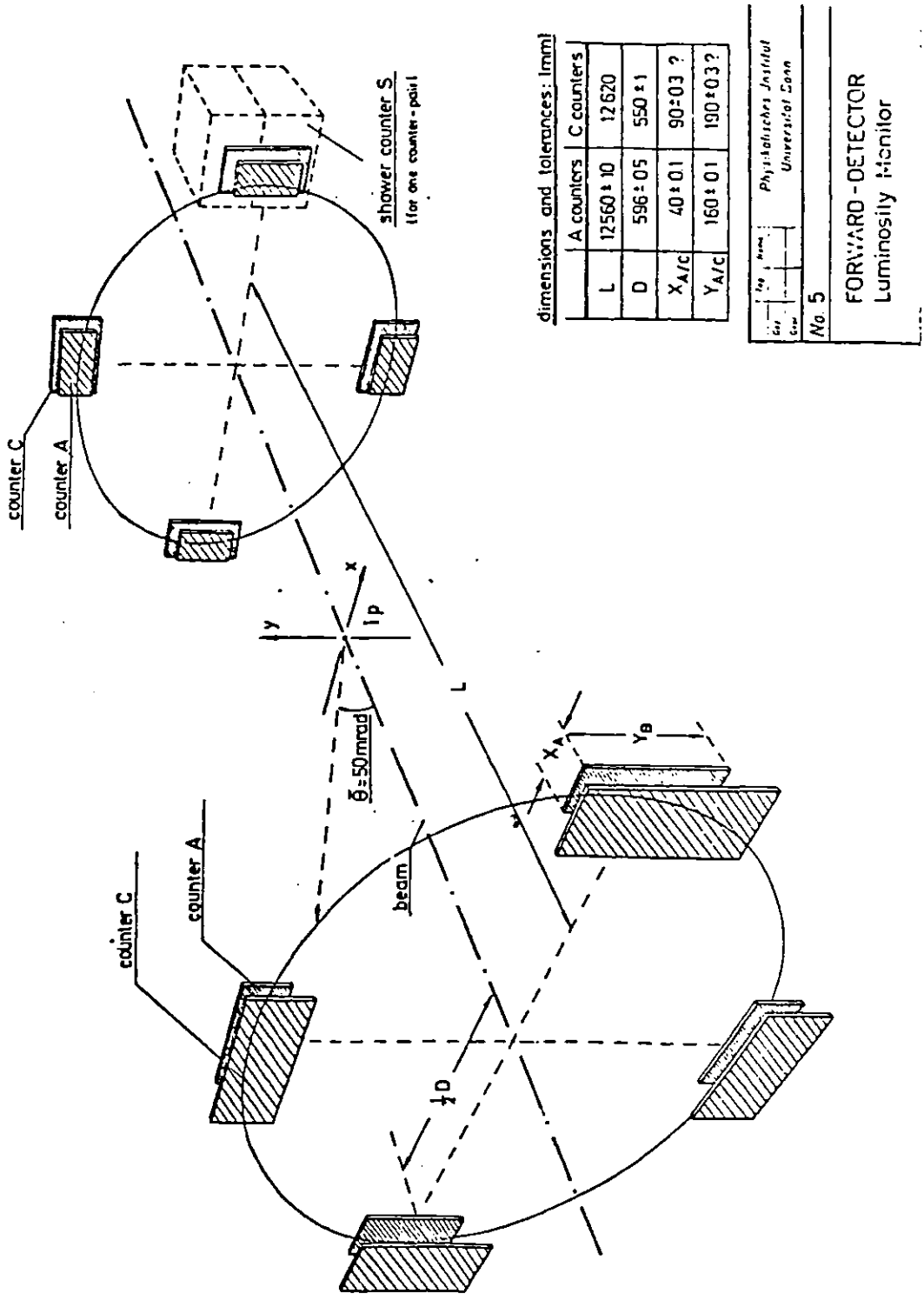


Fig 2·6 the TASSO luminosity monitor

CHAPTER 3

TRIGGER SYSTEM, DATA ACQUISITION AND OFFLINE DATA REDUCTION

3.1 Introduction

Bunches of particles intersect at each interaction point at a rate of ~ 250 KHz. A trigger system is therefore required which will select e^+e^- interactions but reject beam-background events while reducing the data taking rate to a manageable level. The Trigger system used to achieve this for the TASSO experiment is explained.

Following this, a description of the TASSO data acquisition program and on-line monitoring of the experiment is given.

The data taking rate is still high (~ few Hz) compared to the genuine data rate and is predominantly due to background processes. Most of these events are removed by the TASSO off-line data selection programs, which are described below. Data analysed in this thesis was selected from the datasets produced by these programs.

3.2 Trigger system

The trigger logic was arranged to be able to make a decision on whether a valid trigger had been received every time that bunches intersect. In 4-bunch mode there are 1.92 μsec available between successive intersections and in 2-bunch mode there are correspondingly 3.84 μsec. A reset time of 1 μsec was required to reset all components which left 900 nsec and 2.9 μsec to make a decision when running with 4 or 2 bunches respectively.

Initially the timing was set assuming data taking with 4 bunches in each beam. The DC prepro, which will be described later, was unable to make a decision within 900 nsecs, which led to a system of pre and post-triggers being adopted[†]. The pre-trigger decision was available within 900 nsecs. After receiving a pre-trigger an interval of ~ 5.5 μsecs

† At the end of 1980 the pre-trigger was no longer needed when it was decided that PETRA would not operate in a 4 bunch mode.

(2 beam crossings) was available for a post-trigger decision to be made. If no post-trigger had been received by this time a reset was issued.

The interface between the online computer, a NORD 10S, and the trigger electronics was called the SIGH box (Strobe Interupt Gate Handler). This controlled the strobes and resets issued to the read-out electronics and decided on whether a valid trigger was received. On receiving a valid trigger the SIGH box sent an interupt to the NORD which initiated readout of the detector. Strobes and resets were disabled until readout was completed when the NORD issued a reset to the electronics. A total of 16 different triggers were available which could be selected manually or by computer control. The registers of the SIGH box could be read by the computer so that the trigger bits set for an event were recorded as part of the information read out. This allowed an event selection based on a particular trigger to be made.

Stand alone triggers were also used along with pre and post-triggers. The particular triggers used are described below. A schematic diagram of the trigger logic is shown in Fig 3.1 and the trigger rates for a typical data-taking run are shown in Table 3.1.

3.2.1 Experimental Strobe

The experimental strobe was derived from a capacitive probe[57] at $z = -7.1$ m which sensed the bunches as they passed it. The induced signal from the passage of the positron bunch was attenuated and discriminated at a fixed threshold to provide the strobe.

Changes in the bunch currents affect the pulse height of the induced signal, which results in a time-slew of the strobe of the order 100-200 psec. This was sufficient to affect the TOF counter resolution. To correct off-line for this variation part of the induced signal was sent to a zero-crossing discriminator[58], which has far less time slew, and then to a TDC (Time to Digital Converter).

3.2.2 CPC processor

The CPC hardware processor (HWP)[59] looked for track segments using data from the 4 anode planes of the CPC. Coincidences of hits were searched for in 4 pairs of planes, planes 1 and 2, 2 and 3, 3 and 4 and 1 and 4, where the increasing radii of the planes is denoted by increasing plane numbers. The number of adjacent wires searched through in each plane was programable and corresponded to looking for track segments with different degrees of curvature; a minimum transverse momentum P_T of 100 MeV/c was used.

The chamber was divided azimuthally into 96 sectors with 5 anode wires in each plane. A 3-fold track segment was defined as a coincidence in 3 out of 4 of the pairs of planes in a sector while a 4-fold track segment was defined as a coincidence in all 4 pairs. The 96 sectors were paired to form 48 bits which were used by the DC preprocessor. A fast 'OR' of the 48 bits formed part of the pre-trigger.

3.2.3 DC preprocessor (DC prepro)

The DC prepro searched for tracks using field programmable logic arrays (FPLA), with one FPLA for each of the 72 cells of the innermost DC layer. Data from 6 of the DC 0^o planes was fed to each FPLA, (planes 1, 3, 5, 8, 11 and 13 were used where increasing number denoted increasing radius). 16 different track momentum masks were defined for each FPLA and a 5 out of 6 majority logic decision was made for each mask.

Additional data from the CPC HWP (48 bits) and the 48 ITOF mean timers was used. A track was defined as a valid mask which projected through a set ITOF mean timer (± 1 mean timer) and a set CPC HWP bit (± 1 bit). The multiplicity was determined by the number of ITOF mean timers ie. a valid mask projecting through 2 mean timers would count as 2 tracks. The DC prepro had an efficiency dependent on transverse momentum P_T with a constant efficiency ~ 97% above P_T ~ 500 MeV/c.

3.2.4 Pretrigger

The pretrigger did not initiate readout but temporarily disabled the strobe to wait for a decision from the DC prepro.

The pretrigger used is as follows:

$$\text{Pretrigger} = (\text{CPC} \geq 1).(\text{ITOF} \geq 1)$$

where CPC represents the fast 'OR' of the CPC HWP 48 bits and ITOF represents the multiplicity of the ITOF mean timers.

3.2.5 Stand alone triggers

Stand alone triggers received by the SIGHBOX disabled the strobe and initiated readout. The triggers used are as follows:

$$\text{STAND ALONE} = \text{SHI} + \text{FDI} + \text{LUMI}$$

LUMI represents the trigger produced by the luminosity monitor, as it had a high rate then only every tenth event was recorded. FDI represents the forward detector double tag trigger which required a hit in the scintillation counter hodoscope combined with a large pulse height in the lead glass array in both forward detector modules. The shower counter total energy trigger, SHI, will be described in chapter 4.

3.2.6 Post-triggers

Post-triggers could only disable the strobe and initiate readout if a pre-trigger had already been received. The triggers used are as follows:

$$\text{POST TRIGGER} = \text{DCIII} + \text{DCII} + \text{DCI} \cdot \text{SHII} + \text{DCI.FDII}$$ where

DCI, DCII and DCIII represent outputs from the DC prepro. DCI required that ≥ 1 track was found by the prepro, DCII (the topology trigger) demanded that the prepro found 2 tracks that were collinear to within 27° (± 3 ITOF counters) and DCIII (the multiplicity trigger) demanded ≥ 4 and ≥ 3 found tracks for Ebeam ≥ 17 GeV and < 17 GeV respectively. DCIII was the normal hadronic trigger and DCII was the normal Bhabha trigger.

DCI was combined with shower counter (SHII) and forward detector (FDII) triggers. FDII required a single tag in one forward detector module, SHII is described in chapter 4.

3.3 DATA Acquisition system

The data acquisition program[60] was activated after an interrupt was received from the SIGH box. It read in data from the detector via CAMAC. Not all components were necessarily read out; the subset of components to be read out was determined from the trigger information provided by the SIGH box, ie when a luminosity trigger was received only the corresponding data were read out.

The data were then reformatted and stored using the Bank Organisation System (BOS)[61] with additional information on the status of the experiment. A typical event length was 2500 words.

Finally the data were sent via a high speed link from the NORD computer to the DESY computer centre where it was temporarily stored on a 100 M byte disc. When this became full it was dumped onto 6250 BPI magnetic tapes.

A local disc buffering system utilising the NORD computer's 66 M byte discs could provide up to 4 hours of local data storage. This removed deadtime caused by breakdowns in the link or the off-line computer.

During a normal running period the data taking rate was ~ 1-2 Hz with a deadtime of ~ 4% per Hz.

3.3.1 On-line status of the experiment

During data taking the current status of the experiment was displayed on a TV screen. This information included the event rate, the rates of individual triggers and the measured luminosity which was shown graphically and as a rate.

Data from 10% of all events were recorded as histograms which could be displayed on a second TV screen, allowing simple quality checks to be made. For example the hit distribution histogram from each CPC plane shows up failures in the readout electronics. Up to 600 histograms were available.

The current event could also be displayed on a TV screen so that the

information from several components could be examined. A facility existed to display events with a particular combination of triggers which proved useful in checking trigger and detector electronics.

At the end of every run a selection of histograms from each component, with information on event rate, trigger statistics and luminosity was printed out to provide a permanent record.

3.4 Off-line data reduction

In the following sections the data reduction scheme is described. The order of the programs is shown schematically in Fig 3.2.

3.4.1 PASS 1

The initial stage of the data reduction chain was called PASS 1 and operated on raw data stored on dump tapes. Any reformatting or unpacking of compressed data was carried out and calibration corrections to data were made.

A fast track finding algorithm 'FOREST' was run using information from the DC 0° layers. This used a tree finding method[62] to link together hits in neighbouring layers to form tracks in the R-ϕ projection. If more than 1 R-ϕ track was found a second program 'ZREC' was run which assigned hits from the DC stereo layers to found tracks and determined their z-projection. FOREST was also run again with looser cuts if it had already found more than 1 track. A linear drift time relation was assumed when calculating the ϕ values of hits in the DC. New data banks were created from the output of these programs which contained track parameters and also listed the DC hits assigned to each track.

After PASS 1 all data were written onto 6250 BPI tapes with approximately 12,000 events on each tape. No data were rejected at this stage.

3.4.2 Track parameterisation

Each reconstructed track was defined by the 6 variables R, d_0, Z_0, ϕ_0,

tan λ and q. The variables z_0 and ϕ_0 were defined at d_0, the closest distance of approach to the origin of coordinates in the R-ϕ plane, z_0 being the z coordinate and ϕ_0 the azimuthal angle. R represents the radius of the track in the R-ϕ projection, λ is the dip angle and q is the charge of the track. The track parameterisation is shown in Fig 3.3.

3.4.3 PASS 2

The PASS 2 program was the first reduction step in the analysis chain where loose cuts were applied to data from PASS 1 tapes.

Event selection at this stage required either

1) $\geq$ 2 tracks reconstructed in R-ϕ with $|d_0| \leq 2.5$ cm, the d_0 cut selects tracks which are associated with the interaction point.

2) Any forward detector double tag event or any single tag event with $\geq$ 1 track reconstructed in R-ϕ and with $|d_0| \leq 2.5$ cm.

3) Any event with the SHI trigger bit set and > 3 GeV energy in opposite shower counter groups, or $\geq$ 1 GeV in one shower counter with $\geq$ 1 R-ϕ track, with $|d_0| < 2.5$ cm and the SHII.DCI trigger bit set.

All luminosity monitor events were accepted at this stage.

The data reduction at PASS 2 was typically 80%.

3.4.4 PASS 3

The PASS 3 program was intended as a hadronic event selection, other classes of events remained on the PASS 2 tapes.

Event selection required

1) $\geq$ 3 tracks reconstructed in R-ϕ with $|d_0| \leq 2.5$ cm and $\geq$ 2 tracks reconstructed in z with $|z_0| \leq 30$ cm.

2) Any forward detector tagged event.

This selection was called PASS 30, events satisfying condition 1) above were further subdivided into 2 classes. PASS 3 selected the events where $|z_0| \leq 10$ cm and included the hadronic events while PASS 3B selected the events where 10 cm $\leq |z_0| \leq 30$ cm. PASS 3B data was used to estimate the

background due to beam gas events in the PASS 3 sample.

3.4.5 BHASEL

This was the selection procedure for Bhabha events which operated on PASS 2 data.

Event selection required

1) The number of tracks 'N_T' with $|d_0| \leq 2.5$ cm and with transverse momentum $P_T > 0.1$ GeV/c should be $2 \leq N_T \leq 4$. Allowing more than 2 tracks included those Bhabha events where showering had occurred in the material preceding the DC.

2) For events with $N_T > 2$ then at least 2 tracks had to satisfy the condition $\Delta\phi_0 < 5°$. If tracks were due to showering in the detector then they should be clustered together with similar ϕ_0 values.

3) At least 2 tracks were coplanar to within 15° in the R-ϕ plane. For Bhabha events produced in the centre of mass frame the produced electron and positron should be back to back.

4) The number of tracks 'N_z' with 3-dimensional track reconstruction and with $|z_0| < 15$ cm should be $N_z \geq 1$. This is a loose fiducial volume cut to select events coming from the region of the interaction point.

5) The 2 coplanar tracks should intersect the ITOF counters with a measured time 't' in the range -3nsec < t < 25nsec and their time difference should satisfy the condition $\Delta t < 5$ nsec. This cut is designed to eliminate background from cosmic ray events passing the previous 4 cuts, cosmic ray tracks have a larger time difference as they pass through the whole DC with twice the average path length of Bhabha tracks.

Events passing these cuts were written onto 6250 BPI tapes.

3.4.6 Mill

Mill is a track finding algorithm using the same tree finding method

used by FOREST but with more relaxed cuts and more passes through the data. It also used a non-linear drift time relation which was determined from cosmic ray events and used the CPC anode hits in the R-ϕ fit by extrapolation of DC tracks.

The Mill procedure found more tracks than FOREST with a better resolution but it was too slow to be run as the primary track finding algorithm and was only run on the final data samples produced by the PASS 3 and BHASEL programs. Event reconstruction times for several classes of events using Mill are given in Table 3.2.

A resolution in the position of DC hits of ~ 200 μ was achieved for tracks normally incident on a drift cell giving a momentum resolution $\sigma_p/p = 0.02p$ (pin GeV/c). The efficiency for single tracks was > 98% for $P_T \geq 100$ MeV/c and fell rapidly below this.

SUMMARY OF RUN 16911 .....

EVENT STATISTICS

NO. OF EVENT TRIGGERS	2046	(	0.66HZ)
NO. OF EVENTS INPUT OK	2046	(	0.66HZ)
NO. OF EVENTS FORMATTED	2046	(	0.66HZ)
NO. OF EVENTS TRACKED	0	(	0.00HZ)
NO. OF EVENTS OUTPUT	2046	(	0.66HZ)
NO. OF EVENTS REJECTED	0	(	0.00HZ)
NO. OF EVENTS FULL-TRACK	0	(	0.00HZ)
NO. OF EVENTS ANALYSED	205	(	0.07HZ)
NO. OF EVENTS ????	0	(	0.00HZ)
NO. OF EVENTS ????	0	(	0.00HZ)

TRIGGER STATISTICS

NO. OF TOF PRE-TRIGGERS	1486	(0.48HZ)	72.63%
NO. OF UNALLOCATED TRIGGERS	0	(0.00HZ)	0.00%
NO. OF RANDOM BEAM-CROSSING TRIGGERS	0	(0.00HZ)	0.00%
NO. OF RANDOM TOF PRE-TRIGGERS	0	(0.00HZ)	0.00%
NO. OF UNALLOCATED TRIGGERS	0	(0.00HZ)	0.00%
NO. OF LUMINOSITY TRIGGERS	54	(0.02HZ)	2.64%
NO. OF TOF COSMIC TRIGGERS	0	(0.00HZ)	0.00%
NO. OF SHOWER NEUTRAL TRIGGERS	430	(0.14HZ)	21.02%
NO. OF GAMMA-GAMMA TRIGGERS	98	(0.03HZ)	4.79%
NO. OF TEST TRIGGERS	0	(0.00HZ)	0.00%
NO. OF DC PREPRO TRIGGERS	1324	(0.43HZ)	64.71%
NO. OF CPC+HUP TRIGGERS	0	(0.00HZ)	0.00%
NO. OF HUP*IDCP TRIGGERS	0	(0.00HZ)	0.00%
NO. OF SHOWER(ONE TRACK) TRIGGERS	144	(0.05.IZ)	7.04%
NO. OF GAMMA-GAMMA(ONE TRACK) TRIGGERS	33	(0.01IZ)	1.61%
NO. OF UNALLOCATED TRIGGERS	0	(0.00HZ)	0.00%

Table 3·1 typical event and trigger statistics from the run summary

Event Type	Time
Hadronic	~10 sec.
Bhabha	~3.5 sec.

Table 3·2 typical event reconstruction times for MILL

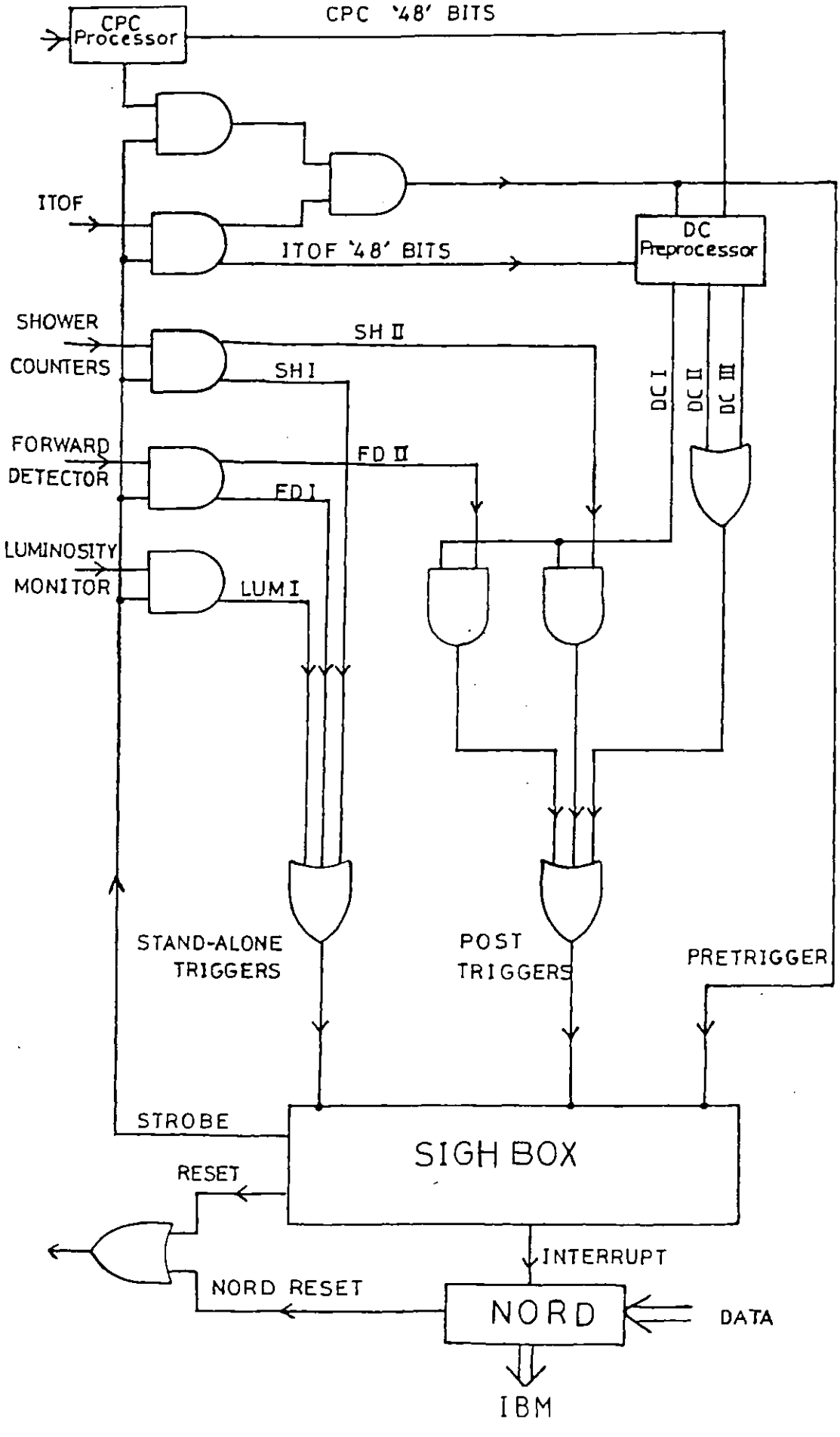


Fig 3·1 schematic diagram of the TASSO trigger logic

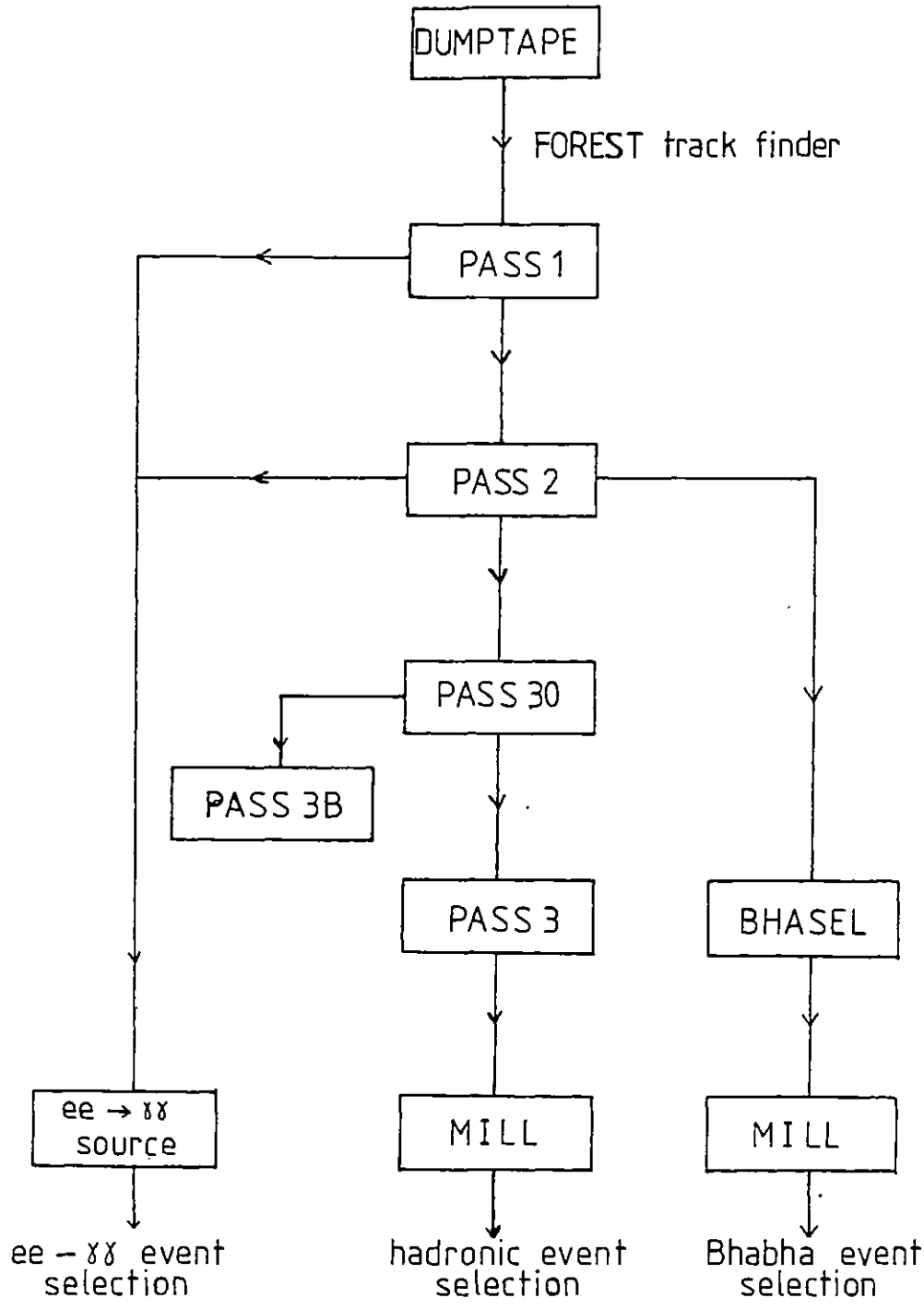


Fig 3·2 schematic diagram of the data reduction chain

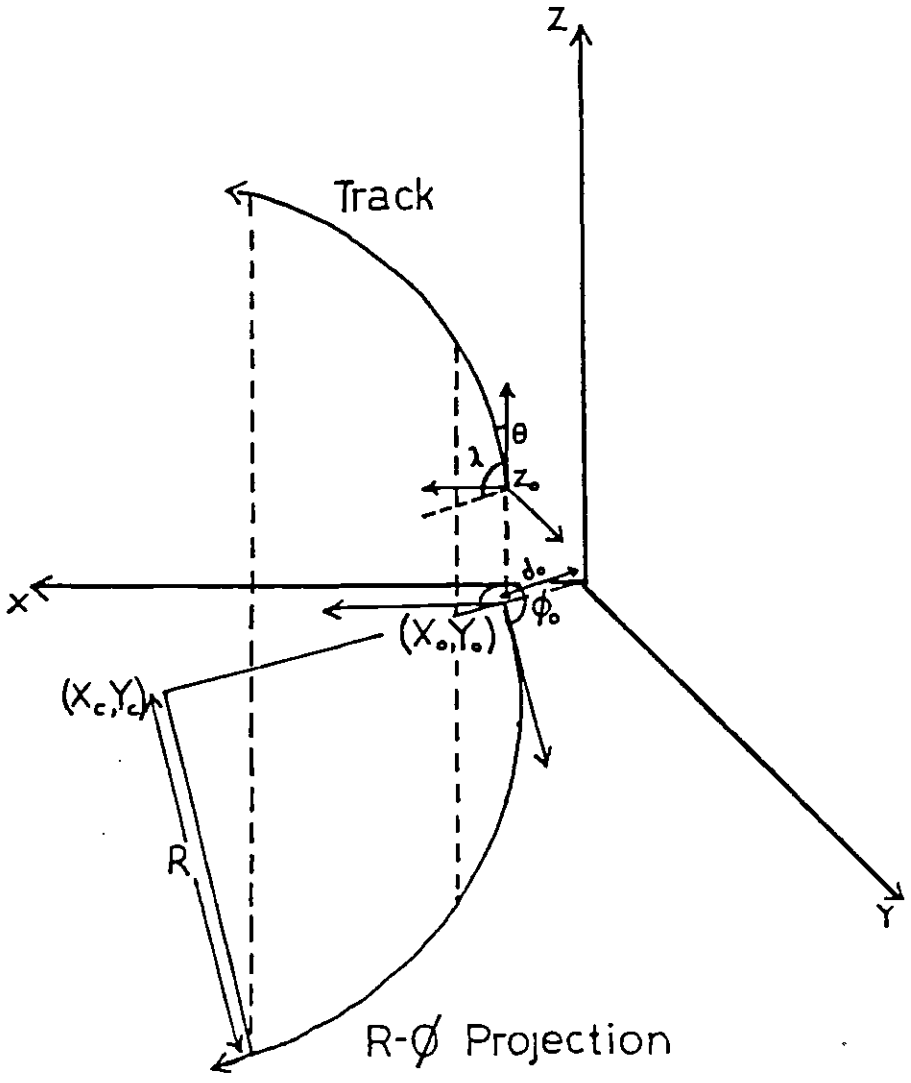


Fig 3·3 track parameterization

CHAPTER 4

SHOWER COUNTERS

4.1 Introduction

A large area (~ $92m^2$) shower counter array for the hadron arms of the TASSO detector has been built by DESY, IMPERIAL COLLEGE and OXFORD and installed in the detector. The shower counters were designed to give a reasonable energy resolution (σ_E/E ~ 19%/$\sqrt{E}$ for E < 3 GeV) and position resolution (0.019 steradians per module) at a low cost.

In this chapter the shower counter will be described in detail.

4.2 Physics motivation

The shower counters provide information on the energy of electrons and photons emitted into the solid angle of the hadron arms (20% of 4π) complementing the information provided by the Cerenkov, muon and time of flight counters. The shower counters serve four essential purposes:

1) They provide a measurement of the neutral energy emitted into the hadron arms which is important for the separation of events from the 1γ and 2γ reactions.

2) They provide information on the amount of neutral energy produced in the jets of particles from the 1γ and 2γ reactions.

3) They increase the overall probability of reconstructing π^0's.

4) They identify electrons up to the highest available momentum. The 3rd hadron arm Cerenkov counter starts to detect pions in addition to electrons at momenta above 5 GeV/c.

4.3 Design requirements

The shower counter detector for the hadron arms was designed[63] to satisfy the following requirements:

1) It should provide good electron-hadron separation.

2) The energy resolution for an electromagnetic shower should be reasonable ($\sigma_E/E \lesssim 20\%/\sqrt{E}$ for E < 4 GeV).

3) The response of the shower counter should be as uniform as possible over its surface.

4) The granularity of each module should be similar or smaller than the granularity of the Cerenkov counters in front of the shower counter array.

The space available in the hadron arms for the shower counters and the requirement that they should hang from the iron muon filter of the hadron arm gives two additional constraints:

5) The total depth of a module should not exceed 35 cms.

6) The photomultipliers should be mounted on the front surface of the shower counters, otherwise they would be inaccessible.

The availability of low cost acrylic scintillator made the choice of a lead scintillator sandwich counter the most attractive one. The limited space available constrained the thickness to ~ 8 radiation lengths. The major problems involved with acrylic scintillator are the low light output and the small attenuation length $\lesssim$ 1.4 m[64]. Good light collection in a large area combined with reasonable uniformity can be obtained by using a wavelength-shifter bar in loose optical contact with the acrylic scintillator.

An additional advantage of using a wavelength-shifter bar is that a very compact light collection system can be designed, which also permits the use of small 2" photomultiplier tubes. For these reasons a wavelength shifter readout system was chosen.

4.4 The "Wavelength shifting" technique

The idea of using fluorescence radiation conversion to the detection of scintillation was first proposed by Shurcliff[65] and Garwin[66], and has been extensively studied by Keil[67].

In scintillator material the energy deposited by the passage of an ionising particle is converted into visible light. The ionisation first

excites a primary fluor which emits ultra-violet (U.V.) light. As the attenuation length of U.V. light is small (~ few mm's) in most materials the scintillator is doped with a second fluor which absorbs U.V. light and re-emits light at a wavelength where the attenuation length is much larger (~ few m's). A typical wavelength of the emitted light is in the blue region of the spectrum.

Part of the fluorescent light produced inside the scintillator is emitted at angles greater than the critical angle and is trapped inside the scintillator. The high geometrical symmetry of the rectangular pieces of scintillator means that they act as a light guide for this part of the light which is then transported to the edge by total internal reflection.

At the edge of the scintillator lies a wavelength-shifter bar. This is an acrylic bar doped with a third fluor which absorbs blue light and re-emits green light isotropically. The blue light that reaches the edge of the scintillator passes into the bar is absorbed and re-emitted as isotropic green light. Part of this light is trapped inside the bar and is transported to the ends by total internal reflection. The coupling between the scintillator and the wavelength-shifter bar is over an air gap otherwise the light produced in the bar would not be trapped by total internal reflection, but would pass back into the scintillator and be lost. The end of the bar is then viewed by a single photomultiplier tube. A sketch of this process is shown in Fig 4.1.

To design an efficient wavelength shifter bar system:

1) The absorption spectrum of the wavelength-shifter bar must match the emission spectrum of the scintillator and to absorb as much of the scintillator light as possible the concentration of wavelength-shifter must be sufficiently large or the bar sufficiently thick.

2) To maximise the light output from the wavelength-shifter bar the attenuation length in it must be as large as possible. To achieve this

the amount of re-absorbtion of the shifted light by the wavelength shifting molecule must be minimised, by choosing molecules with well separated absorbtion and emission spectra, or by increasing the wavelength-shifter bar thickness while decreasing the concentration of the wavelength-shifting molecule.

3) To match the response of the photomultiplier the wavelength of the emitted light should be in a region where the photocathode has good quantum efficiency.

The choice of scintillator and wavelength shifter bar dopings used were based on studies previously reported in the literature[68]. The acrylic scintillator used is plexiglass doped with 3% napthalene, 1% butyl PBD and 0.01% POPOP by weight provided by POLIVAR[69]. The wavelength-shifter bar used is plexiglass doped with 120 mg/liter BBQ provided by ROHM[70]. The function of those molecules are shown in Table 4.1. The scintillator provides light at ~ 420 nm which is absorbed by the BBQ and shifted to wavelengths ~ 495 nm. With the concentrations given above the attenuation of light in the scintillator is $\lesssim$ 1.4m, the wavelength-shifter bar has an absorbtion length ~ 1 cm and an attentuation length ~ 2 m. The emission spectrum of POPOP and the absorbtion and emission spectra of BBQ are shown in Fig 4.2. A measurement of the absorbtion length of scintillator light in BBQ[71] is shown in Fig 4.3.

4.5 Description of the shower counter

The shower counter array in each hadron arm consists of 32 identical modules, each of dimension 142 x 100 x 20 cm^3. The central part of the array is parallel to the beam axis while the wings of the array are bent inwards by 19° to slightly increase the solid angle acceptance, the array is shown in Fig 4.4. Each module matches the granularity of the Cerenkov counters.

A module is made from steel plates welded together to form an open box. A large steel plate is folded to form the back and sides, two plates are welded to this to form the top and bottom sides and a plate is welded across the middle dividing the box into two equally sized compartments. The box is designed to be vertically mounted on an iron frame which is fastened to the iron muon filter in each hadron arm. For this two metal hooks are welded to the top of the backplate which hang on metal pads welded to the iron frame. A steel bolt passes through each hook to rest on the pad and by unscrewing these the module can be lowered into position. A module is shown suspended from the frame in Fig 4.5. The bottom and middle shelf are thicker than the other steel plates to support the weight of the lead scintillator stacks. The box is completed by two thin steel plates, secured to the top with self tapping screws.

Each compartment holds two stacks of lead scintillator. A module is laid on its back to be filled. Two rubber mats are placed in each compartment to provide protection for the bottom piece of scintillator in each stack and also to prevent the stack sliding into the middle of the box. Movement of the lower piece of scintillator into the middle of the box is due to the side of the box being curved at its base. The rubber mats and all side walls are covered by a layer of aluminium foil.

Each stack of lateral dimension 68 x 48 cm^2 is laid in the box with each component placed against the bottom and side walls. A stack consists of 9 pieces of acrylic scintillator each 1 cm thick and 8 pieces of lead each 5 mm thick interleaved with the scintillator. Each piece of scintillator is separated from the neighbouring piece of lead by a layer of polythene film and a layer of aluminium foil with the shiny surface facing the scintillator. Before installation each piece of scintillator was thoroughly cleaned using alcohol to provide the best possible surface finish. The scintillator is only polished on three edges, the fourth

unpolished edge is covered with a layer of white tape which is then placed against the side of the box. This improves the overall light output and provides some compensation for the decrease in light collection yield at greater distances from the output edge of the scintillator, due to light absorbtion[67]. A thick aluminium cover plate of lateral dimension 68 x 48 cm^2 completes the stack. It is held in place by four aluminium brackets which are screwed into the top and bottom steel plates of the compartment. Together the cover plate and brackets hold the stack in place when the box is hung in the vertical direction. Fig 4.6 shows a cross-section of a stack. The box is moved into the vertical direction after the four stacks have been installed.

The wavelength-shifter bar of dimension 68 x 14.8 x 1 cm^3 is placed in the gap between a pair of stacks and views their light output. The bar has a mirror of aluminised mylar not in direct optical contact at its lower end, this improves its efficiency by increasing the amount of light reaching its upper end. The attenuation length of light in the bar is ~ 2 m, which results in a large non uniformity of response to scintillator light absorbed along its length. This is compensated for by partially obscuring the edge of each stack. Copper strips are taped to the cover plate of each stack and hang down the side of the stack facing the wave-length-shifter bar. The copper strips are closely spaced at the upper end of the stack and are spaced at larger intervals further down the stack. The positions and width of these strips are given in Table 4.2. At its upper end the wavelength-shifter bar is cemented to a plexiglass light-guide. Light entering the light guide is first reflected by a prism through 90° to one side, a second prism then reflects the light by 90° through the front surface of the shower counter module and it is then guided adiabatically to the photomultiplier tube. The reflecting surface of each prism is backed by a mirror of aluminised mylar coupled to it by an air

gap to increase the efficiency of each reflection. The light guide is completely covered with aluminium foil with the shiny surface facing inwards. The part of the light guide outside the shower counter box is also covered by a layer of black polythene and is then wrapped in black tape to make it light tight. Before installation into the shower counter the wavelength-shifter bar and light guide were thoroughly cleaned with alcohol to provide the best possible surface finish. The wavelength-shifter bar is held in position between the two stacks by rubber spacers at each end. The light collection system is shown in Fig 4.7.

A plexiglass connector to hold an optical fibre is glued to the mid-point of the upper surface of the wavelength-shifter bar and is used for calibration. In a second plexiglass connector glued to the adiabatic light guide is a green LED which can also be used for calibration. The use of these for calibration will be described later.

The photomultiplier and base units are mounted on the front face of the shower counter module. A length of angle iron is screwed to the bottom and middle plates of the box. From this are fastened two pieces of studding connected to clamps at one end and the metal can of the photomultiplier and base unit is held by these clamps. This arrangement is shown in Fig 4.5. The photomultiplier (P.M.) tubes used are 56 AVP 2" tubes for half of the modules, which were available from a previous experiment and EMI 9807B 2" tubes for the remainder of the modules. Each P.M. tube is coupled to its light guide with optical grease. The P.M. tube is spring loaded at its base, this and proper alignment of the clamps holding the can ensure a good contact with the light guide. Each P.M. tube is shielded from stray magnetic fields by being enclosed in a mu-metal can. The gap between the metal can and the light guide is sealed against light leaks by black foam rubber rings and a layer of black tape.

The whole box is sealed against light leaks with black tape.

4.6 Position of the counters in TASSO

During the early period of data taking with the TASSO detector the barrel liquid argon modules, designed to measure energy in the angular region around the solenoid, were not ready to be installed. As the angular region covered by the barrel liquid argon modules is much larger than the angular region covered by the hadron arm shower counters it was decided to install some of the shower counter modules around the solenoid, increasing the angular region in which energy measurement was made.

Two rows of four shower counter modules were installed above the solenoid and three rows of four shower counter modules were installed under the solenoid. The counters above the solenoid were supported by a frame constructed from aluminium girders which was hung from the magnet flux return yoke. The central row of counters under the solenoid rested on the magnet flux return yoke, the rows on each side of it were hung from iron girders which were fastened to the endplates of the magnet flux return yoke with their base resting on the magnet flux return yoke. Fig 4.8 shows the positions of the shower counters around the solenoid.

At the beginning of 1980 the upper half of the barrel liquid argon calorimeter was installed replacing the two rows of shower counters above the solenoid. Fig 4.9 shows the positions of the shower counters around the solenoid for this period. At the end of 1980 the lower half of the barrel liquid argon calorimeter was installed and all the shower counters were returned to the hadron arms.

4.7 Granularity of the shower counters

The space between each pair of lead-scintillator stacks is wide enough to accommodate two wavelength-shifter bars allowing the light from each stack to be separately read out. The three rows of shower counters under the solenoid had these additional wavelength-shifter bars installed, a doubling of their granularity.

The pair of wavelength-shifter bars are optically separated by a piece of aluminium foil which ensures that the light from each stack is only able to enter one of them.

When the shower counters were returned to the hadron arms the two outermost columns in each arm had their granularity doubled.

4.8 Electronics

The readout system for the shower counters will be described in this section. All the electronics for each component in a hadron arm were situated on a platform fastened to the back of the muon filter.

4.8.1 High Voltage system

High voltage (H.V.) for the P.M. tubes was supplied by Oltronix units each of which fed a distribution box with 11 outputs or by LRS 4032 32 channel H.V. units. Oltronix units supplied the north arm counters while the south arm counters were supplied by 2 LRS 4032 units and by Oltronix units for the additional P.M. tubes after doubling the granularity of some counters. A typical operating voltage for a P.M. tube was 2.2 kV.

During data taking the H.V. units were permanently switched on.

4.8.2 Readout system

Signals from the P.M. tubes travel along 28 m of coaxial cable to the readout electronics. Each cable entered a splitter panel where the signal was divided into two equal parts. One part was sent to the trigger electronics which will be described later, while the second part was sent to the (ADC) Analogue to Digital Converter patch panel. The ADC's used were LRS 2282 modules, each ADC module consisting of 48 12 bit charge sensing channels giving a dynamic range of 4095 counts with a slope of 0.25 picocoulombs/least count. The ADC's were controlled by a microprocessor (LRS 2280) and were read out by the one-line computer via CAMAC. The gate for the ADC's was provided by the experimental strobe. As the ADC system in each hadron arm was also used by the Cerenkov counters and hadron arm

TOF counters the gate that was applied to the ADC modules had to be compatible with the signals from all of the components using it. The signals from the Aerogel Cerenkov counter had a large time spread as the light from it was collected by diffusive reflections from its walls and a long gate length of 220 ns was then required.

If the TASSO trigger logic did not produce a valid trigger then a "fast clear" was issued to the 2280 module a constant 1 μs before the next data cycle.

The microprocessor has the ability to subtract previously stored pedestal values from the stored data values. For the data analysed in this thesis this facility was not used and the data values were read out uncorrected.

Pedestal values were calculated, before each data taking run, using data taking cycles with the strobe provided by a pulse generator.† The pedestal value is the ADC value of a channel when there is no signal from the PM tube, and a typical value of ~ 300 counts was seen.

A schematic diagram of the readout system is shown in Fig 4.10.

4.8.3 Trigger system

The part of the signals not going to the ADC's were sent to linear fan in units where a sum of all the signals was formed. Each module contains 2 groups of 8 inputs so that it was possible to obtain the sum of the signals from groups of 8 counters, as well as the total sum of all counters read out in an arm.

Two triggers were formed from this sum. The sum of all signals was fanned out into two outputs. Output one was passed through a discriminator at a high threshold and was then put into coincidence with a gate derived from the experimental strobe. A logical AND of this signal from the North and South arm shower counters formed the 'stand alone' energy trigger. Output two was passed through a discriminator at a low threshold

† the pulse generator operated provided strobes at the frequency of beam intersections, as the pedestal value obtained was frequency dependant.

and was then put into coincidence with a gate derived from the experimental strobe. The output triggered a gate generator producing a gate of 4 μs. A logical OR of this signal from the North and South arm shower counters was made and the output formed a logical AND with the output of the DC prepro to form the energy + > 1 charged track trigger.
A schematic diagram of the trigger system is shown in Fig 4.11.

The 'stand alone' energy trigger described above was for the case where shower counters were only installed in the hadron arms. For the running periods where some shower counters were installed above and below the solenoid a more complicated 'stand alone' trigger involving the sum of the signals from subgroups of counters was employed. The schematic representation of the trigger system for these shower counter positions are shown in Fig 4.12 and Fig 4.13.

Typically the 'stand alone' trigger is present in ~ 20% and the energy + > 1 charged track trigger is present in ~ 7% of all accepted events. The energies corresponding to the discriminator thresholds are shown in Fig 4.12 and Fig 4.13, showing the trigger systems used for each shower counter geometry. The 'stand alone' trigger threshold was also lowered for low energy running periods where a high threshold would cause some data to be lost.

4.9 Online calibration of the shower counters

The shower counter system was calibrated by a system of fibre optics which were uniformly illuminated by a Xenon flash lamp. Each group of 70 fibres were bundled together at one end and were held at a distance of 20 cm from the lamp. A connector at the end of each fibre plugged into the fibre optic connector mounted on the top surface of a wavelength-shifter bar midway along its length. The manufacturer has measured the light transmission of individual fibres, the variation between fibre's was less than 1%. Each fibre was 12 m long.

Light entering a wavelength-shifter bar from the attached fibre was shifted and transported to the PM tube in the same way as light entering from the neighbouring lead scintillator stacks.

In practice three lamps and fibre optic bundles were used as the fibres were not long enough to reach all of the counters. The output of one lamp was used as a reference for the other two lamps. The calibration of the additional lamps relative to the reference lamp was made by interchanging fibres illuminated by these lamps with fibres illuminated by the reference lamp, using the difference in the ADC values measured from each lamp. The reference lamp was calibrated using the light produced by a mono-energetic electron beam normally incident on the centre of a lead scintillator stack and corresponded to an energy deposit of ~ 10 GeV.

In laying the fibres from a lamp to the shower counters it was necessary to coil up part of the length of the fibres. Great care was taken to make sure that the fibres were not damaged or coiled too tightly as this would reduce the efficiency of light transport down the fibre which depends on total internal reflection from the fibre walls.

Each Xenon lamp was run as a free oscillator at a voltage of 2.7 kV. A signal from the base of the lamp travelled to the readout electronic along 28 m of coaxial cable, it was attenuated and discriminated before being used to provide a gate for the ADC modules. The start time of the gate was adjusted so that the signals from the PM tubes arrive at the ADC modules 50 ns after the start of the gate. The gate was passed to the ADC modules of the opposite arm so that the pedestal values of these modules could be calculated at the same time and was also passed to the TASSO trigger electronics as a special trigger which enabled the on-line computer to readout the ADC modules. Multiple signals were not recorded as the frequency of oscillation of the lamp was smaller than the cycle time of the ADC system.

Calibration runs using the Xenon lamps were taken every 4 days. Each lamp was run separately and the corrected ADC values of all three lamps were combined on the online computer to form the 'SHCL' bank. To check the quality of the calibration histograms of the ADC values of each channel recorded during the calibration run could be displayed at the on-line computer. Fig 4.14 shows the histogram of ADC values for a channel recorded in a calibration run. The drift of the lamps and the effects of slowly drifting HV supplies were corrected in the on-line calibration. The calibration was observed to vary typically by less than 5% over a period of two weeks.

A schematic diagram of the calibration system is shown in Fig 4.15.

4.10 Offline calibration of the shower counters

Bhabha scattering events seen in the TASSO detector were used to perform an offline calibration of the shower counters, by adjusting the energy spectrum of events measured by the shower counters so that the mean value was the same as the beam energy. Separate shifts were calculated for each group of counters illuminated by a Xenon lamp. It was not possible to calculate an individual shift for each counter as the number of events recorded in a counter was typically less than six for a data taking period of one month. Shifts were calculated every month and were applied to the energy deposits observed in the shower counters for all events. Table 4.3 shows the average shifts calculated from Bhabha events for different run periods. Fig 4.16 shows a scatter plot of the Bhabha energy deposited in the shower counters below the solenoid normalised to the beam energy for each counter. There are no large variations from counter to counter observable.

4.11 Tests and performance

Five counters have been tested in an electron beam and in a pion beam at energies up to 4 GeV[64]. In these tests the effect of the material

of the TASSO detector before the shower counters have been simulated by 1.5 radiation lengths of iron placed in front of the counter. Table 4.4 shows the results of measurements in the electron beam where the beam is normally incident at the centre of a lead scintillator stack. These results show that for energies less than 3 GeV the resolution of the shower counter is $\sigma/E \sim 19\%/\sqrt{E}$. The separation of electrons from pions has been examined by comparing the signal distribution obtained from the electron beam tests with the signal distribution obtained from the pion beam tests. A pion was considered to have been misidentified as an electron if its measured signal $S_{pion}(E)$ satisfied the conditions:

$$S_{pion}(E) > S(E) - 2.5\ \sigma(E)$$

where $S(E)$ and $\sigma(E)$ are the mean and standard deviation respectively of the signal distribution expected for an electron of energy E.

In addition the front and back parts of the lead scintillator stack were separately read out to see if comparing the front and back signals would improve the pion/electron separation. Table 4.5 shows the probability of pion misidentification with and without comparison of the front and back signals. The measurements show a small improvement for pion rejection for energies < 4 GeV with comparison of the front and back signals and no improvement for energies > 4 GeV. In the hadron arms electrons with energies below ~ 5 GeV are identified by the Cerenkov counters, so there was no advantage in a longitudinal subdivision of the lead scintillator stack.

The signal variation over the surface of a stack has been measured. In the direction parallel to the wavelength-shifter bar the signal was uniform, which was a result of the partial obscuration of the edge of the stack using copper strips. In the direction perpendicular to the wavelength-shifter bar a variation in the signal $\sigma_S/S \approx 10\%$ was observed which was due to the attentuation of light produced in the scintillator.

Fig 4.17 shows the measured signal as a function of distance from the wavelength-shifter bar. If the entrance point of a particle is unknown the energy resolution will be degraded by the signal variation across a stack.

A signal was seen when an electron passed through the wavelength-shifter bar. For an electron of energy 2 GeV a signal equivalent to an electron of energy 800 MeV entering a stack was seen.

The resolution of the shower counters was measured at higher energies by studying large angle Bhabha scattering events, Table 4.6 shows the resolution obtained from these events. The passage of electrons through the shower counter stack has been simulated using the EGS[72] program, the calculated resolutions are shown in Table 4.7. The test beam measurements agree well with the values calculated using the EGS program while the measurements obtained from Bhabha scattering events without fiducial volume cuts lie above the values calculated using the EGS program. In view of the large corrections applied to the experimental data and possible uncertainties in the intercalibration of the shower counters the agreement is good. The resolutions obtained from the test beam measurements, the Bhabha scattering events and the resolutions calculated using the EGS program are shown in Fig 4.18.

material	function
napthalene	primary fluor
butyl PBD	primary fluor
POPOP	secondary fluor
BBQ	wavelength shifter

Table 4·1 scintillator compounds used and their function

strip position (mms)	strip thickness (mms)
0	9
30	9
67	9
111	9
167	9
230	9
334	9
494	5

Table 4·2 position and thickness of the copper strips along the edge of the shower counter stack

run period	group				
	A	B	C	D	E
1600 – 1940	0·83	0·78	0·95	0·63	0·55
1941 – 2373	0·84	0·70	0·86	0·83	0·86
2374 – 2775	0·70	0·95	0·63	0·80	0·65
2776 – 2905	0·63	0·54	0·73	0·86	1·00
2906 – 3090	1·09	0·63	0·80	0·58	1·00
> 3090	0·54	0·78	0·95	0·65	1·00

Table 4·3 calibration factors, derived from Bhabha scattering events, for each counter group

energy (GeV)	resolution σ/E (%)
1·0	17·7 ± 2·1
2·0	12·8 ± 2·3
3·0	11·1 ± 2·6
4·0	10·9 ± 2·1

Table 4·4 shower counter energy resolution measured in an electron beam

energy (GeV)	probability of pion misidentification (%)	
	without correlation	with correlation
1·0	4·5	3·0
2·0	1·5	1·0
4·0	0·4	0·4

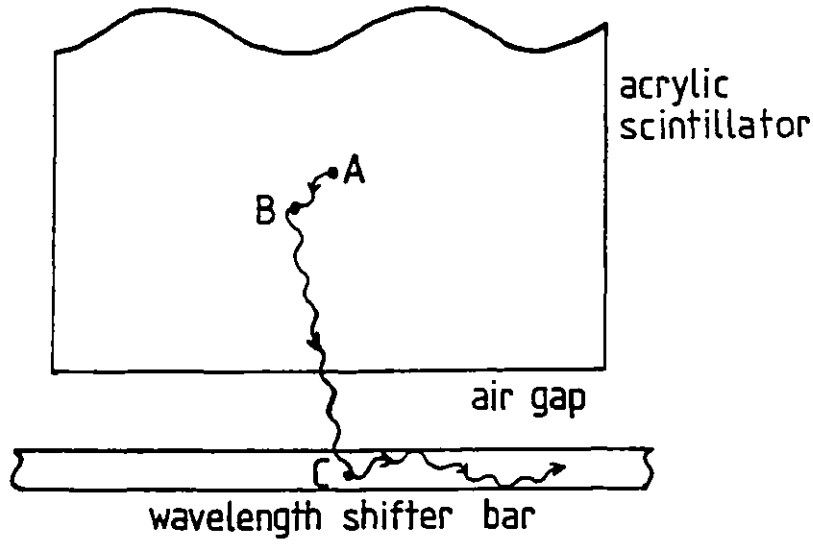
Table 4·5 probability of pion misidentification as an electron

energy (GeV)	resolution σ/E (%)	
	with fiducial volume cuts	without fiducial volume cuts
6·0	13·4 ± 1·7	19·1 ± 2·8
15·0	15·5 ± 2·1	22·6 ± 2·6

Table 4·6 shower counter energy resolution measured using Bhabha scattering data

energy (GeV)	resolution σ/E (%)
1·0	17·9 ± 1·1
2·0	11·9 ± 1·1
3·0	11·1 ± 1·1
4·0	10·6 ± 1·1
5·0	11·1 ± 1·1
8·0	13·6 ± 1·1
10·0	13·6 ± 1·1
12·0	14·5 ± 1·1
15·0	15·1 ± 1·1

Table 4·7 shower counter energy resolution calculated using the EGS Monte Carlo program



A) primary excitation
B) absorbsion of UV light and re-emition of blue light
C) absorbsion of blue light and re-emition of green light

Fig 4·1 schematic diagram of the light collection process using a wavelength shifter bar

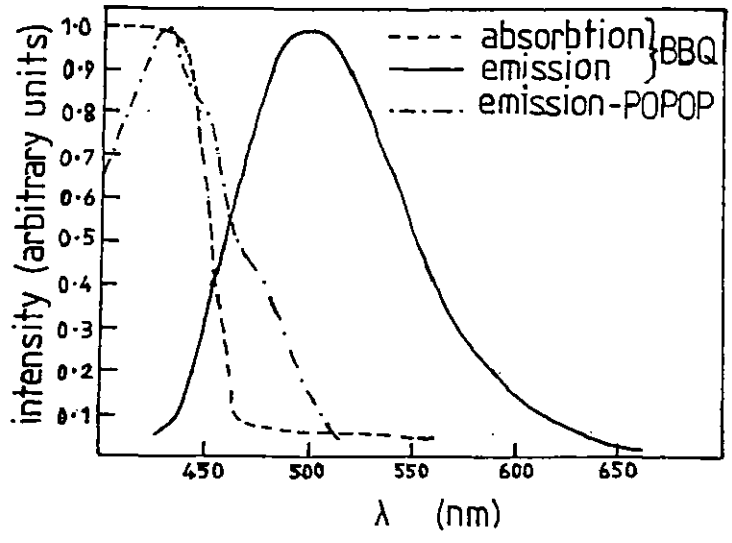


Fig 4·2 emission spectrum of POPOP and the emission and absorbtion spectra of BBQ

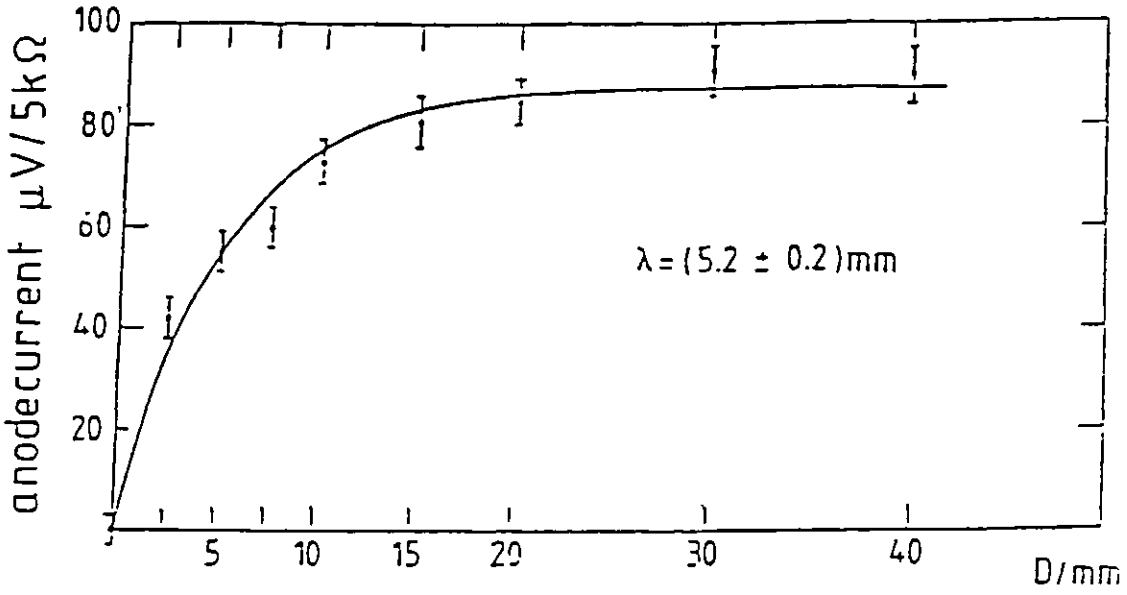


Fig 4 • 3 a measurement of the absorbtion length of scintillator light in BBQ

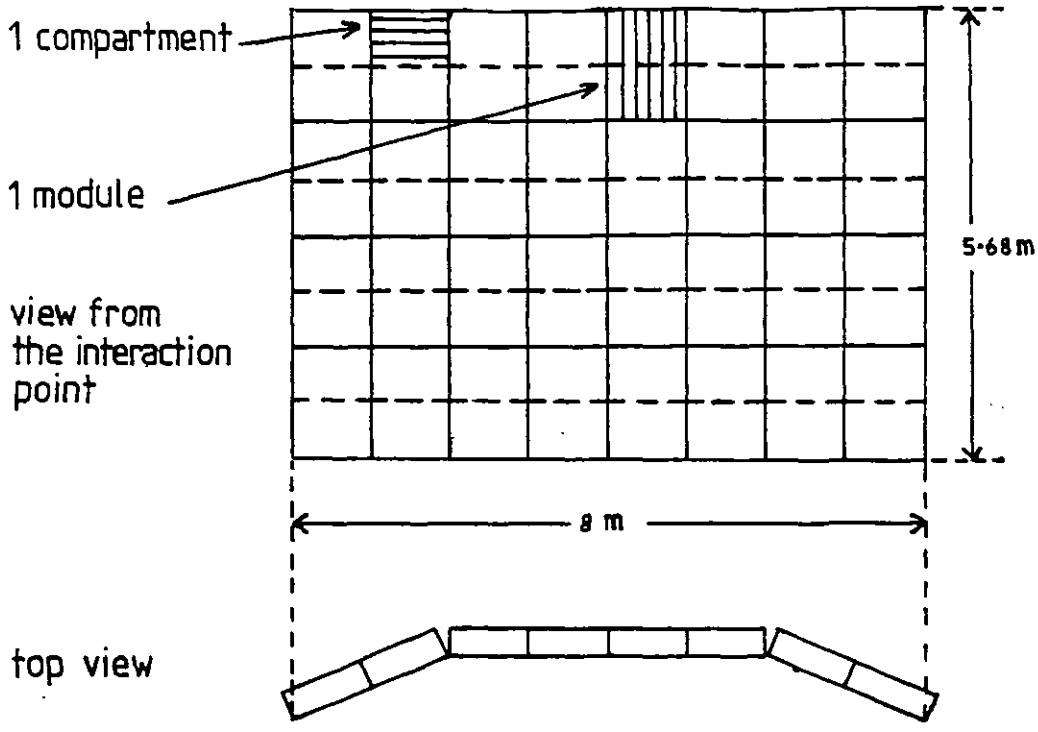
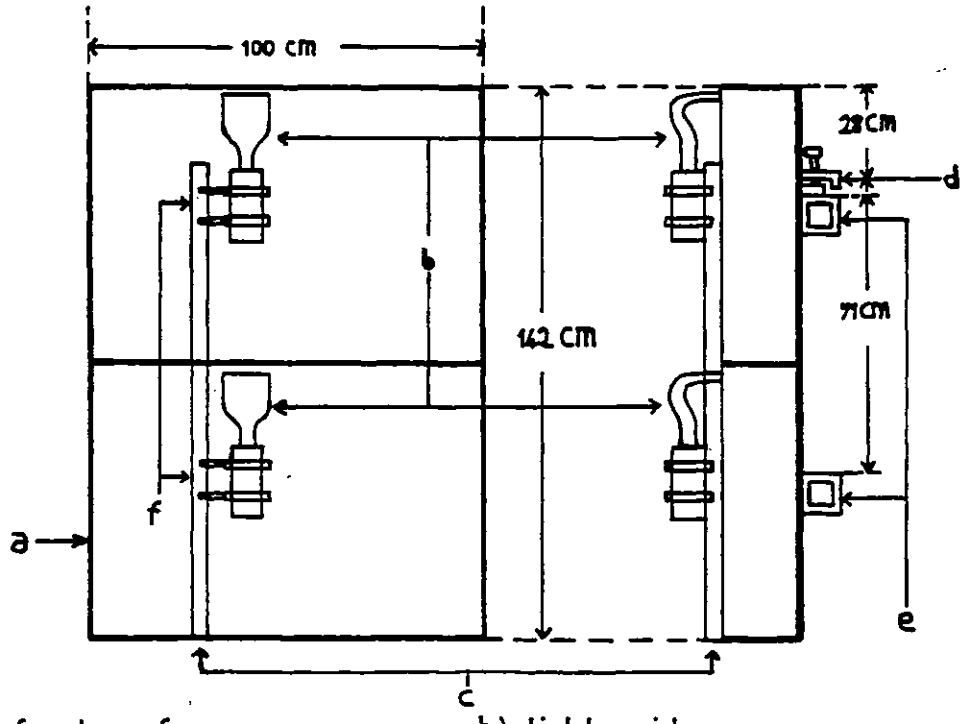
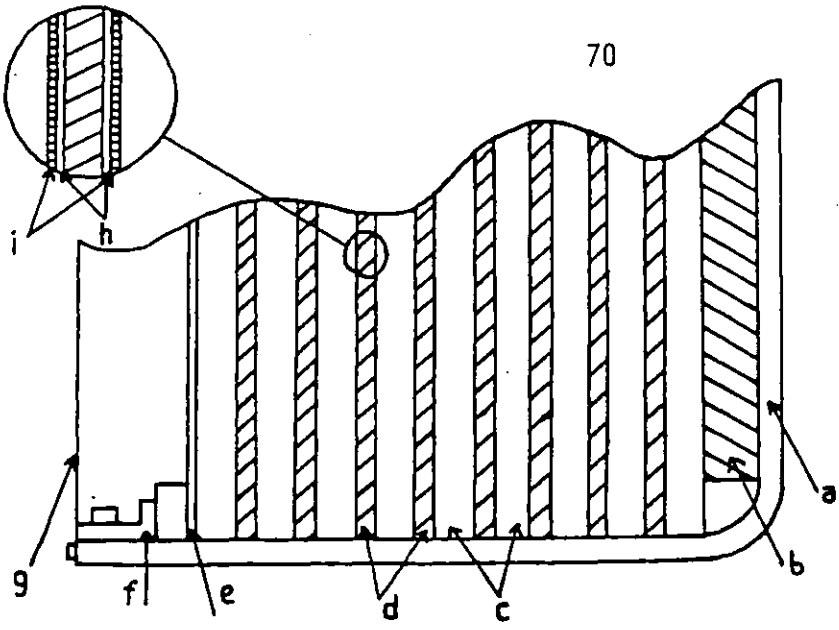


Fig 4·4 side and top view of the shower counter array in one hadron arm



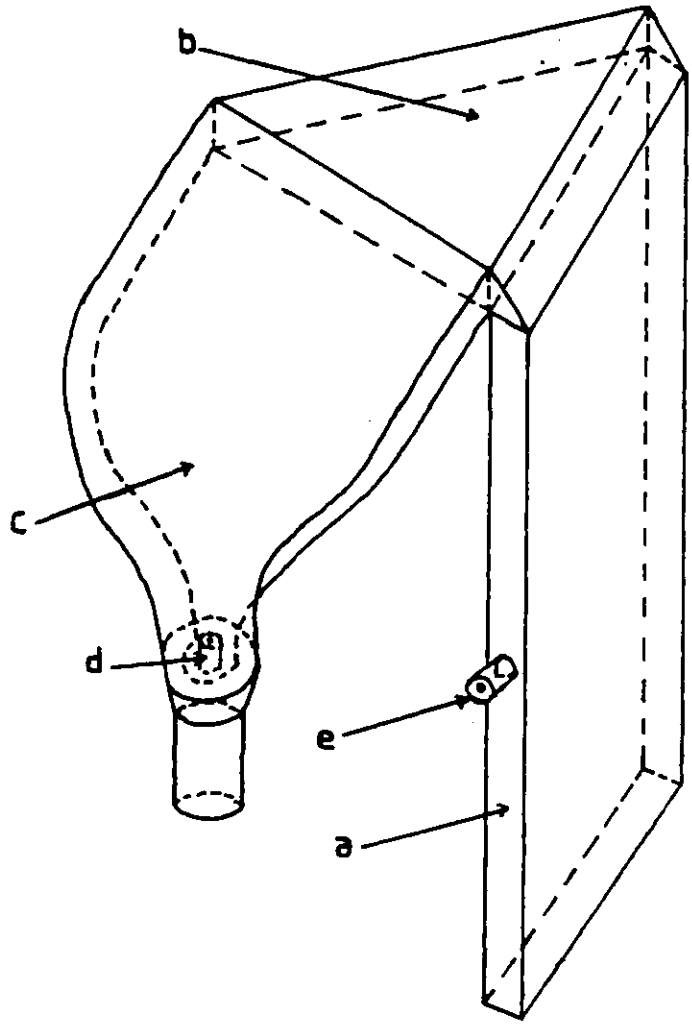
a) front surface
b) light guide
c) support for PM tubes
d) supporting hook
e) bars of muon filter
f) supporting clamp

Fig 4·5 side and front view of a shower counter module



a) iron wall
b) rubber mat
c) scintillator
d) lead
e) cover plate
f) bracket
g) top plate
h) polythene film
i) Al. foil

Fig 4·6 cross-sectional view of a shower counter stack



a) wavelength shifter bar
b) double prism
c) twisted light guide
d) led connector
e) fibre optic connector

Fig 4·7 the shower counter light collection system

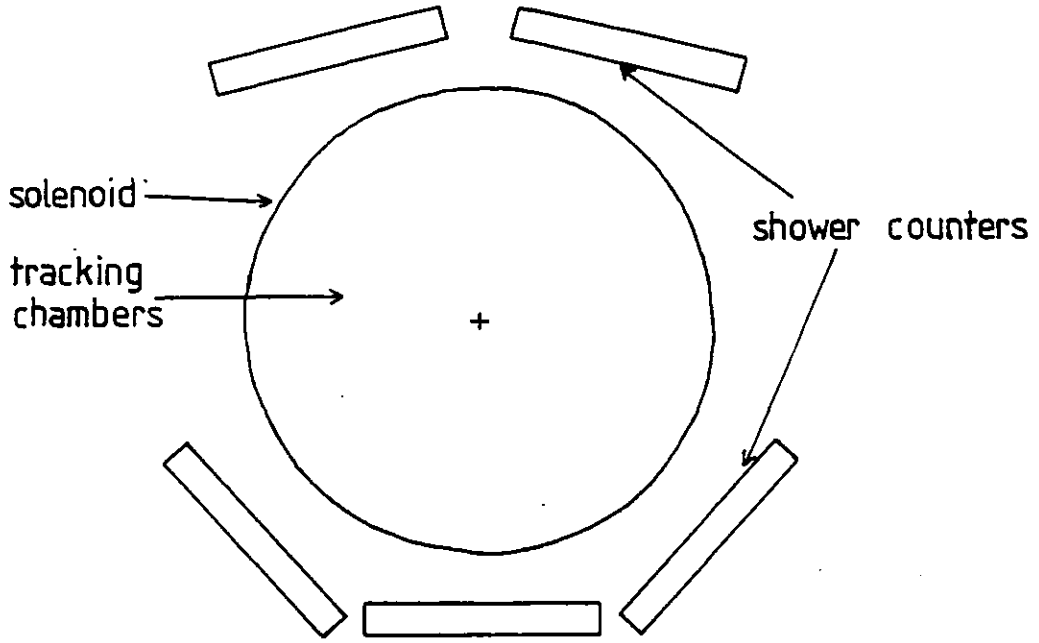


Fig 4·8 position of the shower counters around the solenoid during 1979

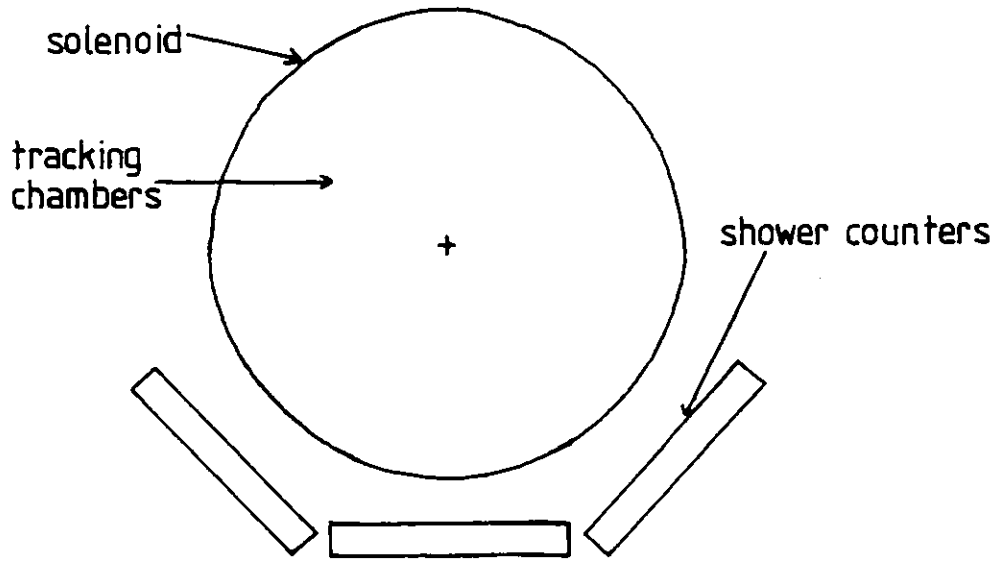


Fig 4·9 position of the shower counters around the solenoid during 1980

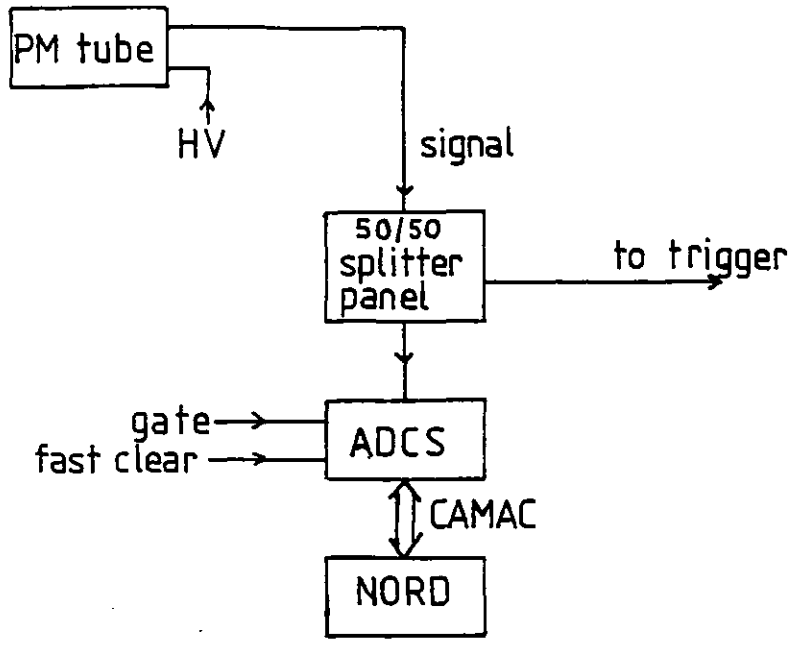


Fig 4·10 schematic diagram of the shower counter readout system

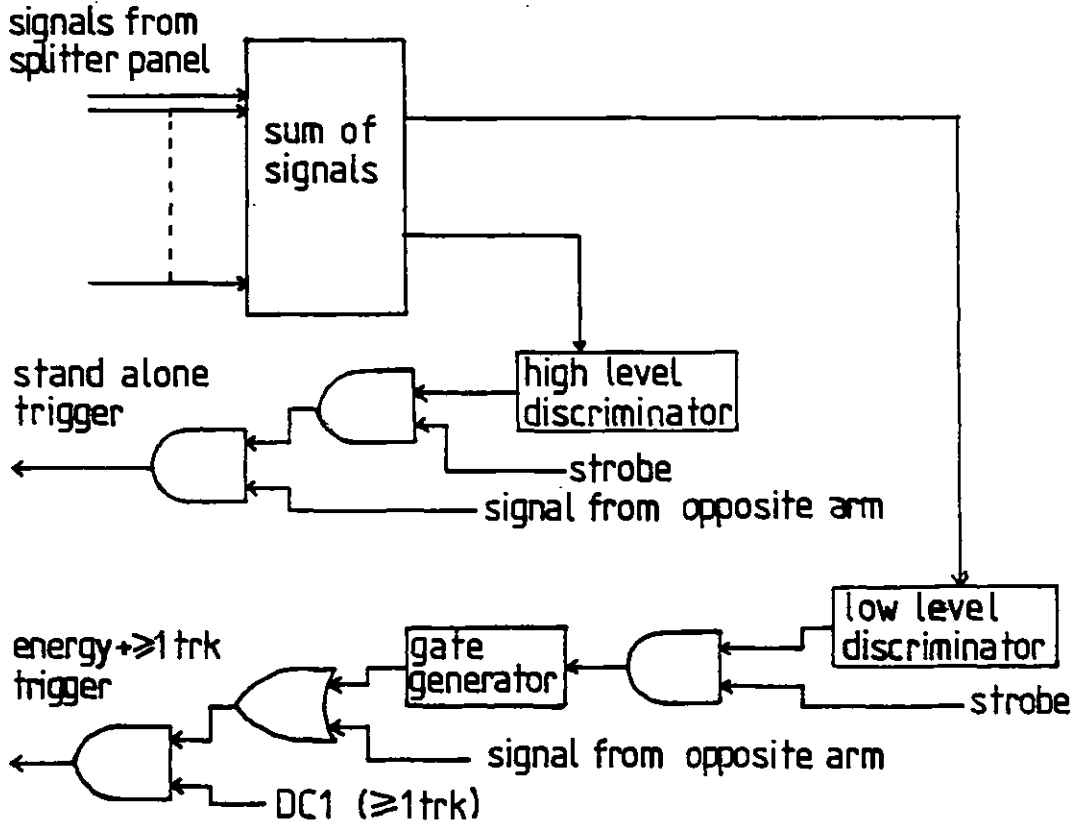


Fig 4·11 schematic diagram of the shower counter trigger system

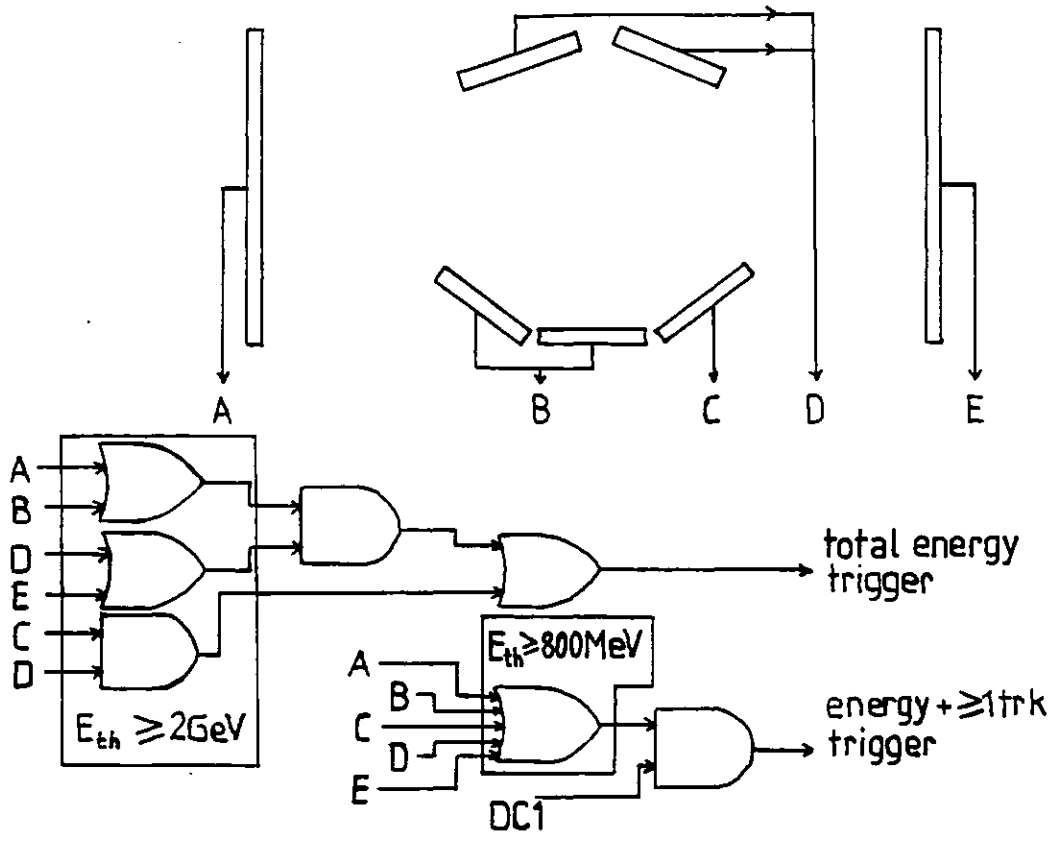


Fig 4·12 shower counter trigger system for the 1979 shower counter positions

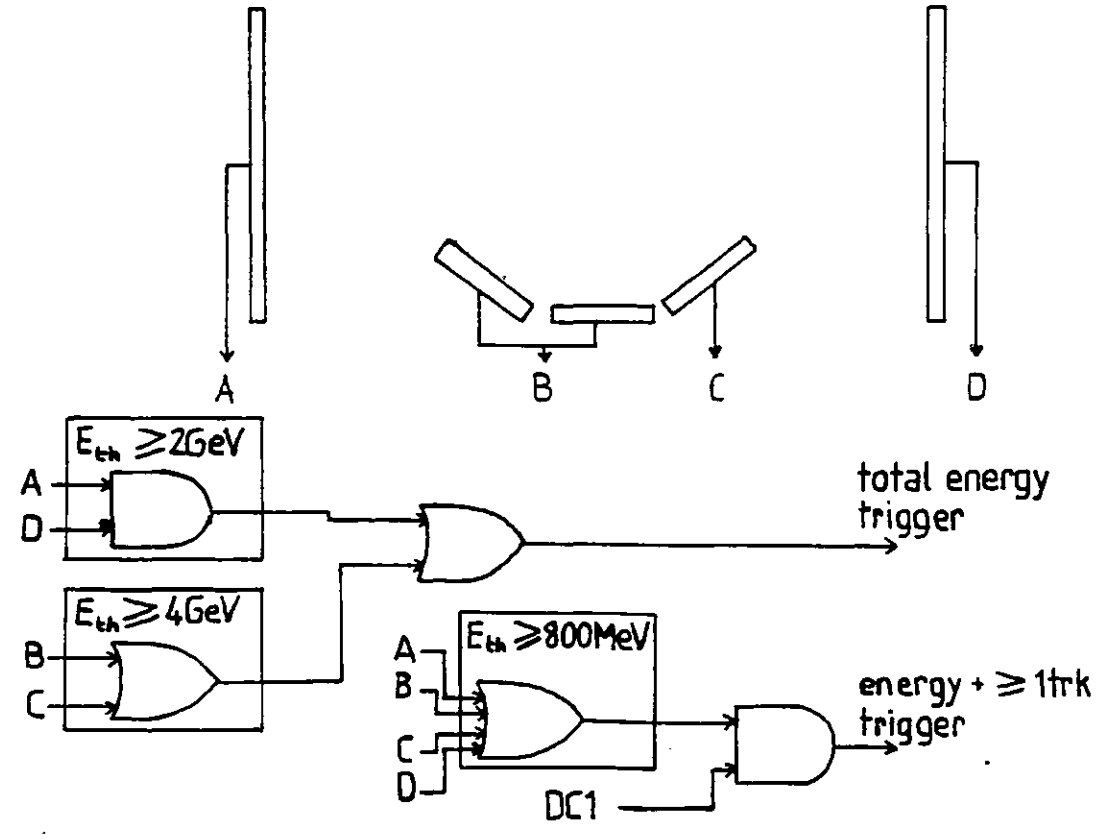


Fig 4·13 shower counter trigger system for the 1980 shower counter positions

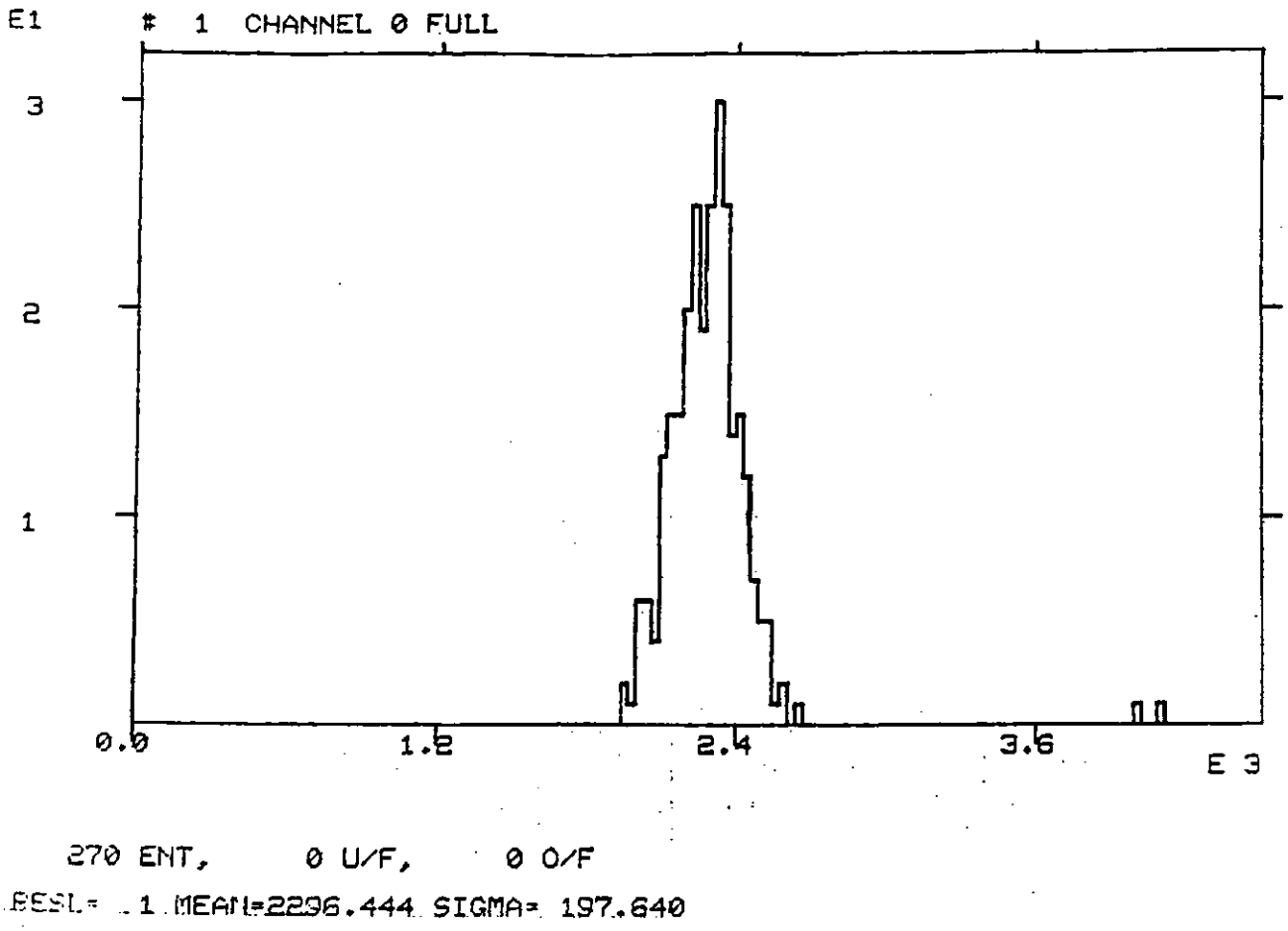


Fig 4·14 spectrum of ADC values for a shower counter recorded during a calibration runs

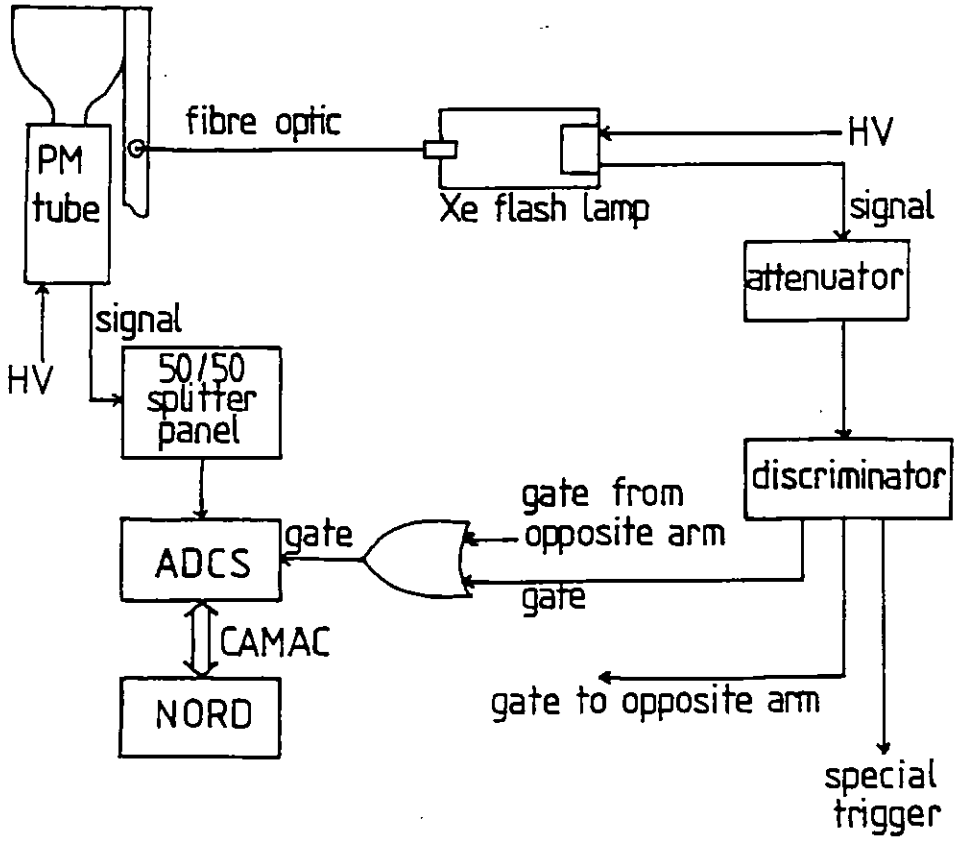


Fig 4·15 schematic diagram of the calibration system

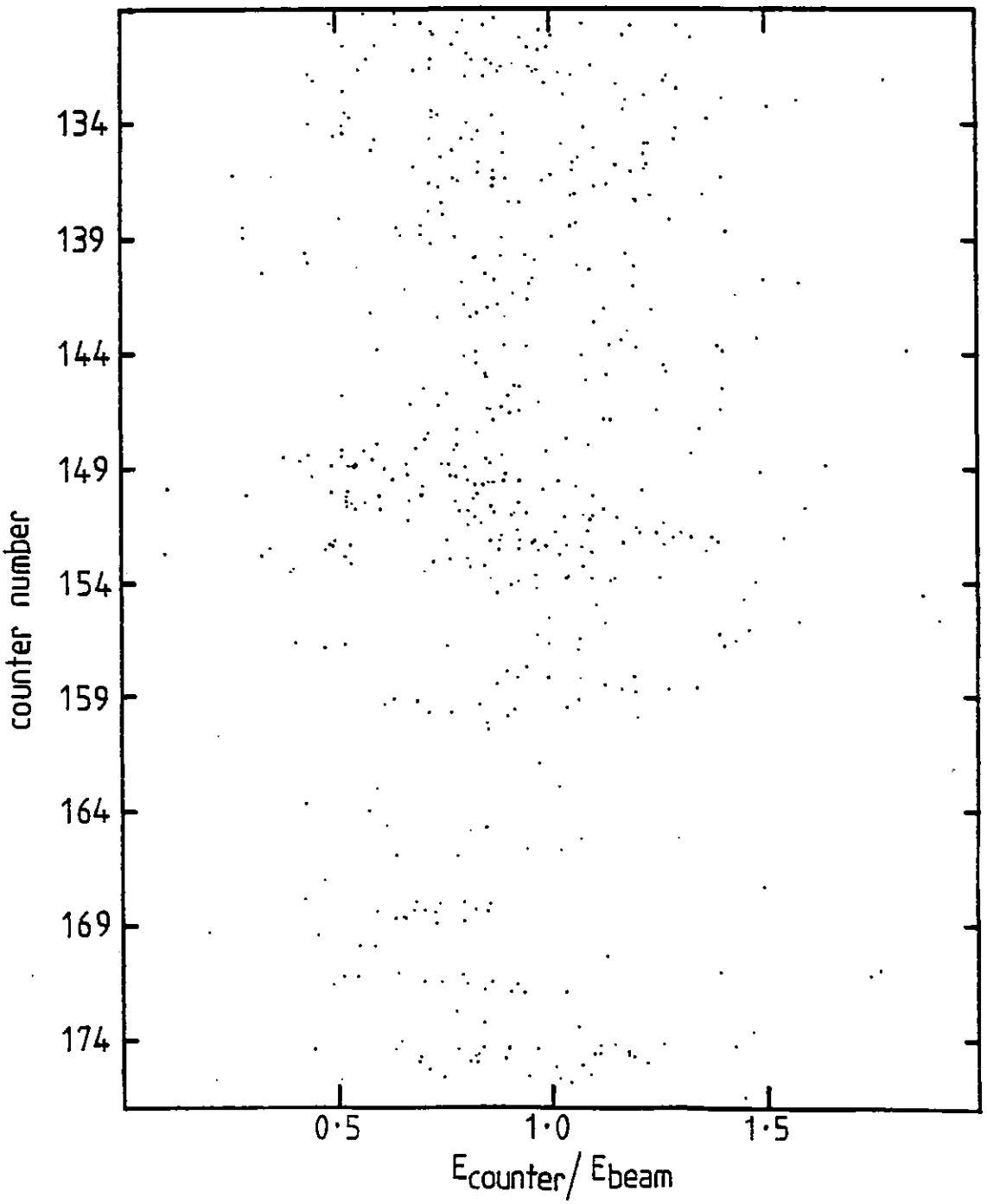


Fig 4·16 $E_{counter}/E_{beam}$ v. counter number for the shower counters below the solenoid

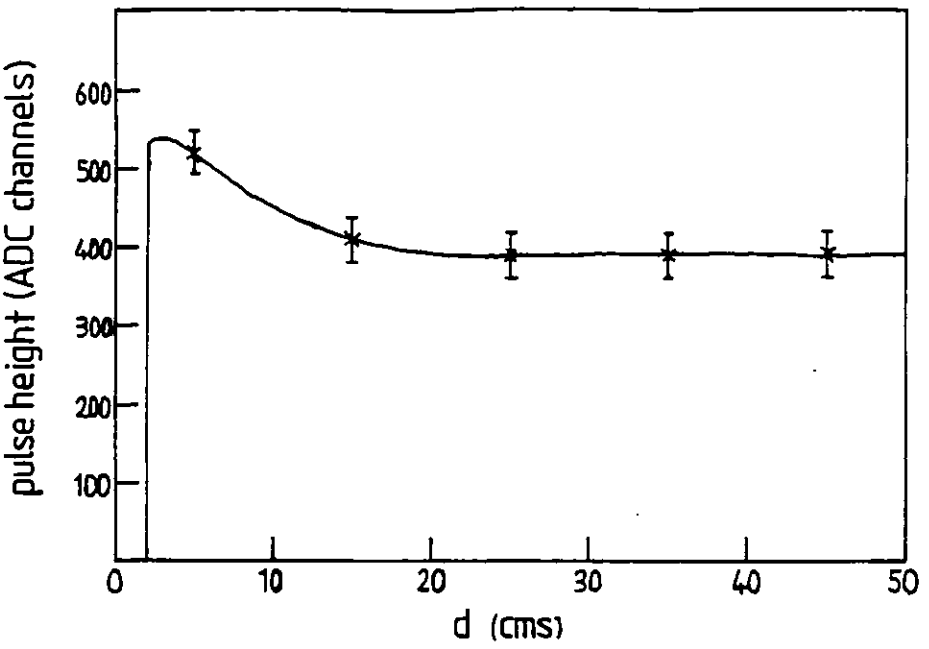


Fig 4·17 pulse height v. distance from the wavelength shifter bar

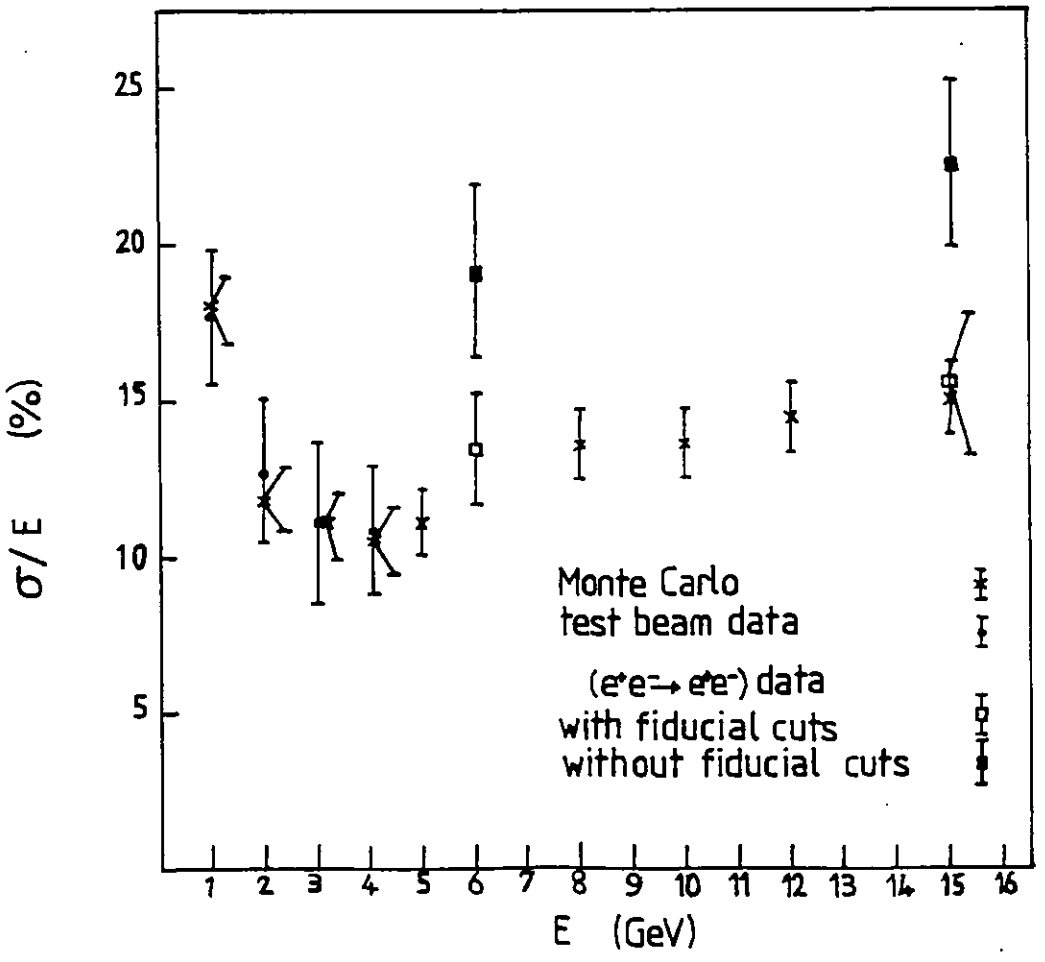


Fig 4·18 shower counter energy resolution (σ/E) v. energy (E)

CHAPTER 5

SHOWER COUNTER AND LABC ANALYSIS ROUTINES

5.1 Introduction

The raw data from the shower counters and LABC consist of ADC values for the PM tubes and the towers and strips respectively. Programs which convert the ADC values into energy measurements and assign clusters of deposited energy to charged particles and photons are described.

5.2 Shower counter analysis package

Shower counter information was accessed for an event by calling a subroutine 'NEUTRL'. The method used in 'NEUTRL' to convert the ADC values into energy measurements and the assignment of the deposited energy to charged particles and photons will be described below. A schematic diagram of the program is shown in Fig 5.1.

5.2.1 Calculation of energy deposits

The first task was to convert the shower counter ADC values into energy measurements. The ADC values were stored in the 'ADCS' and 'ADCN' data banks for the south and north arm shower counters respectively and pedestal values were stored in the 'PEDS' and 'PEDN' banks of the Run Library[73], with separate banks for each run. The ADC values were corrected by subtracting the pedestal values. To account for pedestal drift any ADC value after pedestal subtraction with less than 12 counts was zeroed.

The conversion of the corrected ADC values into an energy measurement in MeV was made using the following formula:

$$E_i(\text{MeV}) = \text{BHACAL}*\text{ADC}_i*10{,}000*\text{FACTOR}/\text{XeCAL}_i \qquad - 5.2.1$$

where ADC_i is the ADC value of channel i and XeCAL_i is the ADC value of channel i recorded using the Xenon lamp calibration system described in section 4.9. The light output of the reference Xenon lamp was equivalent to ~ 10,000 MeV and FACTOR is a shift applied to some counters due to a

difference in the light output of the other Xenon lamps used with respect to the reference lamp. An overall shift of the energy, described in section 4.8, was applied through the factor BHACAL, which normalised the spectrum of energies measured from Bhabha scattering events to the beam energy. Any energy deposit of less than 50 MeV was set to zero.

The calibration of the shower counters using the Xenon lamps assumed that the amount of light entering each of the counters was the same. This has been checked by plotting the energy spectrum measured in each counter for Bhabha scattering events (Fig 4.16). In some counters the energy spectrum obtained peaked below the beam energy, the most likely explanation for this is damage to some of the light fibres. For each of these counters an additional shift of the energy was applied. The limited statistics did not allow these factors to be accurately calculated and for some counters this correction was not attempted.

The calibrated energy deposits were stored as the 'BTSH' bank.

5.2.2 Projection of tracks

The next stage is the projection of charged particle tracks from the DC to the shower counters using the fitting parameters of the programs FOREST or MILL. The projection consisted of three parts:

A) Each track was projected to the ITOF counters assuming a constant magnetic field parallel to the z-axis.

B) Each track was transported through the solenoid in a series of discrete steps, with the magnetic field parameterised as parallel to the z-axis but linearly falling to zero in the radial direction. The parameterisation of the magnetic field in the coil was obtained by a comparison of the position of hits with the entry points of tracks in the muon counters from a large sample of cosmic ray events.

C) Each track was then projected to the shower counters assuming no magnetic field.

The shower counters were treated as rectangular groups. Using the point of intersection of a track with a counter group the counter struck was identified and the perpendicular distance 'd' to the wavelength-shifter bar was calculated. A correction due to the non linear response of the shower counter was made using the following algorithm:

$$\begin{aligned} d &> 20 \text{ cm} \quad \text{FACTOR} = 1 \\ d &\leq 20 \text{ cm} \quad \text{FACTOR} = 1/(1.4 - 0.02|d|) \end{aligned} \qquad - 5.2.2$$

Equation 5.2.2 was determined from the test-beam measurements shown in Fig 4.17.

5.2.3 Energy assignments

The energy deposited in the shower counters was associated with charged particles in the following way.

The shower counter modules struck by charged particles were determined, by projecting charged particle tracks from the DC to the shower counters, using the method described in section 5.2.2. If the measured energy loss in a module struck by a charged particle was $\leq$ 1 GeV all the energy was assigned to the charged particle. If the energy was > 1 GeV the momentum of the charged particle was compared with the energy and if the difference between these quantities was < 2.5 σ, the charged particle was considered to be an electron with all energy assigned to it. Otherwise the charged particle was treated as miniumum ionising with only 200 MeV, the measured mean energy loss of a minimum ionising particle in a shower counter, assigned to it.

The remaining energy, after the subtraction of the energy associated with charged particles, was assigned to photons.

A cluster finding program, which is described in section 5.2.4, was used to identify individual photons from the total energy in the shower counters which had been assigned to photons. The program could also be used to make an improved search for electron candidates by comparing the

momentum of each charged particle with the energy of the cluster associated with it.

Each identified photon had its direction cosines defined by the direction cosines of the centre of the shower counter containing the energy deposit.

5.2.4 Corrections for electrons and photons

For identified electrons and photons two further corrections for the amount of energy leaking from the back of the counters and for the angle of incidence with the counters were made. These corrections have been calculated by passing electrons and photons through a simulation of the shower counters using the EGS[72] program, for various energies and angles of incidence, and were parameterized by the following equations.

A) Photons

$$EC1_i = EC_i \cos\theta_i \qquad - 5.2.3$$

$$E_i = EC_i \{1 + (2EC1_i - 6)/48\} \{1 - 1/\cos\theta_i\} \qquad - 5.2.4$$

where θ_i is the angle of incidence and EC_i is the initial energy of photon i. The dependence on ϕ_i is small due to the geometry of the shower counters and was neglected.

$$EF_i = E_i + 0.02\ E_i^2 \qquad - 5.2.5$$

This correction accounted for leakage from the rear of the shower counters. An additional factor of $80/\sin\theta_i$ MeV was added to account for the average energy deposit due to showering in the solenoid.

B) Electrons

$$EC1_i = 1.11.E_i.FACTOR_i \qquad - 5.2.6$$

$$EC2_i = FACTOR_i \{1 + 2\ EC1_i/43\} \{1 - 1/\cos\theta_i\} \qquad - 5.2.7$$

$$EC3_i = 1.11\ E_i\ EC2_i \qquad - 5.2.8$$

where θ_i is the angle of incidence, E_i the initial energy and $FACTOR_i$ the point of incidence correction of electron i. Again the ϕ_i dependence was neglected.

$$EF_i = EC3_i + 0.02\ EC3_i^2 \qquad - 5.2.9$$

This correction accounted for leakage from the rear of the shower counters.

5.2.5 Cluster finding Algorithm

A cluster finding algorithm was used to select events from Bhabha scattering and electron-positron annihilation into gamma rays.

The shower counter module with the highest energy deposit defined a cluster and any energy in the surrounding 8 modules was added to the cluster energy. The direction of the cluster was the energy weighted sum of the direction cosines of the modules containing energy with the direction cosines of each module defined at its centre. All energy assigned to a cluster was removed and using the same procedure a search was made for additional clusters in the remaining modules.

Clusters assigned to charged particles were considered to be electrons if the event passed the Bhabha selection described in chapter 6 and they had more than 2 GeV deposited energy.

The corrections described for electrons and photons in the previous section were applied to each identified cluster.

5.3 LABC analysis package

LABC information was accessed for an event by calling a subroutine 'LABREC'. A schematic diagram of the program is shown in Fig 5.2.

5.3.1 Calibration of energy deposits

The ADC values of the towers and strips which were the raw data of the LABC were stored in the LIAR bank. The first stage of the program separated this information into separate banks (LIAB 101-108) with one for each of the barrel modules. The format of the LIAR bank was checked and all repeated addresses were removed. The address of non zero ADC values were converted into internal coordinates which were then stored along with the device type in the LIAB banks.

Calibration of the ADC values of the towers was performed using

Bhabha scattering events, with shifts calculated for each module from events collected over a period of a month. The shift was calculated by summing all the tower ADC values in each module associated with a charged particle and then normalising the resulting spectrum to the beam energy.

At this stage noisy towers and strips were also removed. The calibrated data was stored in banks (LIAB 1-8) with a separate bank for each module.

5.3.2 Cluster finding algorithm

A cluster finding algorithm was used to search for clusters of towers in the LABC[74]. The algorithm used the calibrated data stored in the LIAB 1-8 banks with a separate search performed in each module.

The program first performed a one-dimensional search for clusters in the ϕ strips, with the ϕ value of each cluster taken as the centre of gravity of the ϕ strips in the cluster. The ϕ value of each cluster was taken as the start point of a scan along the module in the z direction, searching for energy deposits in the front towers. The front towers were summed in the z and ϕ direction for a maximum of $\pm$ 3 front towers unless a layer of front towers containing no energy was crossed. The θ value of the cluster was taken as the centre of gravity of the z-strips associated with the front towers. If two clusters were not separated by a layer of front towers containing no energy the energy of the front towers was shared between the two clusters. The energy deposits of the back towers associated with the front towers of a cluster were added to the cluster energy. If no strip information was available then the front towers were used to define the θ and ϕ coordinates of the clusters. All clusters of less than 50 MeV energy were not considered. The front to back energy ratio for each cluster was calculated and all clusters where $^{F}/_{B} < .1$ or $^{F}/_{B} > 10$ were rejected.

5.3.3 Cluster assignments

Charged tracks were assigned to clusters if the angle θ between the

cluster and the track was less than 3°. If more than one track satisfied this condition then the track with the smallest θ was chosen. Any cluster unassociated with a charged track was considered to be a photon.

Clusters assigned to electrons and photons had corrections applied for energy leakage and the angle of incidence with the barell module. The corrections were calculated using the EGS[72] program.

For each cluster a data bank containing the cluster parameters was created.

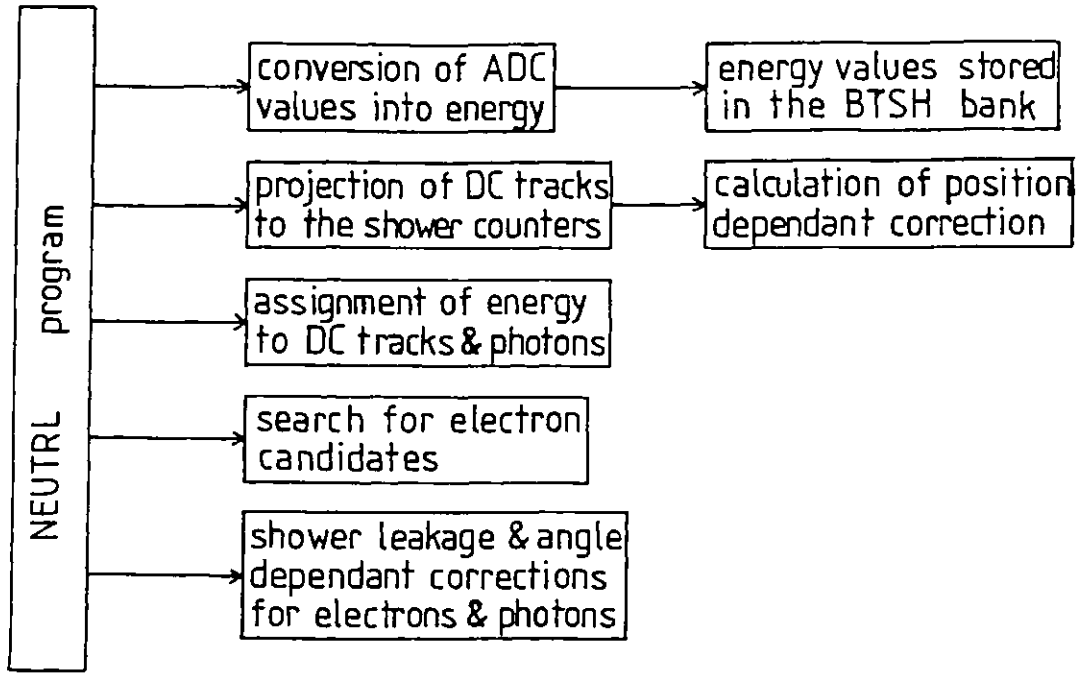


Fig 5·1 schematic diagram of the shower counter program NEUTRL

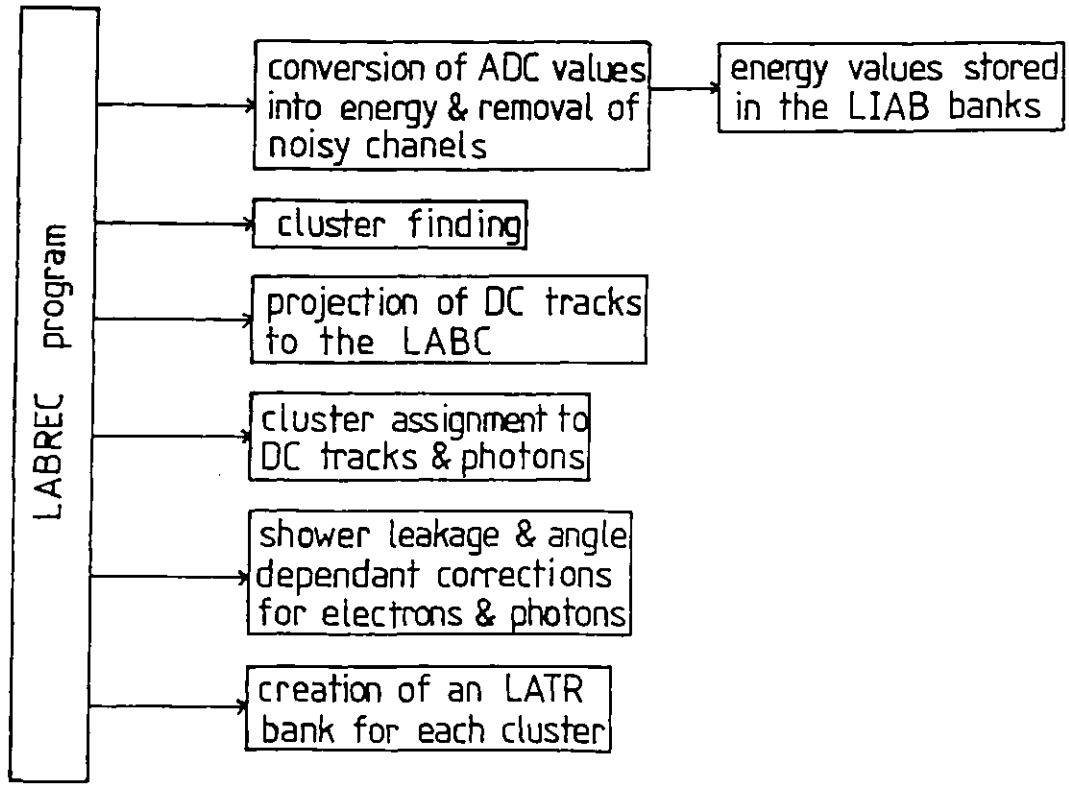


Fig 5·2 schematic diagram of the shower counter program LABREC

CHAPTER 6

ANALYSIS OF BHABHA SCATTERING ($e^+e^- \rightarrow e^+e^-$)

6.1 Introduction

In this chapter an analysis of the reaction $e^+e^- \rightarrow e^+e^-$ is presented. At PETRA where the maximum energy in each beam is ~ 18 GeV, QED can be tested at values of Q^2 up to ~ 1300 GeV^2 which allows a test of the point like nature of the electron to be made. A theoretical description of Bhabha scattering is given, followed by a discussion of the procedures used to select this type of event. The contributions from background processes are calculated and a Monte-Carlo program used to calculate acceptances is described.

The cross-section is evaluated for centre of mass energies, W, between 12 and 36.6 GeV and using the angular distribution of events at an average W of 34.8 GeV the cut off parameters $\Lambda\pm$ are calculated.

6.1.1 Bhabha scattering cross-section

The lowest order differential cross-section, calculated from the two graphs shown in Fig 1.8 is:[33]

$$\frac{d\sigma_o}{d\Omega} = \frac{\alpha^2}{2s}\left[\frac{q'^4 + s^2}{q^4} + \frac{2q'^4}{q^2 s} + \frac{q'^4 + q^4}{s^2}\right] \qquad - 6.1.1$$

where $q^2 = -s\sin^2(\theta/2)$, $q'^2 = -s\cos^2(\theta/2)$, s is the centre of mass energy squared and the mass of the electron has been neglected. In this equation the first term comes from the space like graph (Fig 1.8 a), which dominates for small values of θ, the third term comes from the time like graph (Fig 1.8 b) and the second term results from interference between the two graphs.

Equation 6.1.1 can be rewritten in the form:

$$\frac{d\sigma_o}{d\Omega} = \frac{\alpha^2}{4s}\left[\frac{3 + \cos^2\theta}{1 - \cos\theta}\right]^2 \qquad - 6.1.2$$

If the electrons and positrons are polarised with a transverse

polarisation P the lowest order differential cross-section would be:

$$\frac{d\sigma_o}{d\Omega} = \frac{\alpha^2}{4s} \left\{ \left[\frac{3 + \cos^2\theta}{1 - \cos\theta} \right]^2 - P^2(1 + \cos\theta)^2 \cos 2\phi \right\} \qquad - 6.1.3$$

As no beam polarisation has been seen at PETRA equation 6.1.2 will be used.

6.1.2 Radiative corrections

The lowest order cross-section is modified due to contributions from higher order graphs. These graphs contribute to the final state ($e^+e^- \rightarrow e^+e^-\gamma$) which is indistinguishable in the detector from the lowest order final state ($e^+e^- \rightarrow e^+e^-$), when the γ is of low energy or is not detected. The graphs used to calculate the radiative corrections are shown in Fig 1.9 and the cross section for Bhabha scattering is modified to:

$$\frac{d\sigma}{d\Omega} = \frac{d\sigma_o}{d\Omega} [1 + \delta(\theta,\phi)] \qquad - 6.1.4$$

where $d\sigma_o/d\Omega$ is the lowest order (α^2) cross-section and $\delta(\theta,\phi)$ is the radiative correction to order (α^3). The radiative corrections are calculated using the method of Berends and Kleiss[75].

The first 8 graphs in Fig 1.9 account for the contribution from initial and final state Bremsstrahlung, the next graphs describing vertex corrections, box diagrams and vacuum polarisation of the photon propagator contribute to order (α^3) via interference with the lowest order diagrams (Fig 1.8). The vacuum polarisation due to hadrons is calculated from the total cross-section for $e^+e^- \rightarrow$ hadrons using a dispersion relation[76].

Initial state radiation and large angle final state radiation corrections lead to an acollinearity between the final state electron and positron. The value of the radiative correction is characterised by a threshold energy E_{th} on the final state electron and positron and a limit on ξ the acollinearity angle between them. At W = 34.8 GeV the average value of the radiative correction is ~ -4% for E_{th} = 4 GeV and ξ = 10°.

6.1.3 Tests of QED

In the derivation of equation 6.1.1 describing the differential cross-section for Bhabha scattering all interactions and particles are assumed to be point like. Any deviation from this QED prediction can be parameterised in terms of form factors.

The matrix element describing Bhabha scattering is constructed from the photon propagator $D^{\mu\nu} = -F_1(q^2)\, g^{\mu\nu}/q^2$ and from the vertex functions $\Gamma_\mu = \gamma_\mu F_2(q^2)$, where $F_1(q^2)$ and $F_2(q^2)$ are separate form factors which are unity in unmodified QED. The differential cross-section is then proportional to the product $|F_2^2(q^2)F_1(q^2)|^2$. A joint form factor $F(q^2) = F_2^2(q^2)F_1(q^2)$ is defined as the separate form factors are indistinguishable.

For small deviations from unity the form factor can be expressed as[77]:

$$F(q^2) = 1 \mp \frac{q^2}{q^2 - \Lambda^2_\pm} \qquad - 6.1.5$$

where $\Lambda\pm$ is called the cut off parameter.

For Bhabha scattering two form factors for the spacelike and timelike amplitudes are introduced and the differential cross-section becomes:

$$\frac{d\sigma}{d\Omega} = \left[\frac{q'^4 + s^2}{q^4}\,|F_s(q^2)|^2 + \frac{2q'^4}{q^2 s}\,\mathrm{Re}(F_s(q^2)F_t^*(s)) + \frac{q'^4+q^4}{s^2}|F_t(s)|^2\right]\frac{\alpha^2}{2S} \qquad 6.1.6$$

where $q^2 = -s\sin^2(\theta/2)$, $q'^2 = -s\cos^2(\theta/2)$, s is the centre of mass energy squared and $F_s(q^2)$, $F_t(s)$ represents the spacelike and timelike form factors respectively.

Expressing $F_s(q^2)$ and $F_t(s)$ using equation 6.1.5 with $s, q^2 \ll \Lambda^2$ and neglecting terms of higher order in $1/\Lambda^2$ equation 6.1.6 becomes:

$$\frac{d\sigma}{d\Omega} = \frac{\alpha^2}{4s}\left(\frac{3 + \cos^2\theta}{1 - \cos\theta}\right)^2 \left[1 \mp \frac{s}{\Lambda^2_{s\pm}}\,\frac{(9 - 6\cos\theta - 2\cos^3\theta - \cos^4\theta)}{(3 + \cos^2\theta)^2}\right.$$

$$\left. \mp \frac{s}{\Lambda^2_{t\pm}}\,\frac{(6\cos\theta - 6\cos^2\theta + 2\cos^3\theta - 2\cos^4\theta)}{(3 + \cos^2\theta)^2}\right] \qquad - 6.1.7$$

Setting $\Lambda_s = \Lambda_t$ and $\lambda = \mp 1/\Lambda^2$ equation 6.1.7 becomes:

$$\frac{d\sigma}{d\Omega} = \frac{\alpha^2}{4s}\left(\frac{3+\cos^2\theta}{1-\cos\theta}\right)^2\left[1 + 3s\lambda\frac{(1-\cos^2\theta)}{(3+\cos^2\theta)}\right] \qquad - 6.1.8$$

The cut off parameter Λ can be used to determine a distance above which QED is valid. The uncertainty principle relates Λ to a distance δr by substituting $\delta p = \Lambda$:

$$\delta r \sim \hbar c/\Lambda \qquad - 6.1.9$$

6.1.4 Weak Interaction effects in Bhabha scattering

At the highest PETRA energies the weak interaction becomes more important to Bhabha scattering. In models with one neutral vector boson, Z^o, graphs involving Z^o exchange (Fig 1.10) contribute to the cross-section along with the graphs involving virtual photon exchange (Fig 1.8). The matrix element calculated from all these graphs is[41]:

$$M = \frac{e^2}{t}\bar{u}\gamma_\mu u\bar{v}\gamma^\mu v - \frac{e^2}{s}\bar{u}\gamma_\mu v\bar{v}\gamma^\mu u$$

$$+ \frac{1}{t-M_z^2}\bar{u}\gamma_\mu(g_v+g_A\gamma_5)u\bar{v}\gamma^\mu(g_A+g_v\gamma_5)v - \frac{1}{s-M_z^2}\bar{u}\gamma_\mu(g_v+g_A\gamma_5)v\bar{v}\gamma^\mu(g_v+g_A\gamma_5)u \qquad - 6.1.10$$

where u and v are the electron and positron spinors respectively, g_v and g_A are the vector and axial vector weak neutral coupling constants and M_z is the mass of the Z^o.

From this matrix element the cross-section for Bhabha scattering is written as[41]:

$$\frac{d\sigma}{d\Omega} = \frac{\alpha^2}{8s}\left[4B1+(B3+B2)(1+\cos^2\theta)+2(B3-B2)\cos\theta\right] \qquad - 6.1.11$$

with $B1 = \left(\frac{s}{t}\right)^2 |\, 1 + (g_v^2 - g_A^2)\xi\,|^2$

$$B2 = |\, 1 + (g_v^2 - g_A^2)\chi|^2 \qquad - 6.1.12$$

$$2B3 = |\, 1 + \frac{s}{t} + (g_v+g_A)^2\left(\frac{s}{t}\xi+\chi\right)|^2 + |1 + \frac{s}{t} + (g_v-g_A)^2\left(\frac{s}{t}\xi+\chi\right)|^2$$

$$\text{and} \quad \chi = \frac{G_F M_Z^2}{2\sqrt{2}\pi\alpha} \frac{s}{s-M_Z^2+iM_Z\Gamma}, \quad \xi = \frac{G_F M_Z^2}{2\sqrt{2}\pi\alpha} \frac{t}{t-M_Z^2+iM_Z\Gamma} \qquad - 6.1.13$$

G_F is the fermi coupling constant and Γ is the width of the Z^0 boson. In the standard model[34] $g_V = \frac{1}{2}(1-4\sin^2\theta_W)$, $g_A = -\frac{1}{2}$ and $M_Z = 74.6/\sin 2\theta_W$ GeV/c^2, where $\sin^2\theta_W$ is a free parameter to be determined by experiment. The μ pair cross-section can be obtained from equations 6.1.11, 6.1.12, 6.1.13 by setting s/t to zero.

The total cross-section gives information on the vector coupling g_V. Assuming the measured value[78] of $\sin^2\theta_W = 0.228$ the change in the total cross section is too small to be measured. The axial vector coupling g_A modifies the Bhabha angular distribution from the QED prediction. Fig 6.1 shows the deviation as a function of $\cos\theta$ at W = 35 GeV for $\sin^2\theta_W = 0.25$.

6.2 Event selection

Bhabha events were selected from the 'Milled' 2-prong data-set produced by the program 'BHASEL'. In addition to Bhabha events this data-set contained events from muon and tau pair production, gamma-gamma scattering to leptons, beam-gas scattering and cosmic ray events. The cosmic ray contamination can be easily seen by looking at the phi distribution of tracks (Fig 6.2) which shows an excess of events at angles corresponding to the vertical direction.

The following cuts were applied to select Bhabha events:

a) the number of tracks, NTRK = 2

b) $\sum_{i=1}^{NTRK} q_i = 0$, where q_i is the charge of track i.

Cut a) removed events with an electromagnetic shower in the material of the detector before the drift chamber and cut b) rejected events with a mis-assignment of the charge, which results from the finite resolution in the curvature measurement of tracks.

At Ebeam = 6 GeV, $\simeq$ 0.1% of events and at Ebeam = 17.4 GeV, $\simeq$ 1.4% of events have the wrong charge assignment.

c) the event was triggered by the topology trigger (DCII)

Bhabha events can be selected by several independent triggers with different acceptance and efficiency. Cut c) removed a trigger bias by selecting events from the topology trigger only.

d) $(d_{o1}^2 + d_{o2}^2)^{\frac{1}{2}} \leq 1$ cm

e) $(Z_{o1}^2 + Z_{o2}^2)^{\frac{1}{2}} \leq 5$ cm

f) $-2ns \leq (t_{meas} - t_{pred})_i \leq 4ns$

Cuts d) and e) required tracks to come from a small region around the interaction point and cut f) required the measured time of flight, t_{meas}, to be consistent with the time of flight, t_{pred}, calculated from the path length of the track, for each track i. The distributions of d_o, Z_o and t_{meas} are shown in figs 6.3, 6.4, 6.5 respectively after cuts a) - f). These cuts removed most of the cosmic ray background. The ϕ distribution of tracks (fig 6.6) is now flat consistent with no measured beam polarisation.

g) P_i >4 GeV/c, Ebeam >15 GeV (>2 GeV/c, Ebeam = 6 GeV)

h) acollinearity angle $\xi \leq 10°$

Events from gamma-gamma scattering to leptons are characterised by a low track momentum P_i and an acollinearity angle ξ which is not strongly peaked at small angles, as is the case for Bhabha events. The momentum spectrum of tracks (Fig 6.7) shows a clear separation of the two classes of events. Cuts g) and h) then removed most of the gamma-gamma scattering events.

i) $|\cos\theta_i| \leq .8$

This ensured that each track passed through every DC layer and intersected the ITOF counters.

Events that passed these cuts formed the Bhabha data sample. The

surviving backgrounds are calculated in section 6.3.

Figs 6.8, 6.9 and 6.10 show 3 candidate Bhabha events at W = 12 GeV, W = 30.5 GeV and W = 35 GeV respectively.

6.3 Background estimation

In this section the backgrounds to Bhabha scattering discussed previously are calculated.

a) Cosmic ray and Beam-gas scattering

The contributions from beam-gas scattering and cosmic ray events were determined from the observed Z_0 distribution after the cuts, (excluding the Z_0 cut), described in section 6.2 had been applied. In both types of event the vertex, (defined as the intersection point of both tracks), can occur at any point along the beam pipe, which defines the z-axis. Tracks with $|Z_0| > 8$ cm were classed as from background events. The contamination was then estimated by extrapolating these events into the region $(Z_{01}^2 + Z_{02}^2)^{\frac{1}{2}} \leq 5$ cm assuming a flat distribution and was calculated to be $\lesssim 0.27\%$. Fig 6.11 shows a plot of Z_{01} vs Z_{02} with the boundaries $|Z_0| > 8$ cm and $(Z_{01}^2 + Z_{02}^2)^{\frac{1}{2}} \leq 5$ cm indicated.

b) Gamma-gamma scattering to leptons

The background from gamma-gamma scattering to leptons was calculated using a Monte Carlo program. Events were generated[79] from the matrix element calculated from the graphs shown in Fig 6.12 and final state particles were passed through a detector simulation program. The cuts imposed by the trigger, the effects of interactions of particles in the material before the drift chamber and the resolution of the drift chamber were included in the program.

The contamination was then measured by passing accepted events through the Bhabha selection cuts and was calculated to be $\lesssim 0.08\%$.

c) Tau pair production

The background resulting from tau pair production was calculated

using a Monte-Carlo event generator. Events were calculated correct to order (α^3)[75] and the taus generated were allowed to decay with branching ratios given by the world average measurements[80]. Final state particles were passed through a detector simulation program described in section 6.4 and then through the Bhabha selection cuts.

From the surviving events a contamination of 0.75% at Ebeam = 17.4 GeV was calculated.

d) Muon pair production

This is the major source of background in the Bhabha scattering data. The contribution from it was calculated in the same way as the contribution from tau pair production using a muon pair event generator[75], with events calculated correct to order (α^3).

The contribution of this process was calculated to be 4.86% at Ebeam = 17.4 GeV.

Other processes that could contribute to the background are $e^+e^- \rightarrow q\bar{q}$ and $e^+e^- \rightarrow \gamma\gamma$ where both photons convert in the material before the drift chamber. The contamination from both these processes was calculated to be less than 0.1%.

All the backgrounds apart from muon and tau pair production were neglected due to their small size. The contributions due to muon and tau pair production for different values of the beam energy are given in Table 6.1.

6.4 Monte Carlo simulation of Bhabha scattering

A Monte Carlo program was used to calculate the acceptance of the reaction $e^+e^- \rightarrow e^+e^-$. The program, which is described below, consisted of an event generator and a simulation of the components of the detector inside the solenoid, including the chain of programs described in chapter 3.

Accepted monte-carlo events were stored in the same way as real events allowing the same analysis routines to be used.

6.4.1 Event generator

Events were generated using the method of Berends and Kleiss[75]. The final states e^+e^- and $e^+e^-\gamma$ were produced correct to order (α^3), assuming no polarisation effects, from the diagrams shown in Fig 1.8 and Fig 1.9.

6.4.2 Detector simulation

The detector simulation program 'SIMPLE'[81] was used to simulate the passage of particles through the material and tracking chambers of the detector.

The material of the detector, listed in Table 6.2, was parameterised as 6 layers, whose position and thickness are listed in Table 6.3. Pair production, bremsstrahlung and multiple scattering of charged particles were simulated; (a description of the simulation is given in Appendix A). The production point of each secondary particle was calculated at the radius of the material layer in which it was produced. Tracks were projected back to their closest point of approach to the interaction point, where the track parameters Z_0, d_0 and ϕ_0 were defined.

The trigger logic for the CPC, DC and ITOF counters, described in chapter 3, was simulated next.

The efficiencies of the CPC and ITOF counters were calculated using a sample of Bhabha events selected by the cuts described in chapter 7, which were designed to find events from the reaction $e^+e^- \rightarrow \gamma\gamma$. These cuts selected events with the shower counter total energy trigger set and collinear energy deposits in the calorimeters. The efficiencies, which are listed in Table 6.4 were calculated from the number of events where there was no CPC or no ITOF information associated with a final state particle.

The efficiency of the DC prepro is momentum dependent and is listed in Table 6.5 [82]. The efficiency for momentum > 2 GeV/c was calculated from the data sample used to calculate the CPC and ITOF efficiencies and

is given in Table 6.5. Tracks without CPC or ITOF information were not accepted by the DC prepro.

The topology trigger was then simulated using the tracks identified by the DC prepro and events without the topology trigger set were rejected.

In the next stage of the program the momentum vector of each track was redefined to account for the resolution of the drift chamber. Hits were assigned to each track in each of the detector planes. The drift chamber 0° layer hits were fitted to a circle to determine the track parameters R_0, ϕ_0, d_0 and the α layer hits were fitted to a straight line for the track parameters z_0 and tan λ.

Each drift chamber plane was simulated by calculating the cell through which the track passed. The position of the hit was defined by the phi value of the track at the cell smeared with a gaussian distribution with mean = 0 and σ = 0.035/r radians, where r is the radius of the layer. A software efficiency of 98% and a hardware efficiency of 98% for each hit was used.

The drift chamber cannot detect more than one track passing through a cell. If more than one track passed through a cell then the hit was assigned to the track closest to the sense wire.

Tracks were outside the acceptance of the drift chamber if they passed through fewer than 5 0° layers or 3 α layers and were rejected as having insufficient hits to be reconstructed if they had fewer than 4 0° layer hits or 3 α layer hits.

The software programs described in chapter 3 were now simulated. The major part of this software is the 'FOREST' program which reconstructs the charged tracks in an event using the drift chamber information. The efficiency of the FOREST program for reconstructing a track has been measured using 2-prong data[82]. Two efficiencies were used for the r-ϕ fit and one for the z fit. These efficiencies are given in Table 6.6

as a function of momentum and in Table 6.7 as a function of the number of layers crossed. The second r-ϕ efficiency corresponds to the second and third passes through the data that FOREST makes if it finds more than one track in its first pass through the data.

The PASS 2 and BHASEL programs were then applied to the tracks reconstructed by FOREST.

Surviving events were passed through the MILL program. The efficiences of this program for the r-ϕ and z reconstruction of tracks have been measured from data[81] as a function of the number of layers traversed and are shown in Table 6.8. The track parameters after MILL were then stored in banks in the same way as data.

The final analysis of events was made using the cuts of section 6.2.

The systematic error in the acceptance was calculated by varying the efficiencies used in the program within assumed errors and was found to be ± 5%.

The Monte-Carlo program gave a good description of the z_0,d_0 and t_{meas} distributions, the momentum spectrum of tracks and the number of events with more than 2 charged tracks. The number of events with charge mis assignment was underestimated and a scaling factor of .97 (calculated from the number of Bhabha events with $\Sigma Q \neq 0$), was used to correct for this.

6.5 Data analysis

In this section the differential cross-section, cross-section and the QED cut off parameters are calculated.

6.5.1 Total cross-section

The total cross-section was determined by comparing the number of events predicted by the Monte Carlo program with the number of events in the Bhaba data sample. The predicted number was corrected by the muon and tau pair backgrounds and was normalised to the measured luminosity.

The data were taken in the 'scan' mode where approximately $30nb^{-1}$ luminosity was collected at each energy point with an interval of 10 MeV between points. The data were grouped together in bins of width 0.5 GeV and the W value of each bin was taken as the average of the bin. For the combined high energy data at an average W = 34.8 GeV, $\sigma_{meas}/\sigma_{QED}$ = 1.01 ± .02 for a luminosity of 5400 nb^{-1} and for the data at W = 12 GeV $\sigma_{meas}/\sigma_{QED}$ = 0.97 ± 0.4 for a luminosity of $95nb^{-1}$.

The cross-section measurement is given in Table 6.9 along with the total luminosity, the measured number of events and the predicted number of events at each value of W.

6.5.2 Differential cross-section

The measured differential cross-section is shown in Fig 6.13 for the data at W = 12 GeV and the combined high energy data at an average W of 34.8 GeV. The solid curve represents the lowest order QED differential cross-section, equation 6.1.2. Each event was given a weight, where the weight W_j of bin j was determined from the previously described Monte Carlo program,

$$W_j = a_j^{-1} r_j^{-1} \qquad - 6.5.1$$

j refers to the bin in cosθ, r_j represents the radiative correction and a_j the acceptance of bin j. The data points were normalised to the measured total cross-section. Fig 6.14 shows the measured differential cross-section divided by the QED prediction as a function of cosθ.

6.5.3 Tests of QED

The measured differential cross-section at W = 34.8 GeV was compared with the differential cross-section predicted by the model describing modifications of QED. The cut-off parameters $\Lambda\pm$ were calculated by minimising the chi-square defined by:

$$\chi^2 = \sum_j \left(\frac{d\sigma}{d\Omega}_{oj} - \frac{d\sigma}{d\Omega}_j \right)^2 / \Delta^2 \frac{d\sigma}{d\Omega}_j \qquad - 6.5.2$$

where $d\sigma/d\Omega_j$ and $\Delta d\sigma/d\Omega_j$ are the measured differential cross-section and its error respectively and $d\sigma/d\Omega_{oj}$ is the QED prediction for bin j.

The data have been fitted using equation 6.1.7 and equation 6.1.8 to represent $d\sigma/d\Omega_{oj}$. Using 6.1.7 separate information on the spacelike and timelike form factors is obtained, as at backward scattering angles both amplitudes are comparable in size while at forward scattering angles the spacelike amplitude dominates.

Table 6.10 shows the results of a fit to the combined high energy data at W = 34.8 GeV. Fig 6.15 shows a plot of χ^2 vs $1/\Lambda^2$ obtained from the fit using equation 6.1.8, which is a parabola centred at $1/\Lambda_o^2$. The shift of the parabola minimum from the point $1/\Lambda^2 = 0$ comes from the error in the cross-section measurement, if QED is valid for all momentum transfers Q^2 a perfect measurement of the angular distribution would give $1/\Lambda^2 = 0$. The minimum value of the parameter $1/\Lambda^2$ and its error were used to calculate the cut off parameters $\Lambda\pm$. The cut off parameters calculated at 95% confidence are listed in Table 6.10. The shift of the minimum results in the asymmetric values of $\Lambda+,\Lambda-$.

Equation 6.1.9 has been used to determine a distance above which QED is valid, using the lowest cut off value for the case where $\Lambda = \Lambda_s = \Lambda_t$. At 95% confidence level $r \sim 1.3 \times 10^{-16}$ cm.

Table 6.10 shows the cut off parameters for muon and tau pair production, which were also measured[47,51] using the TASSO detector, with data from the run period analysed here.

6.5.4 Systematic error

The systematic error was estimated as (± 7%) and was obtained by adding the uncertainty in the acceptance (± 5%) and the luminosity (± 4%) in quadrature.

6.6 Conclusions

Bhabha scattering has been studied at centre of mass energies W between 12 and 36.6 GeV. For the high energy data, at W = 34.8 GeV the ratio of the measured cross-section to the QED prediction is 1.01 ± 0.02 and at W = 12 GeV is .97 ± .04. The measured differential cross-section $s d\sigma/d\Omega$ at W = 12 GeV and W = 34.8 GeV is consistent with the prediction of QED and is independent of s. Parameterising a breakdown of QED by a form factor the cut off parameters $\Lambda+$ = 150.9 GeV and Λ = 161.9 GeV are calculated, alternatively QED is valid down to a distance of $\sim 1.3 \times 10^{-16}$ cm.

Ebeam (GeV)	no of muon pair events	no of tau pair events
15·00	6·95	0·61
16·25	4·15	0·38
16·75	38·98	4·22
17·25	63·72	7·01
17·75	42·34	4·76
18·30	9·46	1·15
6·00	23·40	0·85

Table 6·1 number of muon and tau pair background events in each energy bin

	Mean Radius (cm)	Thickness (cm)	X/X_o
1) Beam pipe			
Al		0.4	0.045
Rohacell		0.6	0.003
Kapton		0.0025	0.001
PVC		0.45	0.010
Al cooling pipe			0.002
	13.4		0.061
2) Pipe counters			
Scintillator		0.5	0.0116
Al foil		0.0050	0.0005
Wrapping		0.01	0.0003
	15.1		0.012
3) Cylindrical Proportional Chamber			
Expanded Polystyrene		7.0	0.0030
Epoxy, 24 x 0.09		0.21	0.0063
Copper, 8 x 0.04/1.2		0.027	0.0186
Kapton, 8 x 0.075		0.060	0.0021
Mylar , 2 x 0.075		0.015	0.0005
Al foil		0.020	0.0022
Tungston Anode wires			0.00003
Gas (Argon + Isobutane)		5.6	0.00045
	23.3		0.033
4) Synchroton Radiation Shield*			
Al	32.0	0.20	0.022
Sn	32.0	0.06	0.050
			0.072
	32.0		
5) Drift chamber			
Fiberglass	32.5	0.49	0.024
Argon gas	79.5	90	0.008
			0.032
Total	26.1		0.210

* Installed Dec. 1979 after run 1571. This represents about 60 % of the solid angle. About 30 % of the solid angle has the 2.0 mm Al replaced with 0.125 mm mylar. The proportional chamber rail system is in the remaining 10 %. Typical there are about 1.5 cm Al in this region.

Table 6·2 thickness and radius of material inside the solenoid

layer number	thickness (cm)	mean radius (cm)
1	0·988	13·35
2	0·988	14·35
3	12·932	23·30
4	0·260	32·00
5	0·490	32·50
6	90·000	79·50

Table 6·3 parameterisation of the material inside the solenoid

counter	efficiency per track
CPC	0·987±·059
ITOF	0·964±·059

Table 6·4 CPC and ITOF efficiencies per track

momentum range (MeV/c)	efficiency per track (%)
0 — 138	0 · 00
138 — 161	2 · 96
161 — 184	10 · 84
184 — 267	28 · 58
207 — 230	46 · 32
230 — 253	60 · 12
253 — 276	68 · 99
276 — 299	78 · 85
299 — 322	83 · 78
322 — 345	86 · 73
345 — 368	89 · 69
368 — 391	90 · 68
391 — 414	91 · 66
414 — 437	92 · 65
437 — 460	93 · 63
460 — 483	94 · 62
483 — 506	95 · 60
>506	96 · 59

Table 6·5 efficiency of the DC prepro with track momentum

momentum range (MeV/c)	r-ϕ efficiency / track		z efficiency/trk (%)
	1st pass (%)	2nd&3rd passes (%)	
0 — 150	0·00	0·00	0·00
150 — 175	0·00	3·00	30·90
175 — 200	4·68	46·00	54·31
200 — 225	24·63	91·00	84·28
225 — 250	33·72	95·00	87·09
250 — 275	47·78	95·00	87·09
275 — 300	63·70	95·00	88·03
300 — 325	81·50	95·00	88·03
325 — 350	83·37	95·00	88·03
350 — 375	84·31	96·00	88·03
375 — 400	85·25	96·00	88·96
400 — 425	86·18	97·00	88·96
425 — 450	87·12	97·00	88·96
450 — 475	88·06	98·00	89·90
475 — 500	88·99	98·00	89·90
>500	89·93	99·00	89·90

Table 6·6 efficiency of FOREST with track momentum

layer number	r-Ø efficiency/track		z efficiency/trk (%)
	1st pass (%)	2nd&3rd passes	
1	0·0	0·0	0·0
2	0·0	0·0	0·0
3	0·0	0·0	0·0
4	0·0	68·0	13·0
5	9·0	97·0	50·0
6	79·0	98·0	77·0
7	93·0	98·0	84·0
8	93·0	98·0	94·0
9	100·0	100·0	100·0

Table 6·7 efficiency of FOREST with the number of DC 0° layers traversed

0 layer number	r-Ø efficiency /trk (%)	stereo layer number	z efficiency /trk (%)
1	0·0	1	0·0
2	0·0	2	0·0
3	0·0	3	80·0
4	0·0	4	90·0
5	80·0	5	100·0
6	90·0	6	100·0
7	100·0		
8	100·0		
9	100·0		

Table 6·8 efficiency of MILL with the number of DC layers traversed

W (GeV)	luminosity (nb^{-1})	no of events − background	predicted no of events	$\sigma_{meas}/\sigma_{QED}$
12·0	95·0	566 · 8	586 · 8	0·97 ±·04
30·0	174·0	152 · 4	118 · 4	1·29 ±·08
32·5	120·9	76 · 5	70 · 4	1·09 ±·11
33·5	1215·4	658 · 8	666 · 7	0·99 ±·04
34·5	2104·4	1005 · 3	1090 · 1	0·92 ±·03
35·5	1453·0	840 · 9	711 · 6	1·18 ±·04
36·6	351·8	121 · 4	162 · 3	0·75 ±·09

Table 6·9 summary of the cross-section results for Bhabha scattering

reaction	fitted parameter (GeV^{-2})	Λ_+ (GeV)	Λ_-
$e^+e^- \rightarrow e^+e^-$	$\frac{1}{\Lambda_s^2} = (-1{\cdot}24 \pm 2{\cdot}63) \times 10^{-5}$	135	181
	$\frac{1}{\Lambda_t^2} = (7{\cdot}71 \pm 9{\cdot}50) \times 10^{-5}$	113	66
	$\frac{1}{\Lambda^2} = (-0{\cdot}29 \pm 2{\cdot}52) \times 10^{-5}$	151	162
	$(\Lambda_s = \Lambda_t = \Lambda)$		
$e^+e^- \rightarrow \mu^+\mu^-$	$\frac{1}{\Lambda^2} = (-5{\cdot}0 \pm 4{\cdot}5) \times 10^{-5}$	206	90
$e^+e^- \rightarrow \tau^+\tau^-$	$\frac{1}{\Lambda^2} = (-1{\cdot}8 \pm 11{\cdot}15) \times 10^{-5}$	88	103

Table 6·10 cut-off parameters measured by TASSO

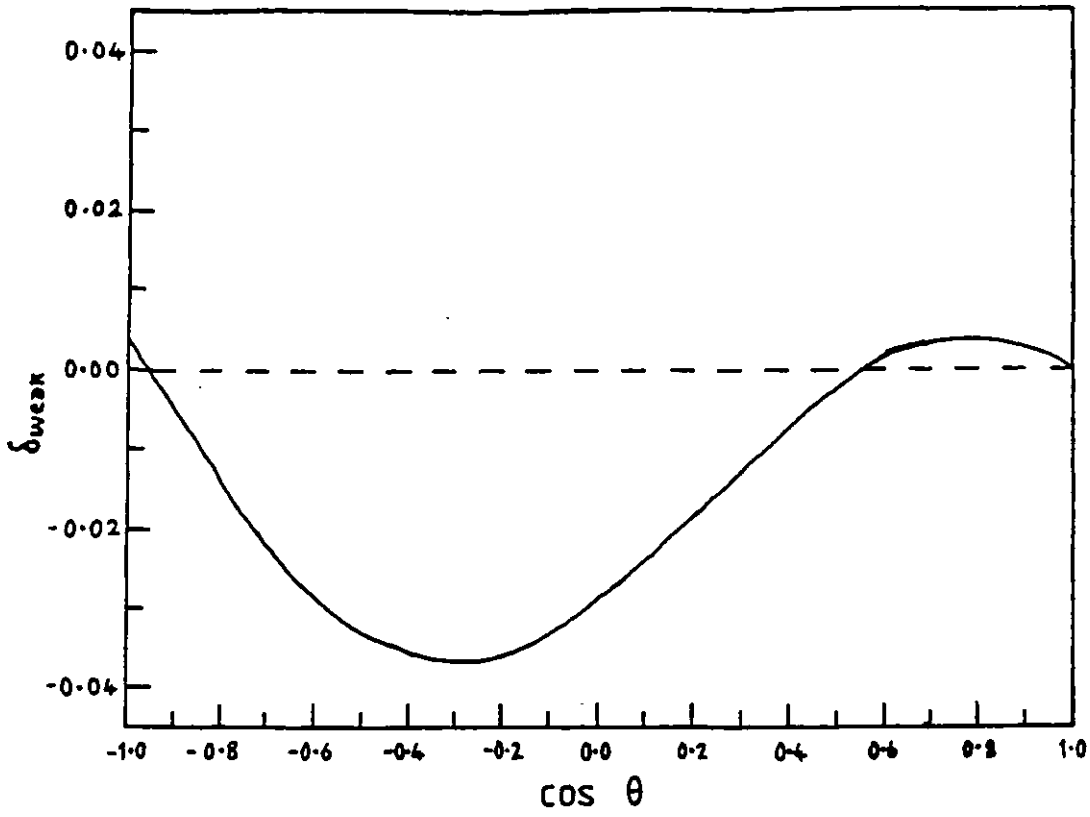


Fig 6·1 deviation of the Bhabha angular distribution from the QED prediction due to weak interaction effects v. cosθ at W = 35 GeV for $\sin^2\theta_W = 0.25$

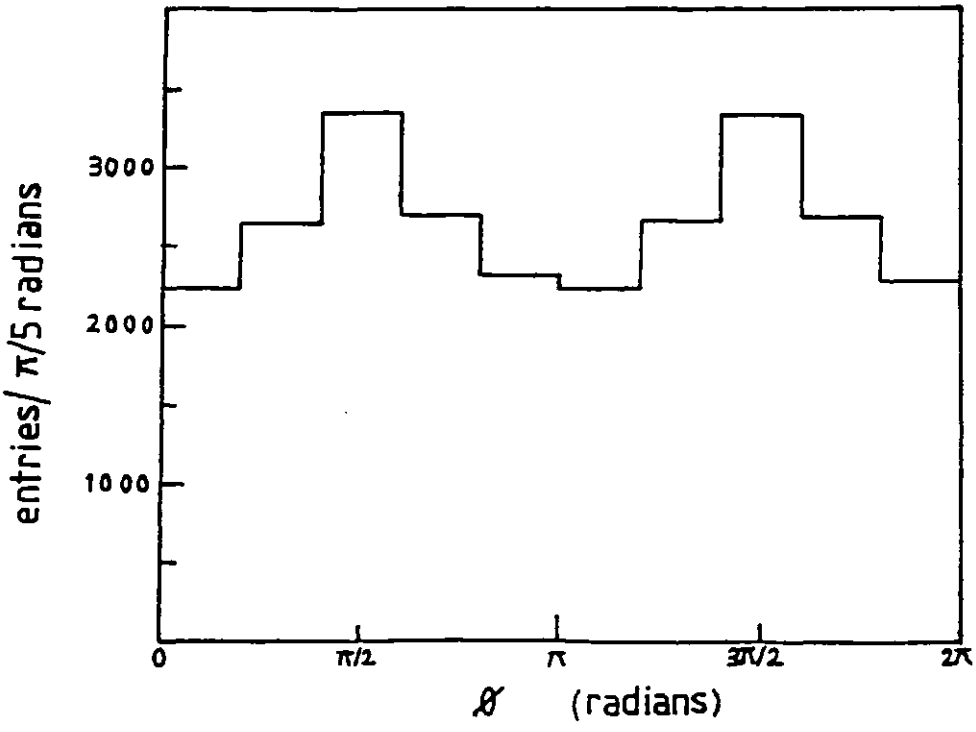


Fig 6·2 φ distribution before Bhabha selection cuts

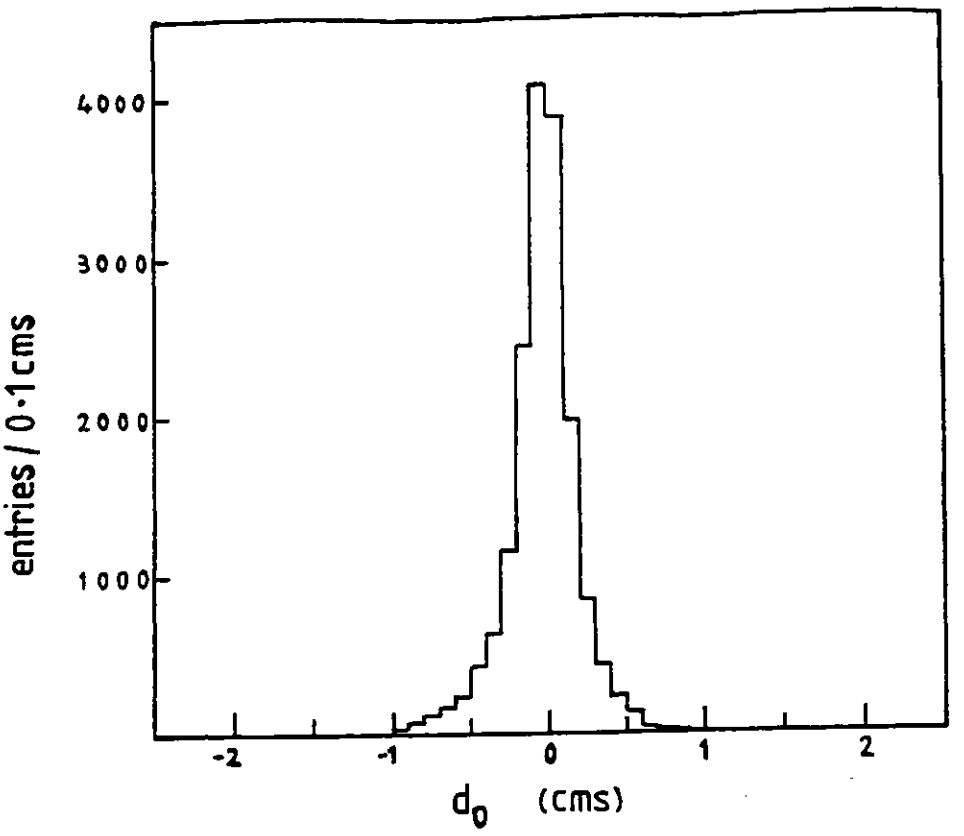


Fig 6·3 d_0 distribution after fiducial cuts

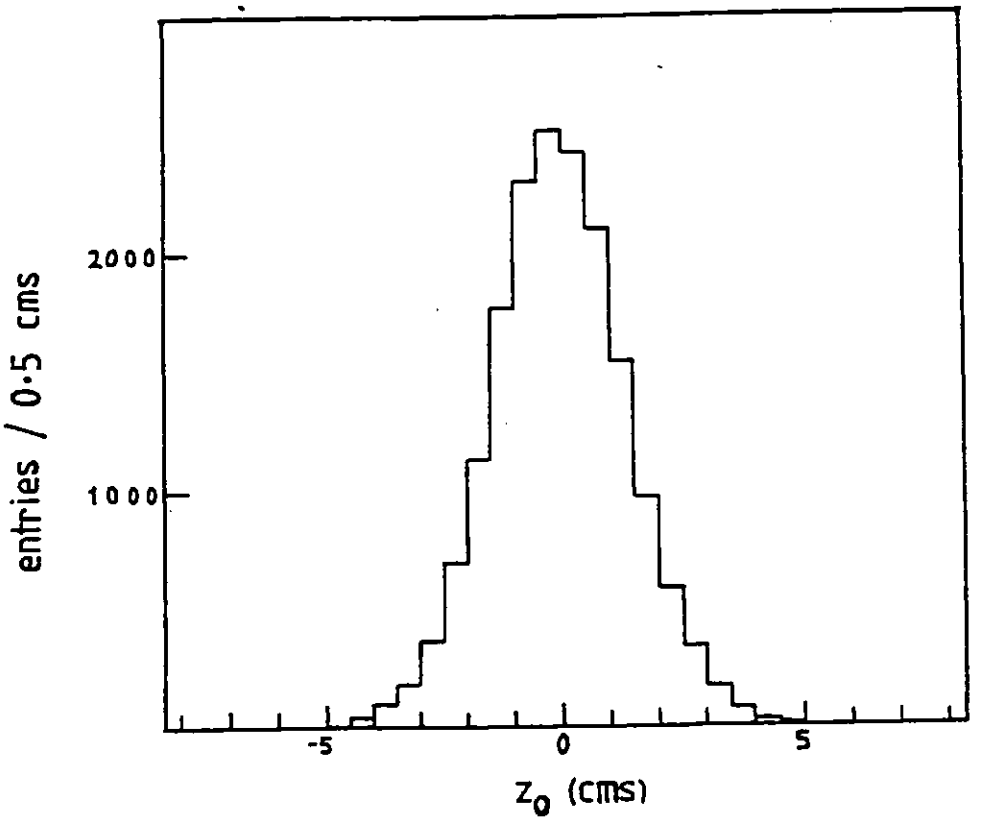


Fig 6·4 Z_0 distribution after fiducial cuts

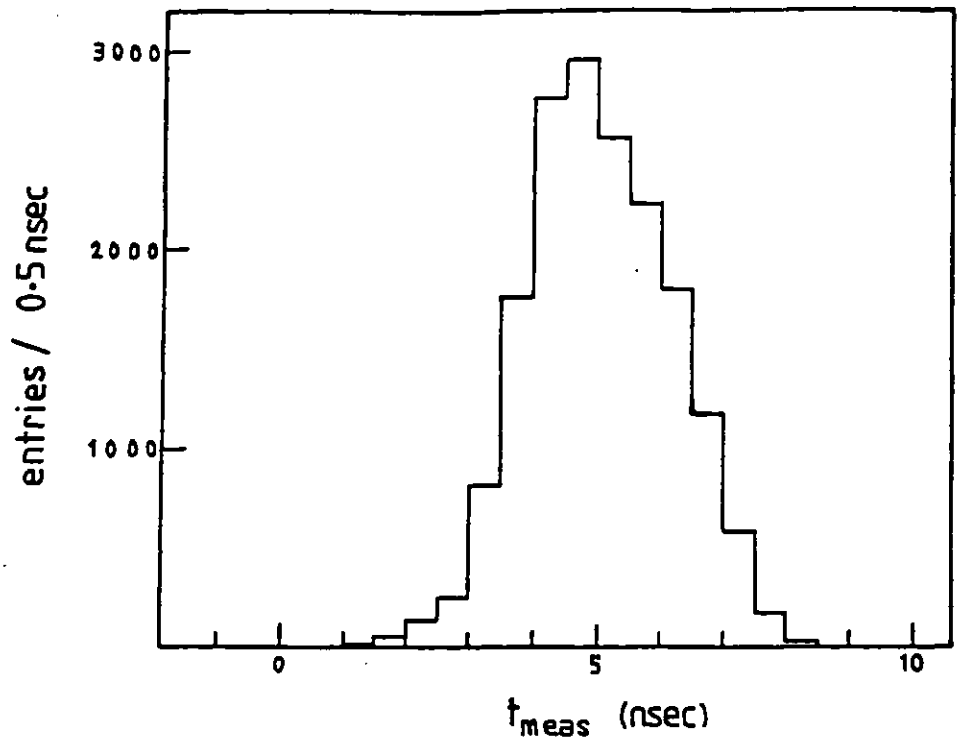


Fig 6·5 t_{meas} distribution after fiducial cuts

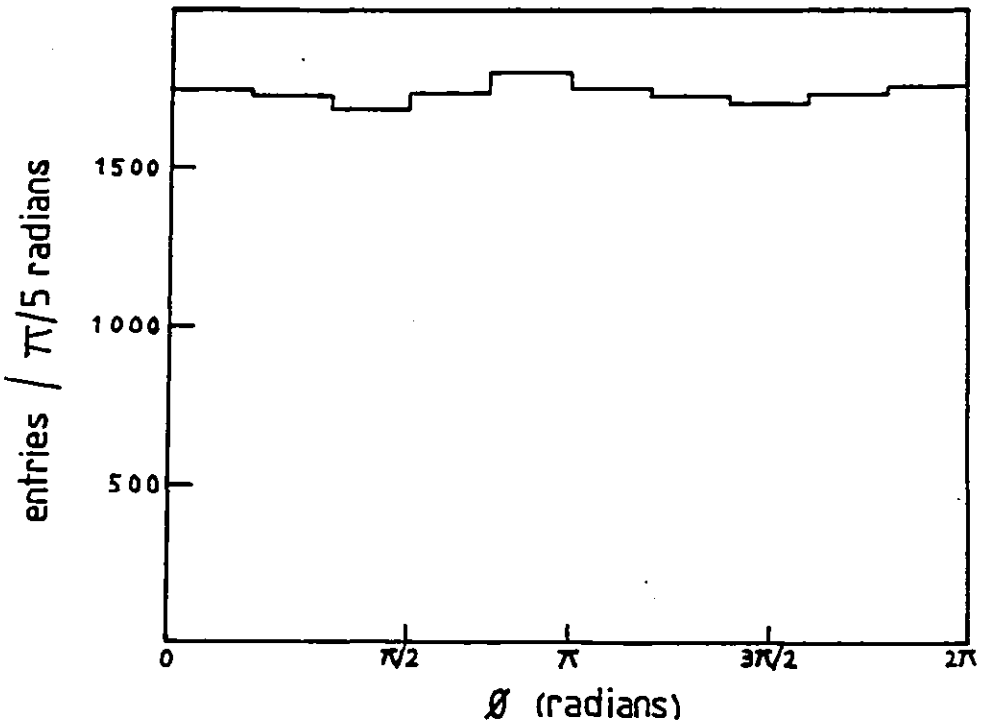


Fig 6·6 ϕ distribution after fiducial cuts

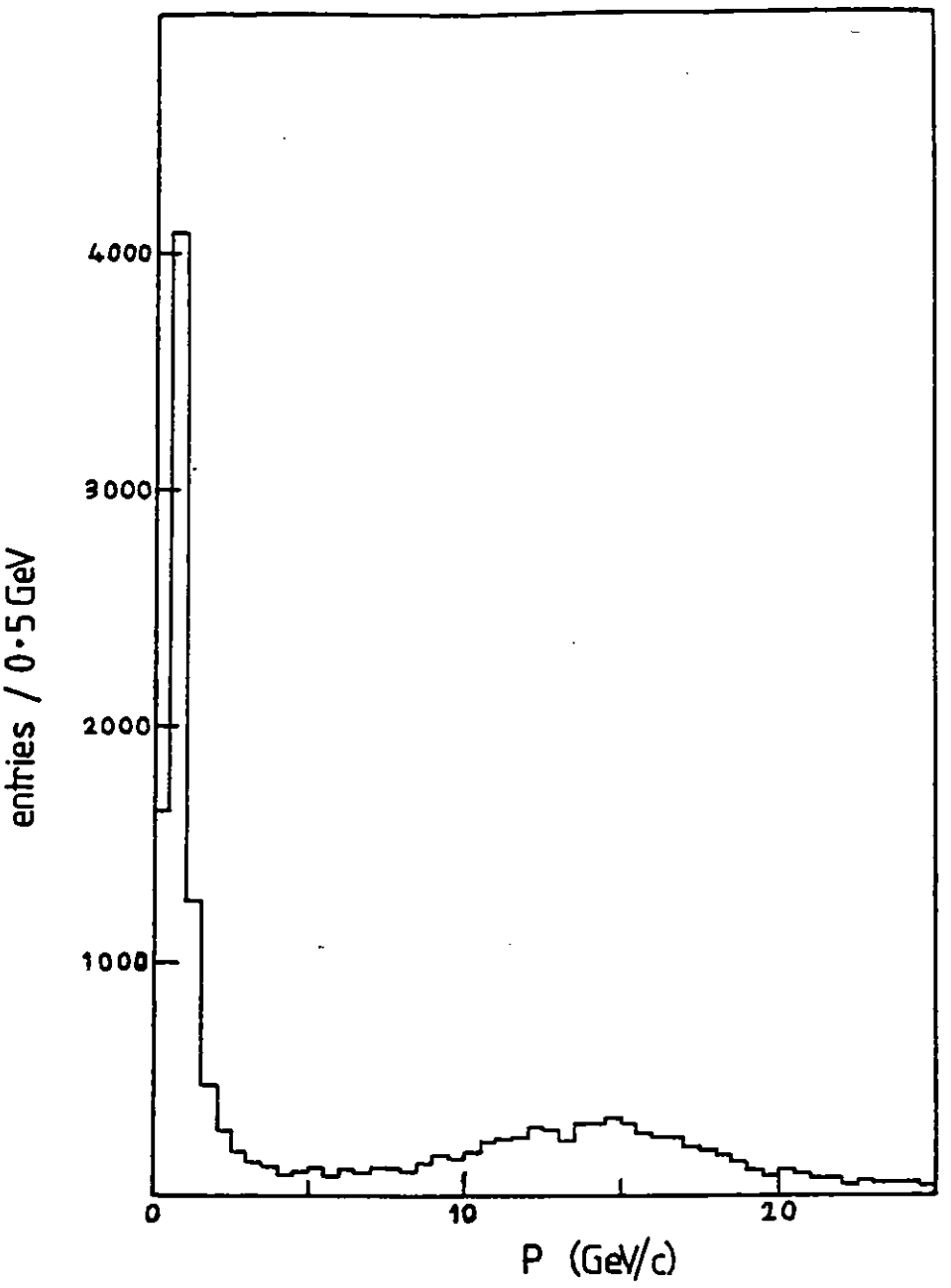


Fig 6·7 momentum spectrum of tracks

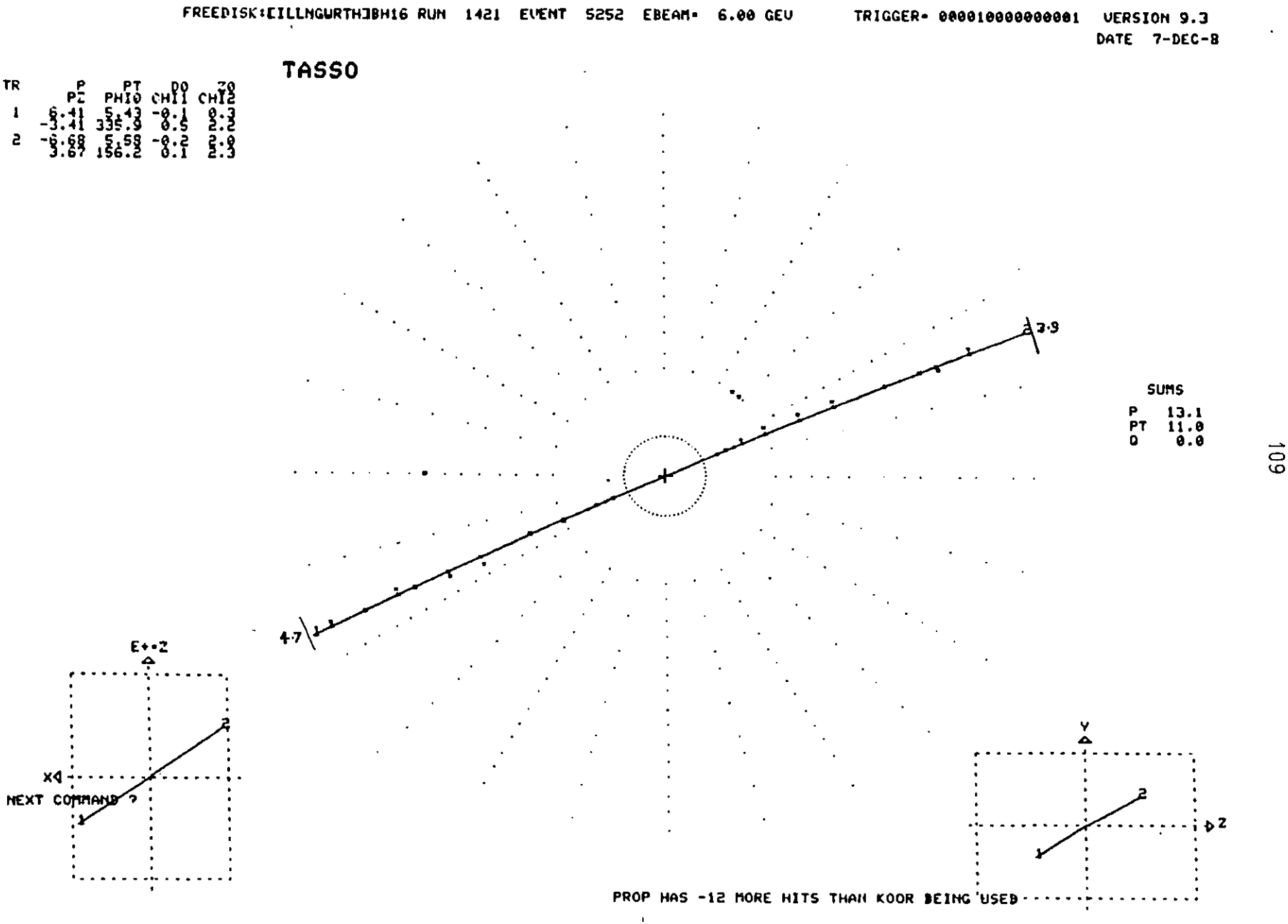


Fig 6.8 Bhabha event at W = 12 GeV

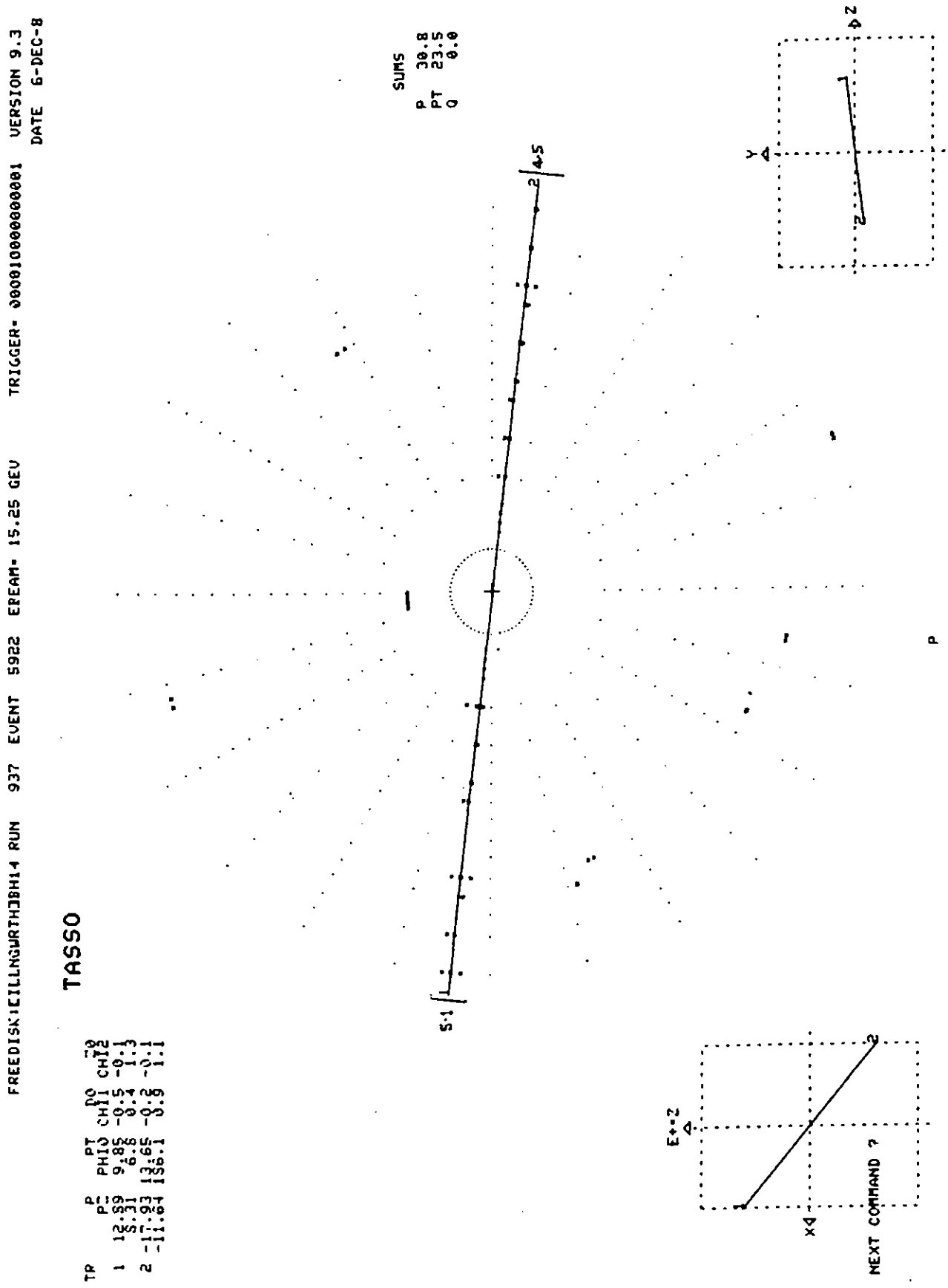


Fig 6.9 Bhabha event at W = 30.5 GeV

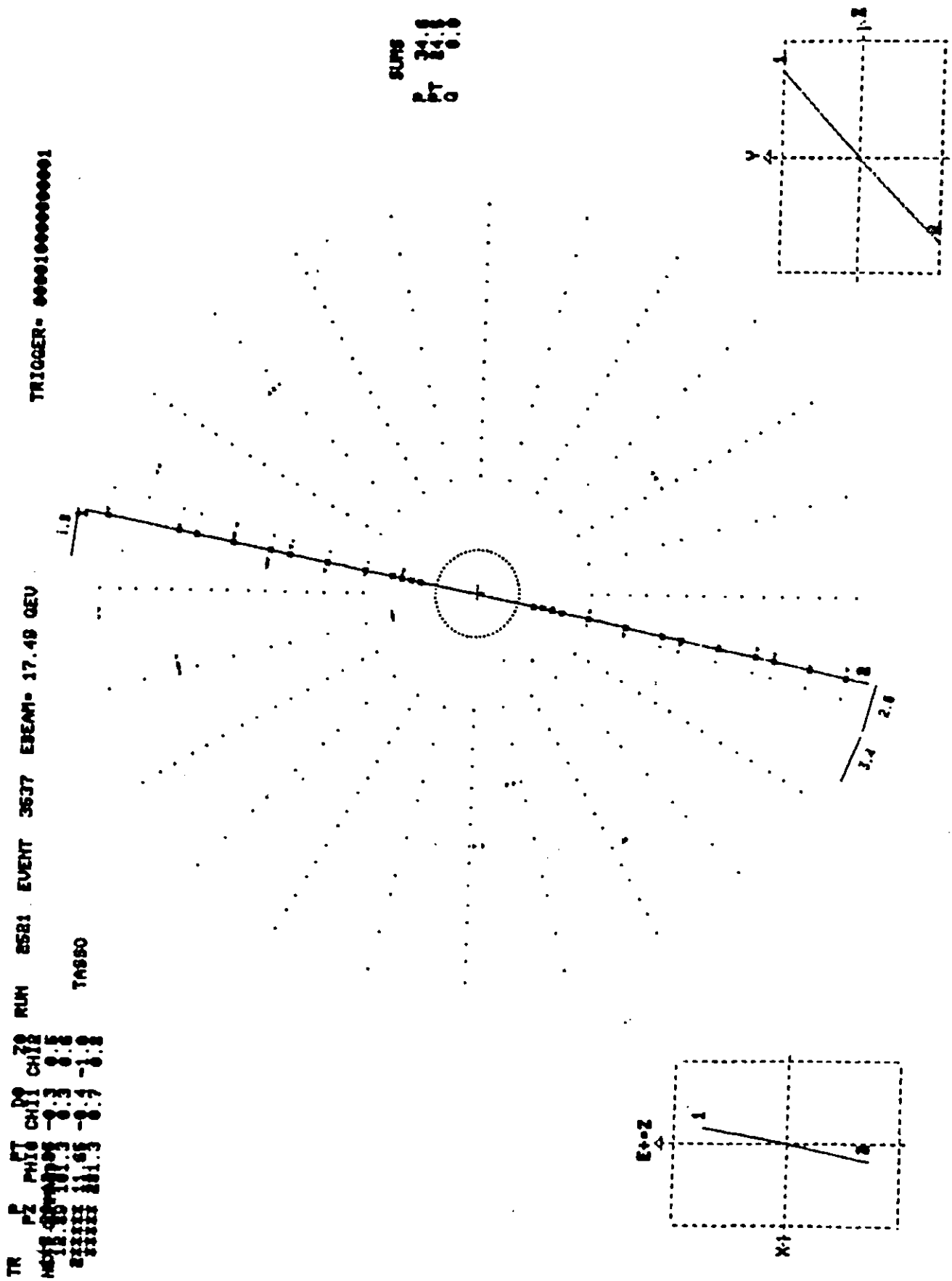


Fig 6.10 Bhabha event at W = 35 GeV

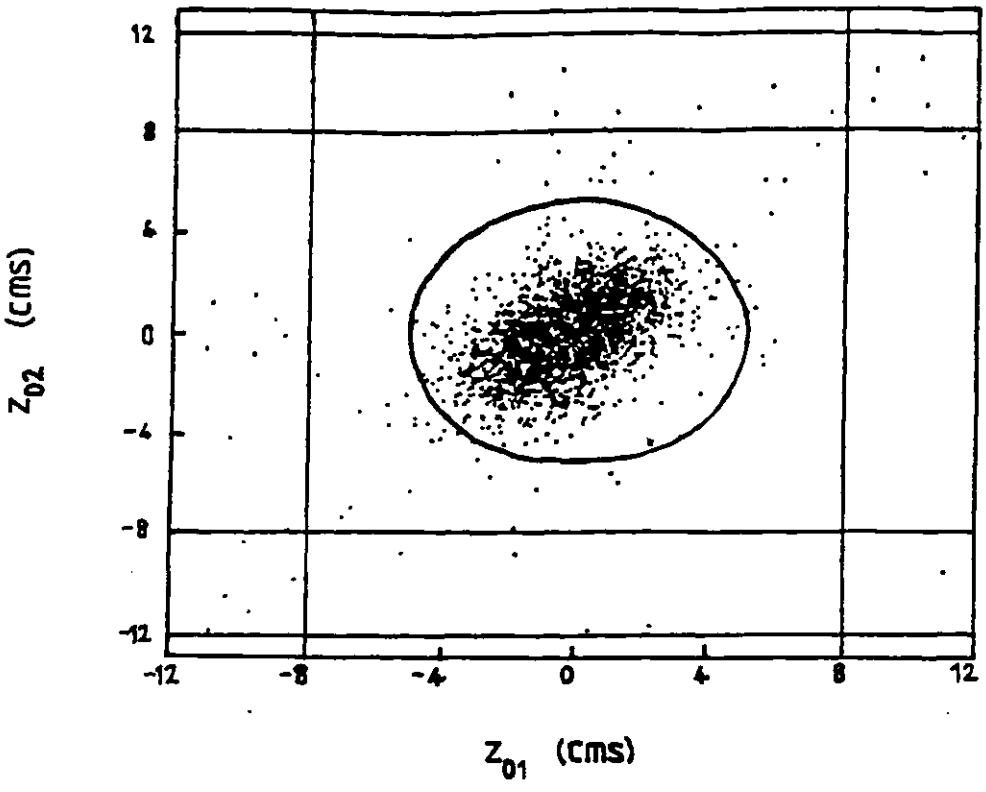


Fig 6·11 Z_{01} V. Z_{02} after Bhabha selection cuts (excluding the Z_o cut). The boundaries $|Z_o| > 8$ cm and $(Z_{01}^2 + Z_{02}^2)^{\frac{1}{2}} \leq 5$ cm used to calculate residual cosmic ray background are indicated

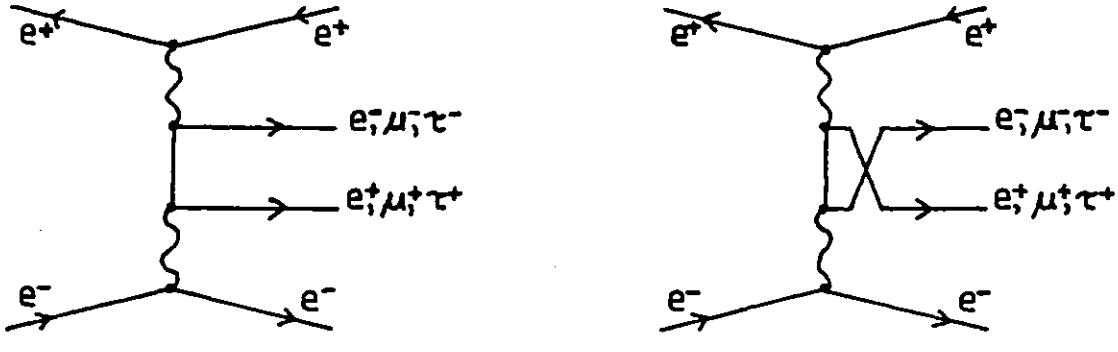


Fig 6·12 diagrams used to calculate the background from gamma-gamma scattering to leptons

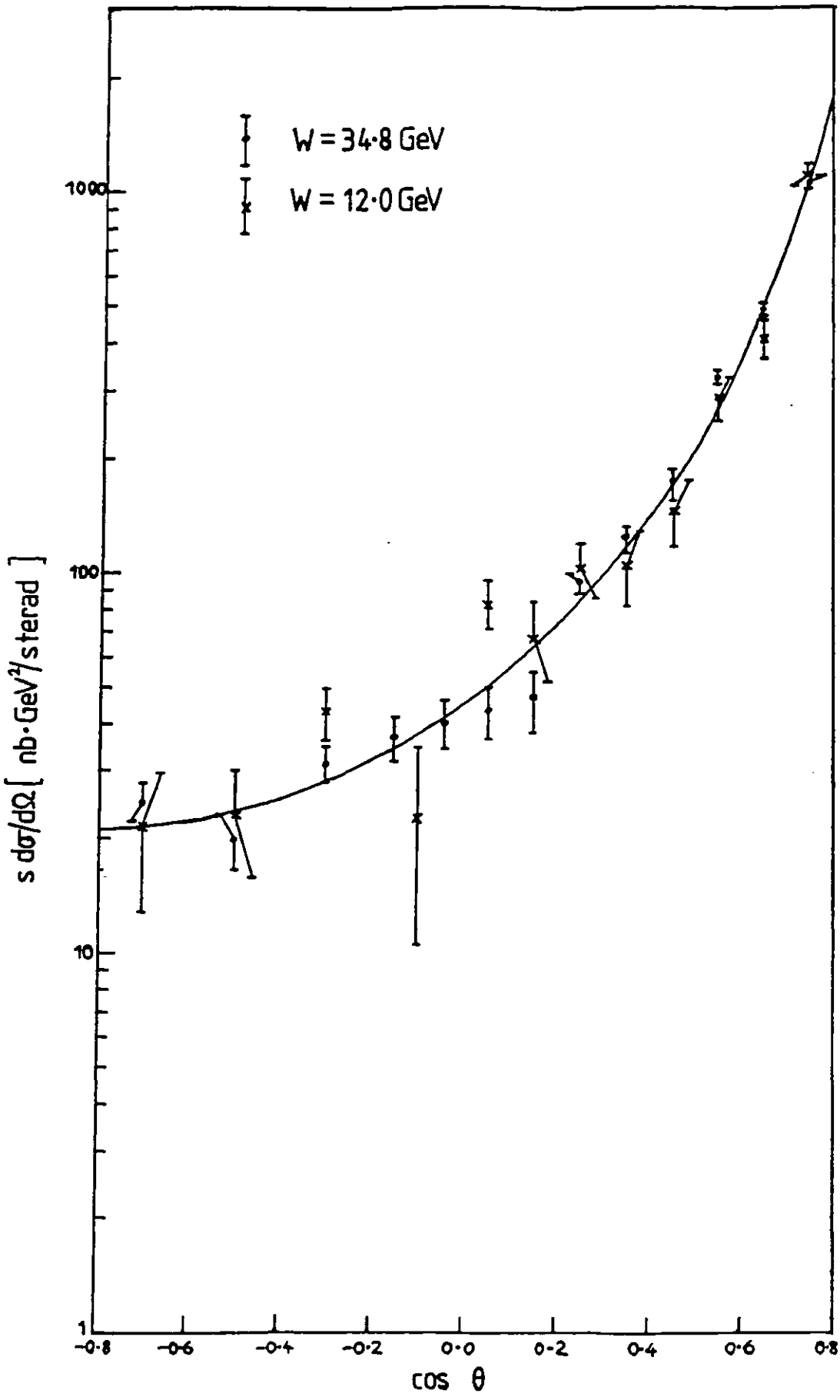


Fig 6·13 $s d\sigma/d\Omega$ v. $\cos\theta$ for W = 12 GeV and W = 34.8 GeV (the solid curve is the prediction of QED)

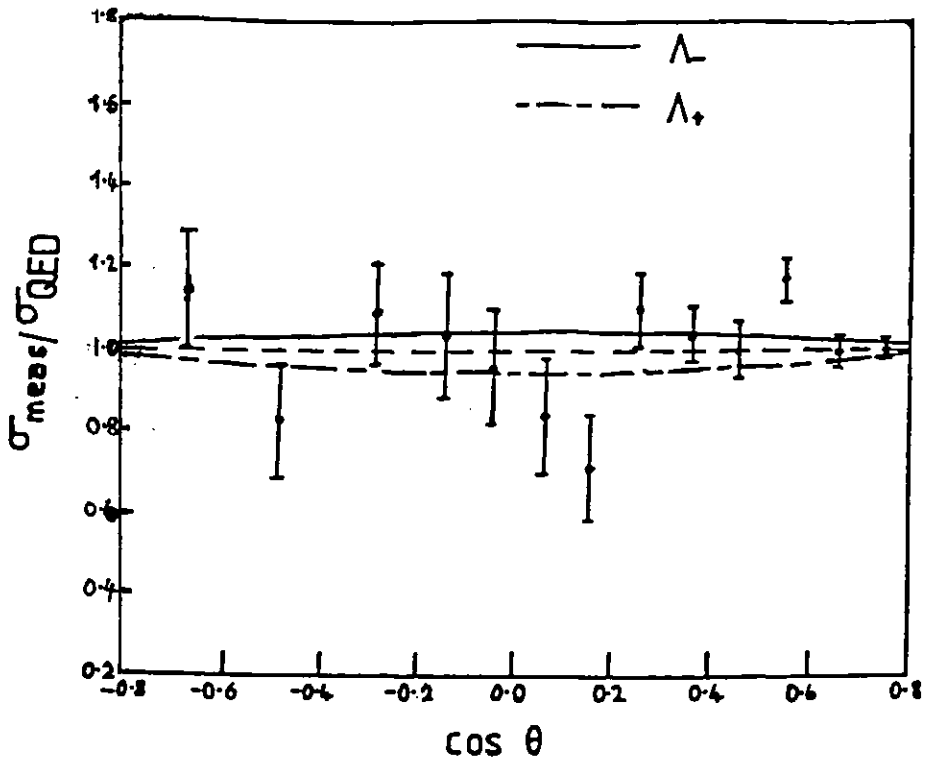


Fig 6·14 $(d\sigma/d\Omega_{meas})/(d\sigma/d\Omega_{QED})$ v. cosθ, the curves represent the modifications to QED at 95% confidence (W=34·8 GeV)

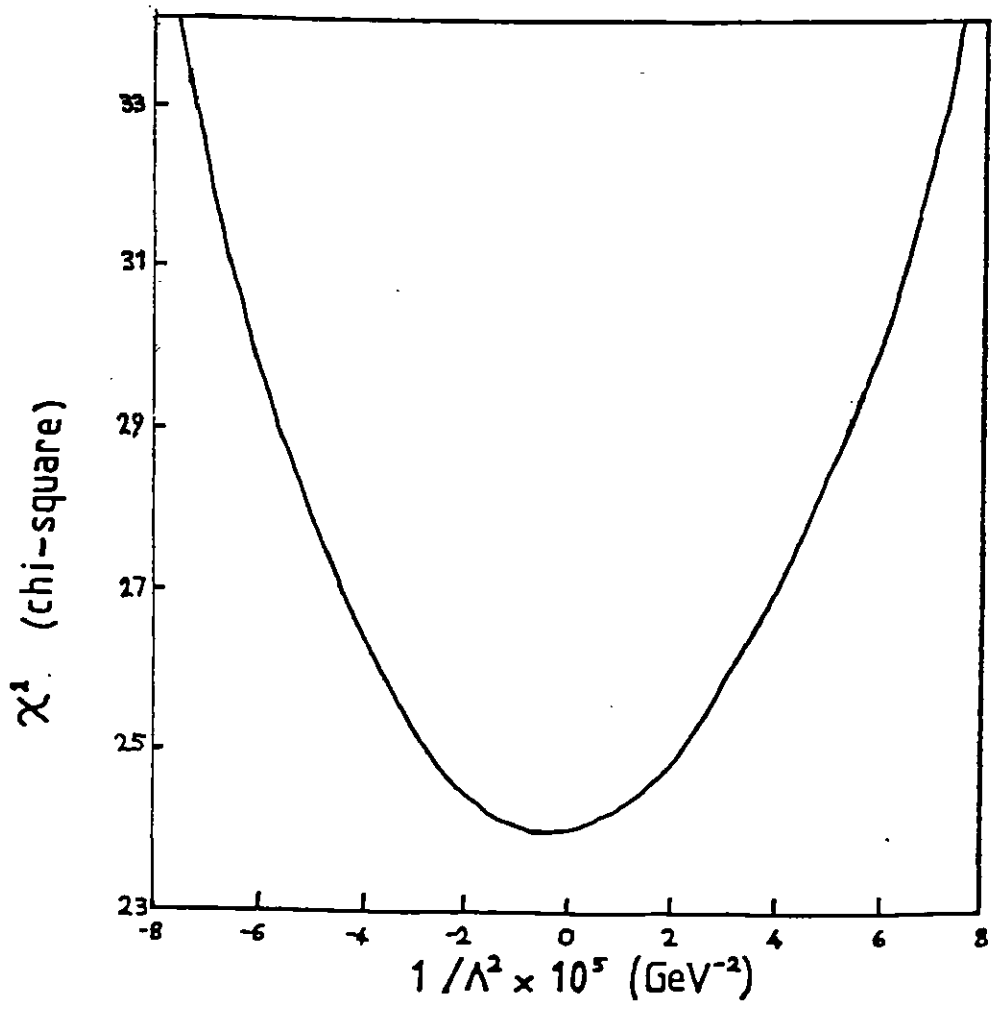


Fig 6·15 χ^2 v. $1/\Lambda^2$

CHAPTER 7

ANNIHILATION OF $e^+ e^-$ PAIRS INTO GAMMA RAYS

7.1 Introduction

In this chapter an analysis of the reaction $e^+e^- \rightarrow \gamma\gamma$ is presented. A theoretical description of the reaction is given and the data selection procedure is described. Two classes of events are considered, a) those in which a photon has converted and b) those in which there has been no conversions in the material preceding the drift chamber. The backgrounds to each class of event are calculated and the monte-carlo programs used to calculate the corresponding acceptances are described.

The cross-section was evaluated for centre of mass energies, W, between 12 and 36.6 GeV. Tests of QED were made at an average W of 34.8 GeV for the events of class b). Two models describing modifications of QED were used, testing the theory to high values of the momentum transfer $Q^2 \sim 1300\ GeV^2$.

7.1.1 QED cross-section for $e^+e^- \rightarrow \gamma\gamma$

The lowest order differential cross-section, calculated from the two graphs shown in Fig 1.11 is[33]:

$$\frac{d\sigma_o}{d\Omega} = \frac{\alpha^2}{2s}\left[\frac{q'^2}{q^2} + \frac{q^2}{q'^2}\right] \qquad 7.1.1$$

where $q^2 = -s\sin^2(\theta/2)$, $q'^2 = -s\cos^2(\theta/2)$, s is the centre of mass energy squared and the mass of the electron has been neglected.

Substituting for q^2 and q'^2, equation 7.1.1 can be rewritten as:

$$\frac{d\sigma_o}{d\Omega} = \frac{\alpha^2}{s}\left[\frac{1 + \cos^2\theta}{\sin^2\theta}\right] \qquad 7.1.2$$

If the electron and positron were polarised with a transverse polarisation P the lowest order differential cross-section would be:

$$\frac{d\sigma_o}{d\Omega} = \frac{\alpha^2}{s}\left[\left\{\frac{1 + \cos^2\theta}{\sin^2\theta}\right\} + P^2\cos 2\phi\right] \qquad 7.1.3$$

As no beam polarisation has been seen at PETRA during data taking periods equation 7.1.2 has been used.

The lowest order differential cross-section, equation 7.1.2, is shown in Fig 7.1, it is symmetrical about $\theta = \pi/2$ and is divergent at $\theta = 0$ and $\theta = \pi$.

7.1.2 Radiative corrections

Contributions from higher order graphs modify the lowest order cross-section. These graphs produce the final state ($e^+e^- \rightarrow \gamma\gamma\gamma$) which in terms of geometrical characteristics is indistinguishable from the lowest order final state ($e^+e^- \rightarrow \gamma\gamma$), when one of the photons is of low energy or is not detected. The radiative corrections are calculated by the method of Berends and Kleiss[83] using the graphs shown in Fig 1.12. The cross-section for pair annihilation into gamma rays is written as:

$$\frac{d\sigma}{d\Omega} = \frac{d\sigma_o}{d\Omega} \{ 1 + \delta(\theta,\phi) \} \qquad 7.1.4$$

where $d\sigma_o/d\Omega$ is the lowest order (α^2) cross-section and $\delta(\theta,\phi)$ is the radiative correction to order (α^3).

The first 6 graphs in Fig 1.12 account for the contributions from Bremsstrahlung and the next 4 graphs represent virtual radiative corrections which contribute to order (α^3) via interference with the lowest order diagrams shown in Fig 1.11. As the final state consists of two indistinguishable photons for the virtual radiative correction graphs a further 4 graphs with the photon four-momenta q_1 and q_2 interchanged are required. Unlike the order (α^3) radiative corrections for Bhabha scattering, muon and tau pair production, there is no contribution from the strong interaction through hadron vacuum polarisation.

The initial state radiation corrections lead to an acollinearity between the final state photons and the value of the radiative correction is characterised by a threshold energy E_{th} on the final state photons and a limit on ξ the acollinearity angle between them. Fig 7.2 shows the

radiative correction, which is also symmetrical about $\theta = \pi/2$.

7.1.3 Tests of QED

In the reaction $e^+e^- \to \gamma\gamma$ there is no contribution from the weak interaction[44], or hadron vacuum polarisation.

Using the measured differential cross-section for this process it is possible to test for the existence of heavy objects which couple to the electron or photon.

a) Heavy electron exchange

A natural theoretical description of a breakdown in QED is through a coupling to a new particle, where an experimental confirmation of QED corresponds to an upper limit on the mass to coupling constant ratio.

Low[84] introduces three QED breakdown mechanisms, where the only breakdown mechanism appropriate to the reaction $e^+e^- \to \gamma\gamma$ is the coupling of an excited electron to the photon and electron. The coupling of the electron, excited electron and photon is via a magnetic interaction, (the usual γ_μ coupling is excluded by current conservation) of the form[84,43]:

$$H_I = \frac{e\lambda}{2M_{e^*}} \psi_{e^*} \sigma_{\mu\nu} \psi_e F^{\mu\nu} + \text{h.c.} \qquad 7.1.5$$

where M_{e^*} is the mass of the excited electron, λ is a measure of the strength of the interaction and $F^{\mu\nu}$ is the electromagnetic field tensor. This interaction is gauge invariant but is not renormalisable. The two additional graphs that are introduced in lowest order are shown in Fig 7.3.

Litke[43] has calculated the differential cross-section in lowest order including the extra graphs which has the following form:

$$\frac{d\sigma}{d\Omega} = \frac{d\sigma}{d\Omega}QED + \alpha^2 \left\{ \frac{1}{2} \left(\frac{\lambda}{M_{e^*}}\right)^4 (E^2\sin^2\theta + M^2_{e^*}) \left[\frac{q^4}{(q^2-M^2_{e^*})^2} + \frac{q'^4}{(q'^2-M^2_{e^*})^2} \right] \right.$$

$$\left. + \left(\frac{\lambda}{M_{e^*}}\right)^4 \frac{4M^2_{e^*}E^4\sin^2\theta}{(q^2-M^2_{e^*})(q'^2-M^2_{e^*})} + \left(\frac{\lambda}{M_{e^*}}\right)^2 \left[\frac{q^2}{(q^2-M_{e^*}{}^2)} + \frac{q'^2}{(q'^2-M_{e^*}{}^2)} \right] \right.$$

$$+ \left(\frac{\lambda}{M_{e^*}}\right)^2 E^2 \sin^2\theta \left[\frac{1}{(q^2-M_{e^*}^2)} + \frac{1}{(q'^2-M_{e^*}^2)}\right]\} \qquad 7.1.6$$

where $q^2 = -s/2(1-\cos\theta)$, $q'^2 = -s/2(1+\cos\theta)$ and $4E^2 = s$.
Neglecting terms of order $(\lambda/M_{e^*})^4$, in the limit $s \ll M_{e^*}^2$ equation 7.1.6 becomes:

$$\frac{d\sigma}{d\Omega} = \frac{d\sigma}{d\Omega}QED \left\{ 1 + \frac{s^2}{2\Lambda^4} \sin^2\theta \right\} \qquad 7.1.7$$

where $\Lambda^2 = M_{e^*}^2/\lambda$ 7.1.7b

The deviation is a function of s^2 and is maximum at $\theta = \pi/2$. If the coupling is the same as for unmodified QED ($\lambda = 1$) then $\Lambda = M_{e^*}$ is the mass of the heavy electron.

b) "Seagull" graph

A simple modification of QED for the reaction $e^+e^- \rightarrow \gamma\gamma$ would be a modification of the charged particle propagator. This requires a modification of the vertex function[85] in order to maintain current conservation. The Ward Takahashi identity[86]:

$$i(p_\mu - q_\mu)\, \Gamma_\mu(p,q) = s^{-1}(p) - s^{-1}(q) \qquad 7.1.8$$

determines the form of the vertex function modification, where $s(q)$ is the charged particle propagator, $p = i\gamma_\mu p_\mu$, $\Gamma_\mu(p,q)$ is the one photon vertex function and p,q and K are the four momenta of the real lepton, virtual lepton and real photon respectively. If one of the fermions is on the mass shell the vertex modification cancels completely with the propagator modification[85,87,42]. To make the modified amplitude gauge invariant it is also necessary to add a two photon vertex. Kroll[42] has developed a procedure for constructing the multi photon vertices required to make the modified amplitude gauge invariant. Following this procedure he shows that for any process of a given order in e, excluding closed loops, the amplitude is independent of the propagator modification.

Kroll then describes a general procedure for characterising a modified QED in terms of a modified propagator and a vertex modification.

Using the following vertex function

$$\Gamma_\mu = \gamma_\mu \pm \frac{1}{\Lambda^2}[\sigma_{\mu\nu}k_\nu(i\not{q} + m) + (i\not{p} + m)\sigma_{\mu\nu}k_\nu] \qquad 7.1.9$$

it can be shown[42] that all corrections of order (q^2/Λ^2) cancel and that the modification can be parameterised by a form factor

$$F(q^2) = 1 \pm \frac{q^4}{\Lambda_\pm^4} \qquad 7.1.10$$

With this modification what is being tested for is the presence of contributions from the two photon, "seagull" graph shown in Fig 7.4.

The differential cross-section given by equation 7.1.1 becomes:

$$\frac{d\sigma}{d\Omega} = \frac{\alpha^2}{2s}\left\{\frac{q'^2}{q^2}|F(q^2)|^2 + \frac{q^2}{q'^2}|F(q'^2)|^2\right\} \qquad 7.1.11$$

where $q'^2 = -s/2\,(1 + \cos\theta)$ and $q^2 = -s/2\,(1 - \cos\theta)$.

Substituting the form factors described by equation 7.1.10 into equation 7.1.11 the differential cross-section becomes:

$$\frac{d\sigma}{d\Omega} = \frac{d\sigma}{d\Omega}_{QED}\left\{1 \pm \frac{s^2}{2\Lambda_\pm^4}\,\frac{\sin^4\theta}{1+\cos^2\theta}\right\} \qquad 7.1.12$$

The deviation is a function of s^2 and is maximum at $\theta = \pi/2$. At $\theta = \pi/2$ the deviation is of the same magnitude as the deviation derived from an excited electron propagator. Fig 7.5 shows both of these modifications as a function of $\cos\theta$ for $S/\Lambda^2 = 1$.

7.2 Data selection

Events of the reaction $e^+e^- \to \gamma\gamma$ were selected from PASS1 tapes until October 1979. From this time events with the total energy trigger set and with more than 2 GeV energy deposited in the shower counters were selected by the PASS2 job and data selection was performed on the PASS2 tapes.

In the lowest order the final state consists of two collinear photons each with the beam energy. Higher order corrections, in particular initial state radiation, lead to an accolinearity angle distribution and an energy distribution of the final state photons. These distributions are shown in Fig 7.6 and Fig 7.7 respectively for events generated using the method of Berends and Kleiss[83]. Most events have a small accolinearity angle and the energy of the final state photons is close to the beam energy (86% have E > 90% Ebeam).

The shower counters were divided into four groups and the total energy deposited in each group was calculated. The groups were:

a) the north arm shower counters

b) the south arm shower counters

c) the shower counters above the coil

d) the shower counters below the coil

Data were taken during 1980 with the shower counter modules above the coil replaced by the upper part of the LABC. For this period group c) refers to the LABC, the total energy deposited in it was taken as the summed energy of all found clusters. Energy deposits were required in opposite groups and events with energy deposits in non opposite groups were rejected by the following cuts.

Events were selected where none of the photons had converted before the DC (class A). During 1980 data was taken with a synchrotron radiation shield, consisting of 2.6 mm of tin sandwiched between aluminium, installed between the CPC and DC to reduce the flux of synchrotron radiation entering the DC. This increased the amount of material before the DC from 13.8% to 21% of a radiation length and hence the number of photons converting before it. A second set of events, where a photon had converted before the DC, was selected for this data period (class B).

7.2.1 Selection of class A events

1) The total energy trigger was set, alone or with the pretrigger

2) In each opposite group there was greater than 2 GeV energy and less than 2 GeV energy in the non opposite groups:

$E_a > 2$ GeV.AND.$E_b > 2$ GeV.AND.$E_c \leq 2$ GeV.AND.$E_d \leq 2$ GeV.OR.

$E_a \leq 2$ GeV.AND.$E_b \leq 2$ GeV.AND.$E_c > 2$ GeV.AND.$E_d > 2$ GeV

A total energy cut and a cut on the number of shower counter modules, N, containing energy were applied to reduce the background.

3) $E_{TOT} \geq 8$ GeV (E beam > 14 GeV)

4) $N < 10$

The total energy is taken as the summed energy in the opposite groups defined by cut 2) and for the liquid argon data N is defined as the number of shower counter modules containing energy and the number of liquid argon clusters.

The cluster finding program described in chapter 5 was run on the events that survived these cuts.

5) The acollinearity angle, ξ, calculated using the maximum energy cluster in the opposite counter groups defined by cut 2), was required to be $< 10°$. This removes background events, as events from $e^+e^- \rightarrow \gamma\gamma$ have an acollinearity angle distribution (Fig 7.6) which is strongly peaked at low values of ξ.

6) Events satisfying the above cuts and also satisfying the BHASEL cuts were classed as Bhabha events and were removed from the class A events.

7.2.2 Selection of Class B events

Candidate events were required to satisfy the cuts 2) - 6) from the class A selection and the following additional cuts.

1) Any trigger combination in which the total energy trigger and a trigger other than the pretrigger was set.

The total energy trigger selects events with energy deposits of > 2 GeV in opposite counters groups, additional triggers are set when tracks have been identified by the DC prepro.

2) the number of reconstructed tracks NTR was required to be ≤ 2

3) the summed momenta of these tracks $\sum_{i=1}^{NTR} P_i$ was > 2 GeV/c

4) If NTR = 2 then only events with $\theta_{12} < \pi/2$ were selected, where θ_{12} is the angle between the tracks in the R-ϕ projection

Cuts 2) - 4) were applied to the information produced by the FOREST program. Cut 2) includes events where only one track from a photon conversion is reconstructed and cut 4) will reject 2-prong events where tracks are produced at much larger θ_{12}.

Events where all tracks from a photon conversion were not reconstructed, which were found in a scan of the class A events, were transferred to this dataset. All selected events were passed through the MILL program and cuts 2) - 4) were applied to the milled data.

Both particles produced in a photon conversion pass through the same drift cells when they are produced close to each other. As only one point is assigned in each cell that has been passed through there are often insufficient points to reconstruct both tracks. Events with only a single reconstructed track were accepted as photon conversion candidates for this reason.

To further reduce background the following cuts on the track parameters were made.

5) If NTR = 2 then $\sum_{i=1}^{2} q_i$ should be = 0, where q_i is the charge of track i

6) $|Z_{oi}| \leq 5$ cm

7) $-3\text{ns} \leq \tau_{measi} - \tau_{predi} \leq 4\text{ns}$

Cut 6) required each track to come from a small region along the beam axis around the interaction point. Fig 7.8 shows the projection in

the R-ϕ plane of the tracks from a photon conversion, the d_0 parameter of each track is negative, (from its definition) and can be much larger than the typical d_0 value of a track from a Bhabha scattering event. A cut involving the track parameter d_0 was not used. Cut 7) rejected events where the measured time of flight τ_{meas} was inconsistent with the time τ_{pred} calculated from the path length of the track. Figs 7.9 and 7.10 show the z_0 and τ_{meas} distributions respectively.

Events with two tracks were passed through a photon reconstruction program which is described in Appendix B.

Figs 7.11 and 7.12 show a scatter plot of E_{γ_1}/Ebeam versus E_{γ_2}/Ebeam for the class A and class B datasets respectively, where E_{γ_1} and E_{γ_2} are the photon energies, showing photon energies clustered at the beam energy.

Figs 7.13 and 7.14 show examples of class A events at Ebeam = 6 GeV and 16.5 GeV respectively and Fig 7.15 shows a class B event at Ebeam = 16.5 GeV.

7.3 Background estimation

7.3.1 Background to the class A events

Events from the class A dataset were scanned using a program which displayed views of the detector including information from all of its components. Views of parts of the whole detector were also available.

An $e^+e^- \rightarrow \gamma\gamma$ event where neither photon has converted before the DC should have no tracks visible in the DC and should have no hits in the muon tubes. Hits can occur in the ITOF counters through showering of a photon in them or in the coil, but the multiplicity of ITOF counters, N_{TOF}, should be small. This was used as the basis of event selection and all events satisfying any of the following conditions were regarded as background.

1) a track was seen in the DC

2) hits occurred in the muon tubes

3) $N_{TOF} > 4$

Only one of the rejected events was attributable to beam-gas

scattering, the remainder (130 events) being from cosmic rays. The cosmic ray events were characterised either by tracks passing through the DC with many hits in muon tubes, or by many hits in the muon tubes but with no observable tracks. Tracks passing through the DC were not reconstructed by the FOREST program as they were too far from the interaction point and in some cases a track just grazed the DC resulting in a band of ITOF counters. Figs 7.16 and 7.17 show two typical cosmic ray events with observable tracks, the first event has a well defined track in the DC while the second shows a track which just grazes the DC. Fig 7.18 shows a typical cosmic ray event with no observable tracks, many of this type occurred in the hadron arms where the shower counters are far from the tracking chambers.

A set of software cuts were designed to sort the previously selected background events from the class A dataset. The number of struck muon tubes, N_M, for each of the muon chambers behind installed shower counters and the number, N_D, of DC 0° layer wires firing were calculated.

The following cuts were used:

1) $N_M < 10$, for each muon chamber

2) $N_{TOF} \leq 4$

3) $N_D \leq 45$

Cut 3) could not be made more restrictive due to the large number of random hits in the DC, where the average number of hits for non-background events is 15 with a tail extending up to 45 hits. The above cuts removed ~ 65% of the background events identified using the display program and a further 16% of background events were removed by rejecting events with more than 6 energy clusters. The remaining background events could not be separated from good events without scanning, as the hit multiplicity N_D of their tracks was indistinguishable from the number of random hits.

A sensitive test for remaining background events is to compare the number of events with acollinearity angle $\xi > 20°$ with the number predicted

by the Monte-Carlo program, described in section 7.7. As the ξ distribution of $e^+e^- \rightarrow \gamma\gamma$ events is peaked at small angles the background will be relatively larger in this region. Fig 7.19 a) and Fig 7.19 b) show the ξ distribution of the final event sample and the background events respectively. The distribution for the background events, Fig 7.19 b), is flat. Table 7.1 shows the number of events predicted and seen for several ranges of ξ, the agreement shows that the final event sample is very clean. A background of less than one event has been estimated from the tail of the acollinearity distribution.

7.3.2 Background to class B events

The class B dataset was scanned to exclude background events. Events were rejected as background if they satisfied any of the following conditions.

1) a track was seen in the DC which does not pass through the cylinder defined by its second layer
2) hits occurred in the muon tubes
3) the multiplicity of ITOF counters, $N_{TOF} > 5$

The remaining backgrounds, from gamma-gamma scattering to leptons and beam-gas scattering are calculated below.

a) Beam-gas scattering

The contamination from this process was determined from the observed z_0 distribution after all the cuts, apart from the z_0 cut, described in section 7.2.2 had been applied. Events where a track had $|z_0| > 8$ cm were classed as background, as this type of event can have vertices at any point along the beam pipe. Assuming a flat background distribution the contribution from this process was estimated by extrapolation into the region $|z_0| < 5$ cm and is calculated to be 0.06 events.

b) Gamma-gamma scattering to leptons

The contribution from this process, where Fig 6.12 shows the lowest order diagrams, was determined using a Monte Carlo generator[79] which calculated the matrix element of the diagrams. Final state leptons and

photons were passed through a program which simulated the trigger, interactions of particles in the material preceding the DC and the resolution of the DC for accepted tracks. Accepted monte-carlo events were required to be selected by the shower counter trigger acceptance program which is described in section 7.5. The remaining events which fail the Bhabha selection cuts described in section 6.2 were then passed through the cuts described in section 7.2.2. The contamination was estimated from the remaining events to be 0.22 events.

Other processes that could contribute to the background are $e^+e^- \rightarrow q\bar{q}\gamma$ and $e^+e^- \rightarrow e^+e^-\gamma$, the background from both these processes was calculated to be less than 0.01 events and was therefore neglected.

7.4 Selection of Bhabha events

Events from the reaction $e^+e^- \rightarrow \gamma\gamma$ were selected using the cuts, described in section 7.2, which search for collinear energy deposits of $E > 2$ GeV in the calorimeters of the detector. The final state of the reaction $e^+e^- \rightarrow \gamma\gamma$ consisting of two collinear photons is topologically similar to the final state of Bhabha scattering ($e^+e^- \rightarrow e^+e^-$) which consists of a collinearly produced electron and positron. Also all the particles will produce an electromagnetic shower in the calorimeters, where assuming that the shower is contained all of the incident energy will be deposited. These similarities in the two reactions mean that the Bhabha scattering events, where both charged particles enter the calorimeters, would also be selected by the cuts of section 7.2, and in the absence of tracking information, events from the two reactions would be indistinguishable.

The acceptance of the tracking chambers is larger and includes all of the acceptance of the calorimeters used in the trigger, consequently all the Bhabha events selected by the total energy trigger should also have been selected by the topology trigger. As the total energy trigger is independent of the topology trigger the Bhabha events selected using the cuts

of section 7.2 can be used to estimate the efficiencies of the topology trigger and the pretrigger. The calculation of these efficiencies has been described in section 6.4.

The FOREST efficiencies can also be calculated from this sample of Bhabha events. The R-ϕ efficiency was calculated from the fraction of events with fewer than two reconstructed tracks and the z efficiency was calculated from the fraction of events with two tracks reconstructed in the R-ϕ projection but not in the z projection. These efficiencies are given in Table 7.2 and were used in the Monte Carlo program described in section 6.4.

7.5 Shower counter geometrical acceptance

Bhabha events, selected by the cuts of section 6.2, have been used to check the surveyed positions of the shower counter groups. Tracks found in the DC were used if they were correlated with an energy deposit $\geq$ 4 GeV in any shower counter group. These tracks were projected into the planes formed by the shower counter groups and the distribution of their points of intersection compared with the surveyed positions.

The hadron arm shower counters and the counters above the coil had surveyed positions which were consistent with tracking measurement errors and interactions in the coil. For the shower counters below the coil there was a displacement of the positive z direction and one counter module was slightly displaced into the positive x direction. The major gaps between groups of shower counters were visible but any gaps between individual counter modules were too small to be resolved.

The corrected positions of the shower counters have been used to calculate the geometrical acceptance for the 1979 and the 1980 data taking periods. The geometrical acceptance for 1979 is 44.1% of 4π ster and for 1980 is 32.8% of 4π ster, the smaller value for 1980 is a result of the transfer of the counters above the coil to the hadron arms and

does not include the geometrical acceptance of the LABC modules. Fig 7.20 shows the geometrical acceptance as a function of cosθ for the 1979 and 1980 geometries.

7.6 Shower counter trigger efficiency

Bhabha events, selected by the cuts of section 6.2, where both or one of the charged particles entered the shower counters can be used to calculate the efficiency of the shower counter trigger in an unbiased way. In addition the efficiency of the LABC modules can be calculated although this detector was not part of the trigger.

Events with more than 2 GeV energy deposited in opposite shower counter groups were used. The trigger efficiency was calculated from the ratio of events with and without the shower counter energy trigger set. For the 1980 data taking period the LABC efficiency was calculated from the subset of events with an energy deposit of more than 2 GeV in the shower counters below the solenoid, from the ratio of events with and without an energy deposit of more than 2 GeV in the LABC. These efficiencies are given in Table 7.3 as a function of centre of mass energy W.

7.7 Monte Carlo simulation of class A events

The acceptance of the reaction $e^+e^- \rightarrow \gamma\gamma$ was calculated using a Monte Carlo program, consisting of an event generator and a simulation of the detector using the EGS[72] program. The Monte Carlo events were stored in the same way as the data of real events allowing the same analysis routines to be used.

7.7.1 Event generator

Events were generated using the method of Berends and Kleiss[83]. The final states $\gamma\gamma$ and $\gamma\gamma\gamma$ were produced correct to order (α^3) assuming no polarisation effects, using the diagrams shown in Fig 1.11 and Fig 1.12.

7.7.2 Detector simulation

The EGS program was used to simulate the development of electromagnetic showers, which are generated by the passage of the final state photons through the material of the detector. The EGS program code is fully described in reference 72, only the detector geometry used will be given here.

The material of the detector within the solenoid was simulated as 13 cylindrical layers, where the thickness, mean radius and the part of the detector simulated by each layer is listed in Table 7.4. When a layer is made from more than one material it was considered to be made from the major material with its thickness rescaled to the correct number of radiation lengths. Scintillator was parameterised as a compound of carbon and hydrogen with the relative proportions C/H = 1/1. All intervening gaps between the layers were considered to be vacuum.

Particles from the electromagnetic shower were projected towards the shower counters. The counters formed 11 rectangular groups which described all of the different configurations used during the experiment. From the point of intersection of a particle with the front surface of a group the shower counter module struck was calculated. Any particles which did not intersect a group were discarded. The stack geometry used is given in Table 7.5. At each stage of the shower the position of the showering particles was used to calculate in which module the shower was contained. In this way any energy deposited could be assigned to a particular shower counter and the different configurations used could be simulated by turning off absent modules. Particles passing through the back and sides of a group were considered as shower leakage and were discarded.

The response of a module is only uniform in the direction parallel to the wavelength shifter bar. The response of a module in the direction perpendicular to the wavelength shifter bar was parameterised from the

response measured in a test beam (Fig 4.20) using equation 5.2.2. From the position of each particle in the module a weight was calculated and the weighted energy deposited in the 9 layers of scintillator was calculated for each of the counter modules.

The energy deposited in each module was converted into a pedestal subtracted ADC value, using the measured distribution of pedestal subtracted ADC values from the Bhabha scattering events selected in section 7.4. A global factor was applied as there was insufficient data to calculate an individual shift for each counter, the peak energy value corresponding to 2600 counts. To account for overflows in the ADC's any pedestal subtracted ADC value above 3700 counts was set to 3700. The peak ADC value for Xenon lamp calibration data, of 1320 counts, was then used to convert each ADC value into an energy measurement. Apart from the substitution of global for individual calibrations, equation 5.2.1 was used to convert the ADC values into an energy measurement. The BHACAL factor of equation 5.2.1 used, of size 0.8, was consistent with the typical value of 0.78 measured from data. Equations 5.2.3, 5.2.4 and 5.2.5 were then used to correct for energy leakage and for the angle of incidence with the shower counters.

The LABC modules were not simulated using the EGS program as they were not part of the total energy trigger. The 4 rectangular modules of the calorimeter had photons projected towards them. If a photon intersected a module then its energy and direction cosines were smeared by gaussian distributions which were parameterised by the energy distribution and θ and ϕ distributions measured from data.

The analysis routines described in section 7.1.1 were then applied to the Monte-Carlo events.

The EGS program was checked by comparing the number of photons converting before the DC with the number predicted from the amount of

material x, using the probability $P = (1-e^{\frac{-.7778x}{\sin\theta}})$, which is given in Table 7.6 for several ranges of cosθ. The agreement is very good.

The Monte Carlo gives a good description of the energy spectrum and the angular distributions of photons measured in the shower counters. The systematic error was estimated by comparing the acceptance with the acceptance calculated when the response of the shower counter modules was taken to be uniform and was found to be ± 5%.

7.8 Monte Carlo simulation of class B events

The acceptance of class B events was calculated by a separate Monte Carlo program. The event generator used was given in section 7.7.1 and the detector simulation was described in section 6.4. A shower counter simulation program was added to the detector simulation and the order of the programs describing the software was altered to account for the different selection procedure adopted for these events. The shower counter simulation program and the software chain used are given below.

7.8.1 Shower counter simulation program

Charged particles and photons were projected towards the shower counters which were treated as 9 rectangular groups for the 1980 data taking period. The energy of particles entering the shower counters was smeared by a gaussian distribution with a resolution parameterised from data. The LABC modules installed above the coil were simulated in the same way with a resolution parameterised from data[50]. Events were selected if they satisfied the cuts 2) - 4) described in section 7.2.

7.8.2 Software chain

FOREST was applied to events selected by the shower counter simulation program. Events without the pretrigger set were selected to account for events converting in the synchrotron radiation shield which would be selected by the class A cuts. Events with tracks identified by the DC

prepro had the cuts 2) - 4) described in section 7.3 applied and any events satisfying the BHASEL cuts were rejected.

The MILL program was applied to all remaining events and any events with no reconstructed tracks were rejected. Cuts 2) - 7) described in section 7.3 were applied and the photon reconstruction program described in appendix B was used to calculate the effective mass of track pairs. Events with single tracks were accepted along with events with two oppositely charged tracks and an effective mass < 250 MeV/c^2.

The description of the data by the Monte Carlo program has been checked in four ways. As discussed in section 7.2.2 photon conversion events can have either one or two reconstructed tracks and the track parameter d_o will tend to have negative values. In the final data sample the fraction of events with two reconstructed tracks 45.8 ± 17% is in good agreement with the fraction 47% predicted by the Monte Carlo. Fig 7.21 and Fig 7.22 show the measured d_o distribution of all tracks and the effective mass distribution of track pairs after the photon reconstruction program. The curves represent the prediction of the Monte Carlo program, again there is good agreement with the data. Finally the fraction of events with photons converting in the synchrotron radiation shield was compared with the prediction of the Monte Carlo program. These events were identified by all reconstructed tracks having no hits in the CPC anode layers. The predicted fraction 39.7% is in good agreement with the measured fraction of 45.8 ± 17%.

The systematic error of the detector simulation program was calculated in section 6.4 as ± 5%.

7.9 Data analysis

Using the class A data the cross section was evaluated as a function of centre of mass energy W and a search for events with three observable photons was made. The differential cross-section was also calculated and was

then used to test QED using the two models discussed in section 7.1. The cross-section for the class B data was evaluated.

7.9.1 Total cross-section

a) Class A

The number of events predicted by the Monte Carlo program was compared to the number of events in the final data set to determine the total cross-section. The number of events predicted was normalised to the measured luminosity.

Data taking was performed in the 'scan' mode where approximately 30 nb^{-1} luminosity was collected at each energy point with an interval of 10 MeV between points. Data were grouped together in bins of width 0.5 GeV with the centre of mass energy W taken as the average of the bin. Table 7.7 shows the cross-section as a function of W with the luminosity, the measured no of events and the predicted number of events in each bin. The corrections for the energy trigger efficiency and the LABC efficiency were calculated separately for each bin, using the events from the Bhabha data sample described in chapter 6 in the same energy interval. For the combined high energy data at an average W of 34.8 GeV $\sigma_{meas}/\sigma_{QED}$ = 1.01 ± .10 for a total of 5400 nb^{-1} luminosity, and for the data at W = 12 GeV $\sigma_{meas}/\sigma_{QED}$ = 0.95 ± .24 for a total of 95 nb^{-1} luminosity.

b) Class B

The cross-section of class B events was determined by comparing the number of events in the final dataset to the number of events predicted by the Monte Carlo program. The predicted no of events was corrected by the energy trigger and LABC efficiencies calculated using the Bhabha data sample and was normalised to the measured luminosity. Table 7.7 shows the cross-section and the measured and predicted no of events. For the class B data at an average W of 34.8 GeV $\sigma_{meas}/\sigma_{QED}$ = .85 ± .17 for a total of 5400 nb^{-1} luminosity.

7.9.2 Differential cross-section

The measured differential cross-section is shown in Fig 7.23 for the combined high energy data at an average W of 34.8 GeV and the data at W = 12 GeV. The solid curve represents the lowest order QED differential cross section, equation 7.1.2. Each event was given a weight, where the weight W_j of bin j was determined from the Monte Carlo program,

$$W_j = a_j^{-1} r_j^{-1} \qquad - 7.9.1$$

r_j represents the radiative correction and a_j the acceptance.

Only eight bins in cosθ were possible from the geometry of the shower counters and to improve the statistics in each bin the curve was folded about the point $\theta = \pi/2$ (the differential cross-section represented by equation 7.1.2 is symmetrical in cosθ about the point $\theta = \pi/2$). The corrections for the energy trigger and LABC efficiencies were calculated for each bin in cosθ using the Bhabha data sample. A correction for individual shower counter modules was not possible due to limited statistics. The data points were normalised to the measured total cross-section. Table 7.8 gives the ratio of the measured differential cross-section to the QED prediction for each bin at W = 34.8 GeV and W = 12 GeV.

7.9.3 Tests of QED

The measured differential cross section at W = 34.8 GeV was compared with the predicted differential cross section from each of the models describing modifications of QED. The chisquare was minimised to determine the parameters $\Lambda^{\pm}$ where:

$$\chi^2 = \sum_j \left(\frac{d\sigma o}{d\Omega_j} - \frac{d\sigma}{d\Omega_j} \right)^2 / \Delta^2 \frac{d\sigma}{d\Omega_j} \qquad - 7.9.2$$

$d\sigma/d\Omega_j$ and $\Delta d\sigma/d\Omega_j$ are the measured differential cross section in bin j and its error respectively and $d\sigma o/d\Omega_j$ is the predicted differential cross section in bin j.

a) Heavy electron exchange

In this case equation 7.1.7 was used to represent $d\sigma_e/d\Omega_j$. Fig 7.24 a) shows the plot of χ^2 vs $^1/\Lambda^4$ obtained from equation 7.9.2, which is a parabola. The shift of the parabola minimum from the point $^1/\Lambda^4 = 0$ is due to the difference in the measured cross section from the QED prediction. Table 7.9 shows the minimum value of the parameter $^1/\Lambda^4$ calculated at W = 34.8 GeV. The minimum value of the parameter $^1/\Lambda^4$ and its error were used to calculate the cut off parameters $\Lambda\pm$, where $\Lambda+$ = 44.2 GeV and $\Lambda-$ = 43.9 GeV at 95% confidence. Using the value of $\Lambda+$ obtained and equation 7.1.7b a plot of Me^{*2}, where Me^* is mass of the heavy electron, as a function of the coupling strength λ was calculated. This is shown in Fig 7.25 where the shaded region represents values of Me^* which are excluded at 95% confidence. If the coupling strength is the same as for unmodified QED ($\lambda = 1$) then the mass of the heavy electron is > 44.2 GeV at 95% confidence. Fig 7.26 shows the measured differential cross-section, divided by the QED prediction as a function of $\cos\theta$, superimposed are curves representing the modified predictions corresponding to $\Lambda+$, $\Lambda-$ respectively.

b) Seagull graph

In this case equation 7.1.12 was used to represent $d\sigma_e/d\Omega_j$. The plot of $^1/\Lambda^4$ vs χ^2 obtained from equation 7.9.2, which is a parabola, is shown in Fig 7.24 b). The shift of the parabola minimum from the point $^1/\Lambda^4 = 0$ is due to the difference in the measured cross-section from the QED prediction. The minimum value of the parameter $^1/\Lambda^4$ obtained is shown in Table 7.9 for the combined high energy data at W = 34.8 GeV. The cut off parameters $\Lambda\pm$ were calculated from the minimum value of the parameter $^1/\Lambda^4$ and its error, where $\Lambda+$ = 41.4 GeV and $\Lambda-$ = 41.9 GeV at 95% confidence level. Fig 7.26 shows the measured differential cross-section divided by the QED prediction as a function of $\cos\theta$, superimposed are

curves representing the modified predictions corresponding to $\Lambda+$ and $\Lambda-$ respectively. The values of $\Lambda\pm$ are comparable with the values obtained from the heavy electron exchange modification.

7.9.4 Systematic error

The systematic error was estimated as ± 7% by adding the uncertainty in the acceptance (± 6%) and the luminosity (± 4%) in quadrature.

7.9.5 3γ events

If the cross section for the reaction $e^+e^- \rightarrow \gamma\gamma$ is calculated to order (α^3) then the reaction $e^+e^- \rightarrow \gamma\gamma\gamma$ must also be considered, where the additional photon may have enough energy to be observed.

A search for events with three observable photons was made in the class A data, which corresponds to an average W of 34.8 GeV, using the cluster finding method described in chapter 5.

The cluster finding algorithm was tested by applying it to the Bhabha data sample, corresponding to the same data taking period, where a single high energy cluster would be expected for each track projected into the shower counters. Table 7.10 shows the cluster multiplicity observed for each counter group which is consistent with 1 for each of the groups. Table 7.10 also shows the cluster multiplicity observed in each group for the class A data, again this is consistent with 1 for each of the groups. For the events with more than one cluster in a group the energy deposit in the lowest energy cluster was < 1 GeV.

The number of three photon events expected was calculated using the Monte-Carlo program described in section 7.7. A subset of the generated events was used where three photons entered the detector, comprising 4.2% of the accepted events. These events were examined to see if any of them had three observable clusters.

In 11% of the events the third photon was unobservable (E < 100 MeV), 16% of the events failed the cuts described in section 7.2 and in 37% of

the events the third photons deposited energy was < 2 GeV or it was not sufficiently separated from one of the other photons to be observable. The remaining 36% of the events had a photon with an energy deposit > 2 GeV and a well separated cluster.

The number of events expected was calculated using the events with all three photons having an energy deposit > 2 GeV. Excluding events where a photon has converted and correcting for the energy trigger and LABC efficiencies, the number of three photon events expected is 1.04 ± .39 events. This is consistent with the data where none are seen.

7.10 Conclusions

The reaction $e^+e^- \rightarrow \gamma\gamma$ has been studied at centre of mass energies W between 12 and 36.6 GeV. The ratio of the measured cross-section to the QED prediction $\sigma_{meas}/\sigma_{QED}$ is 1.01 ± .10 at W = 34.8 GeV and is .95 ± .24 at W = 12 GeV, both measurements are in good agreement with QED. The cross section has also been measured at W = 34.8 GeV for events where a final state photon has converted into an e^+e^- pair before the drift chamber, the measurement $\sigma_{meas}/\sigma_{QED}$ = .85 ± .17 is also in good agreement with QED. The measured differential cross-section $sd\sigma/d\Omega$ at W = 12 GeV and W = 34.8 GeV is consistent with the QED curve and is independent of s. Two models describing modifications of QED have been tested by comparing the measured differential cross-section at W = 34.8 GeV with the differential cross-section predicted by each model. Each model is parameterised by the cut off parameters $\Lambda\pm$. The cut off parameters for the model involving a "seagull" graph are $\Lambda+$ = 41.4 GeV and $\Lambda-$ = 41.9 GeV at 95% confidence, while for the model involving heavy electron exchange graphs they are $\Lambda+$ = 44.2 GeV and $\Lambda-$ = 43.9 GeV at 95% confidence. In the case of the model involving heavy electron exchange, if the coupling strength is the same as for unmodified QED (λ = 1) then at 95% confidence the mass of the heavy electron is > 44.2 GeV. Both sets of cut off parameters confirm

the validity of QED at present values of Q^2 (Q^2 max ~ 1300 GeV^2). The number of events with 3 final state photons ($e^+e^- \rightarrow \gamma\gamma\gamma$) observable after all cuts, 1.04 ± .39 events, is consistent with the data where none are seen.

Acolliniarify angle range (degrees)	Number of events predicted	Number of events observed
0 — 5	65·5	65 ± 8·1
5 — 10	38·3	40 ± 6·3
10 — 20	9·1	3 ± 1·7
20 — 40	4·4	5 ± 2·2
40 — 60	1·8	3 + 1·7
>60	0·7	2 ± 1·4

Table 7·1 predicted and observed no. of events in bins of acollinearity angle

r−ø efficiency per track (1st pass)	0·9 ± 0·02
z efficiency per track	0·9 ± 0·06

Table 7·2 FOREST efficiencies

W (GeV)	shower counter efficiency (%)	LABC efficiency (%)
12·0	70·3	not installed
30·0	64·3	89·3
32·5	54·8	10·0
33·5	59·7	89·3
34·5	64·5	63·5
35·5	63·4	79·2
36·6	71·4	77·6

Table 7·3 shower counter trigger and LABC efficiencies

part of the detector simulated		mean radius (cm)	thickness (radiation lengths)
beam pipe		13·27	0·061
beam pipe counters		15·10	0·012
CPC inner wall		18·00	0·0063
CPC 1 partition		20·25	0·0069
CPC 2 partition		23·30	0·0069
CPC 3 partition		26·35	0·0069
CPC outer wall		28·59	0·0063
synchrotron radiation shield	layer 1	31·92	0·011
	layer 2	32·00	0·05
	layer 3	32·08	0·011
DC inner wall		32·50	0·032
DC outer wall		122·45	0·056
ITOF counters		133·00	0·048
solenoid		139·45	1·00

Table 7·4 parameterisation of the material of the inner detector

material simulated	thickness (cm)	depth (cm)
scintillator	1·0	0·0
lead	0·5	1·0
scintillator	1·0	1·5
lead	0·5	2·5
scintillator	1·0	3·0
lead	0·5	4·0
scintillator	1·0	4·5
lead	0·5	5·5
scintillator	1·0	6·0
lead	0·5	7·0
scintillator	1·0	7·5
lead	0·5	8·5
scintillator	1·0	9·0
lead	0·5	10·0
scintillator	1·0	10·5
lead	0·5	11·5
scintillator	1·0	12·0

Table 7·5 parameterisation of the shower counter stack

cos θ range	conversion probability/trk fromEGS (%)	conversion probability/trk (%)
0·0 — 0·1	11 · 64	12 · 96
0·1 — 0·2	12 · 75	13 · 09
0·2 — 0·3	13 · 00	13 · 34
0·3 — 0·4	13 · 07	13 · 76
0·4 — 0·5	14 · 84	14 · 38
0·5 — 0·6	13 · 18	15 · 30
0·6 — 0·7	18 · 02	16 · 68
0·7 — 0·75	18 · 24	18 · 24

Table 7·6 conversion probability/track in the material before the drift chamber

W (GeV)	luminosity (nb^{-1})	no of events observed	predicted no of events	$\sigma_{meas}\backslash\sigma_{QED}$
class A data				
12·0	95·0	17·0	19·04	0·95 ± ·24
30·0	174·0	3·0	5·30	0·57 ± ·58
33·5	1215·4	39·0	28·10	1·39 ± ·16
34·0	2104·4	35·0	35·32	0·99 ± ·17
35·5	1453·0	23·0	28·30	0·81 ± ·21
36·6	351·8	5·0	6·70	0·75 ± ·45
class B data				
34·8	5400·0	24·0	28·28	0·85 ± ·17

Table 7·7 measured cross-section, luminosity and no. of events seen in bins of W

cos θ range	$\sigma_{meas}/\sigma_{QED}$ (W = 34·8 GeV)	$\sigma_{meas}/\sigma_{QED}$ (W = 12·0 GeV)
0·0 — 0·18	0·90 ± ·20	1·47 ± ·39
0·18 — 0·36	1·14 ± ·18	0·50 ± ·58
0·36 — 0·54	0·92 ± ·19	1·17 ± ·43
0·54 — 0·72	1·08 ± ·23	0·76 ± ·58

Table 7·8 $\sigma_{meas}/\sigma_{QED}$ in bins of cosθ

QED modification	fitted parameter λ (GeV^{-4})	Λ_+ (GeV)	Λ_-
heavy electron exchange	$\frac{1}{\Lambda^4} = (-0.28 \pm 16.31) \times 10^{-8}$	44.2	43.9
seagull graph	$\frac{1}{\Lambda^4} = (0.71 \pm 20.36) \times 10^{-8}$	41.4	41.9

Table 7.9 cut off parameters

group	cluster multiplicity	
	$(e^-e^- \to e^-e^-)$	$(e^-e^- \to \gamma\gamma)$
A	1.00	1.02
B	1.02	1.00
C	1.09	1.07
D	1.01	1.01

Table 7.10 cluster multiplicities observed for $(e^+e^- \to e^+e^-)$ and $(e^+e^- \to \gamma\gamma)$ events

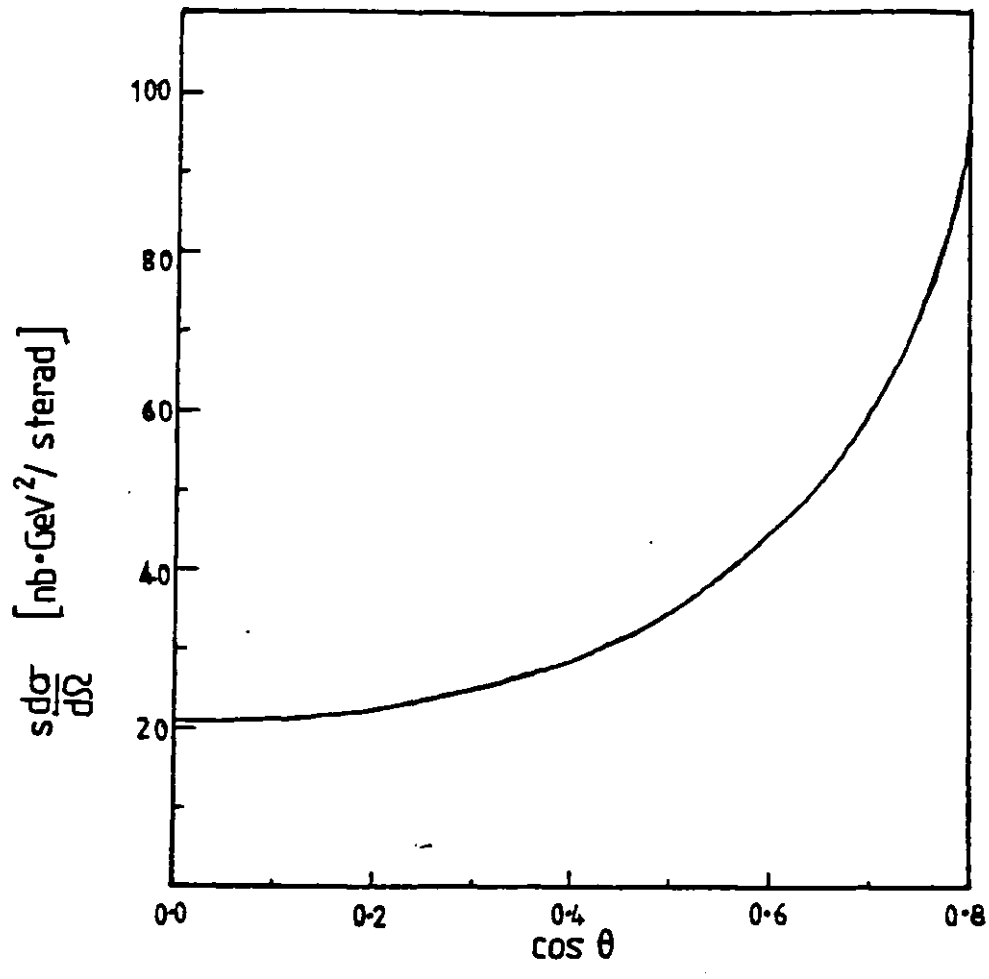


Fig 7·1 lowest order differential cross-section

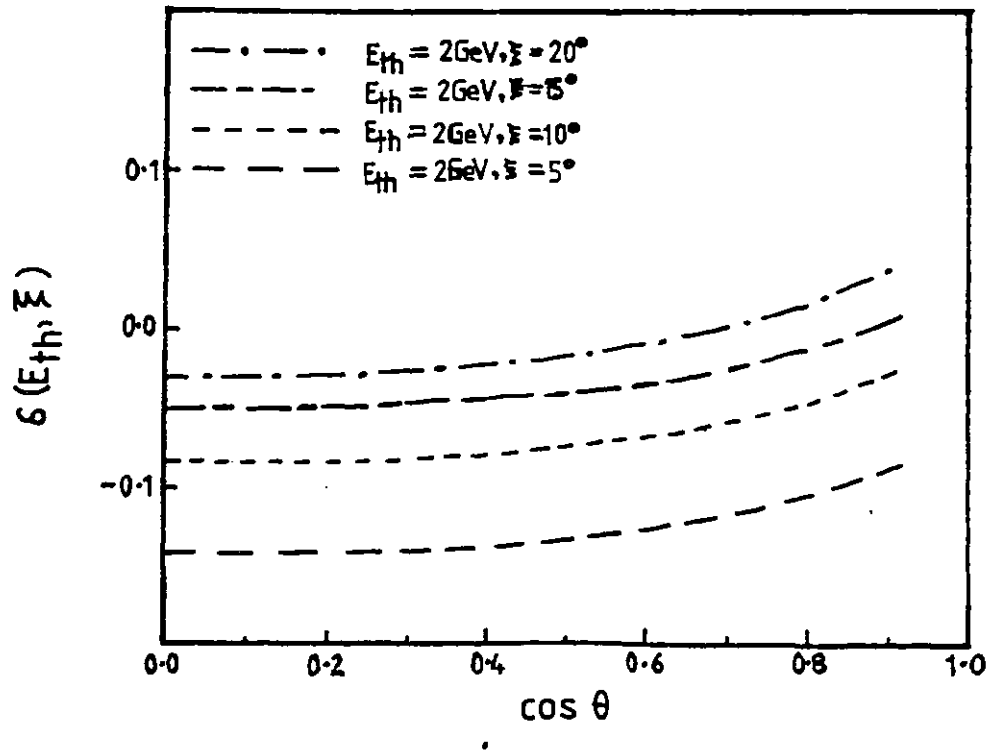


Fig 7·2 radiative correction $\delta(E_{th},\xi)$ v. cosθ for W = 30 GeV

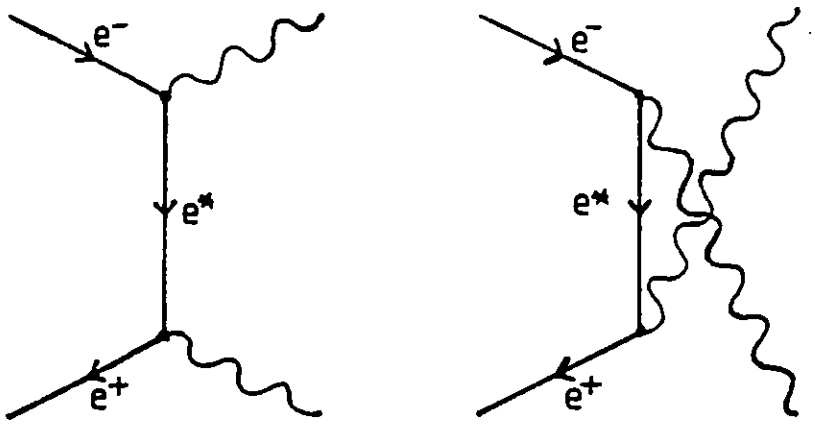


Fig 7·3 heavy electron exchange diagrams

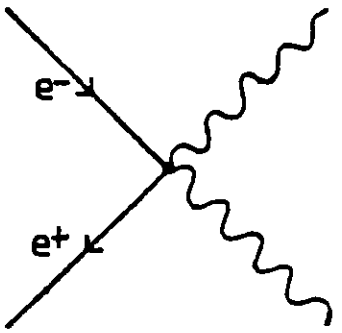


Fig 7·4 seagull diagram

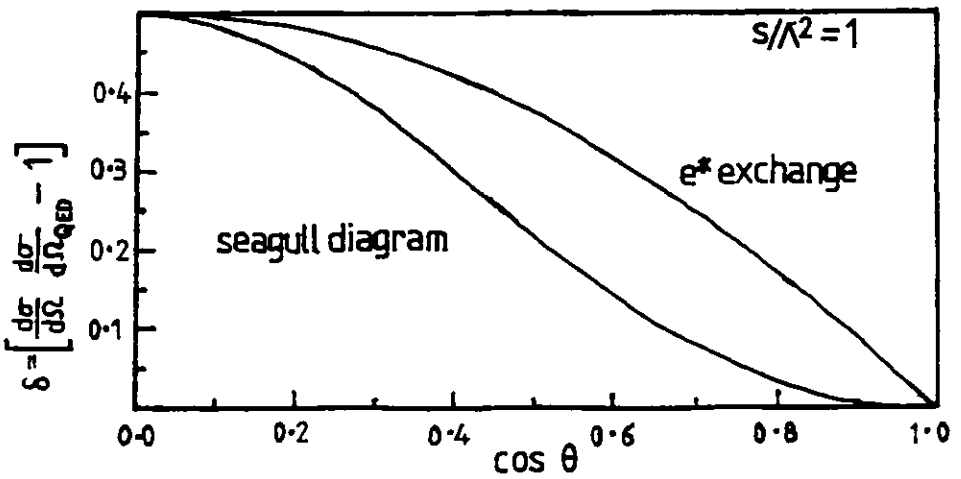


Fig 7·5 $\delta = [(d\sigma/d\Omega)/(d\sigma/d\Omega_{QED}) - 1]$ for $S/\Lambda^2 = 1$

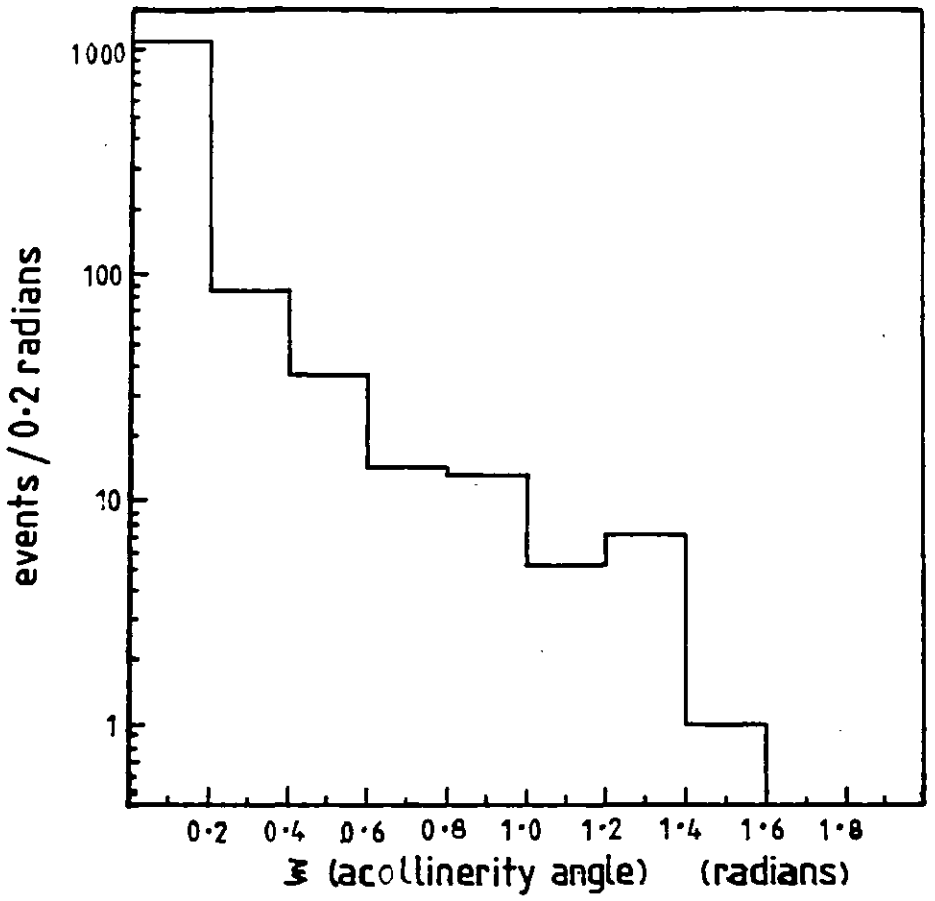


Fig 7·6 acollinearity angle distribution for events generated at W = 34 GeV

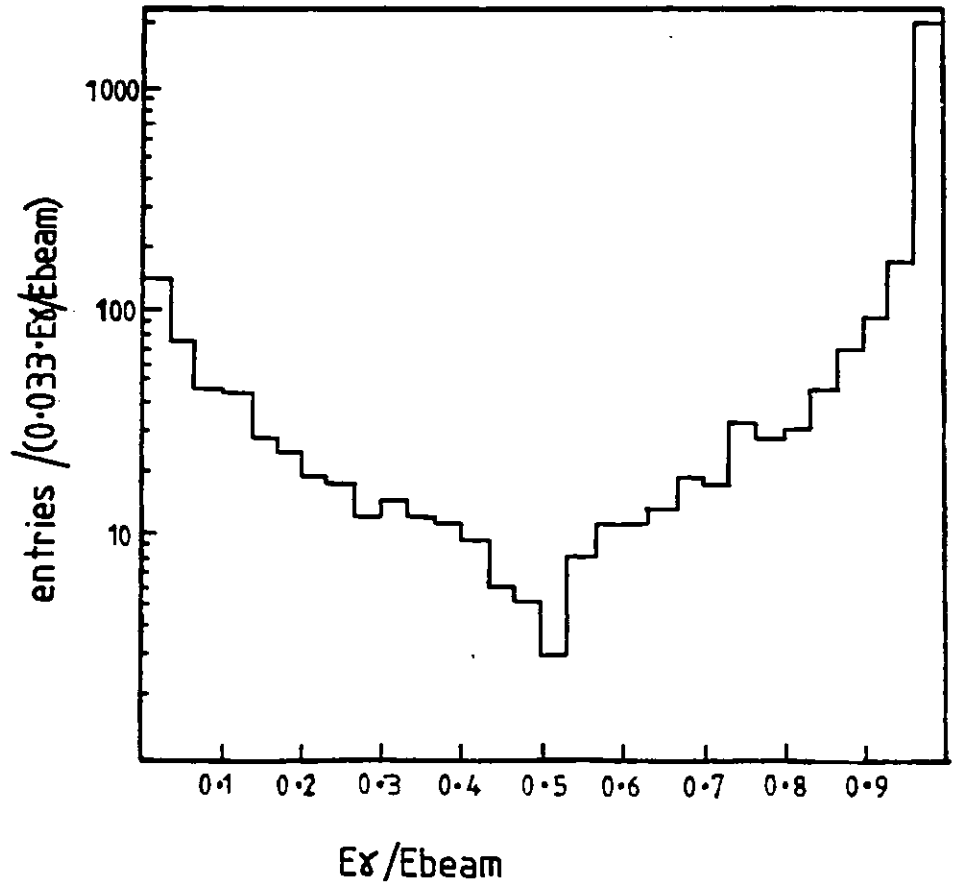


Fig 7·7 normalised photon energy for generated events at W = 34 GeV

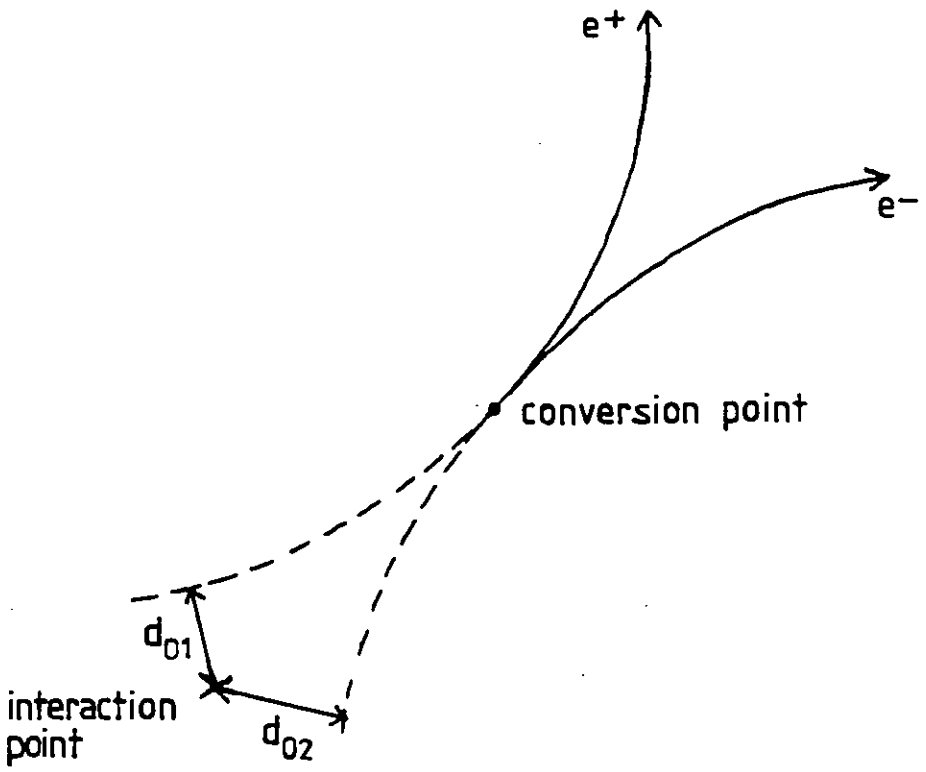


Fig 7·8 r - ϕ projection of the tracks from a photon conversion showing the d_0 parameter of each track

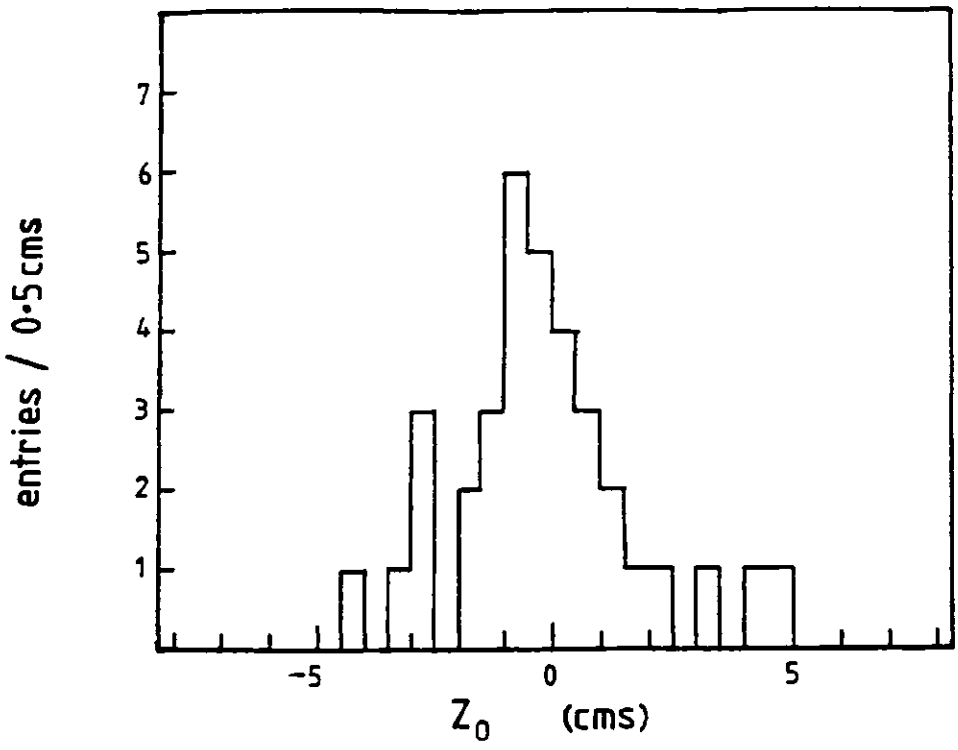


Fig 7·9 Z_0 distribution (class B data)

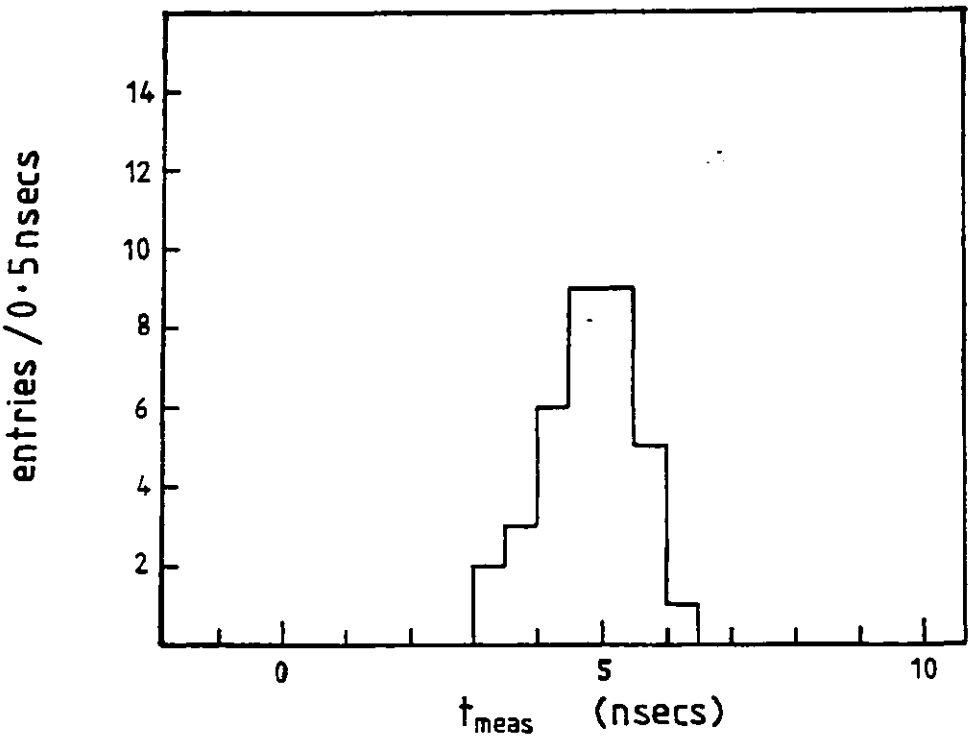


Fig 7·10 t_{meas} distribution (class B data)

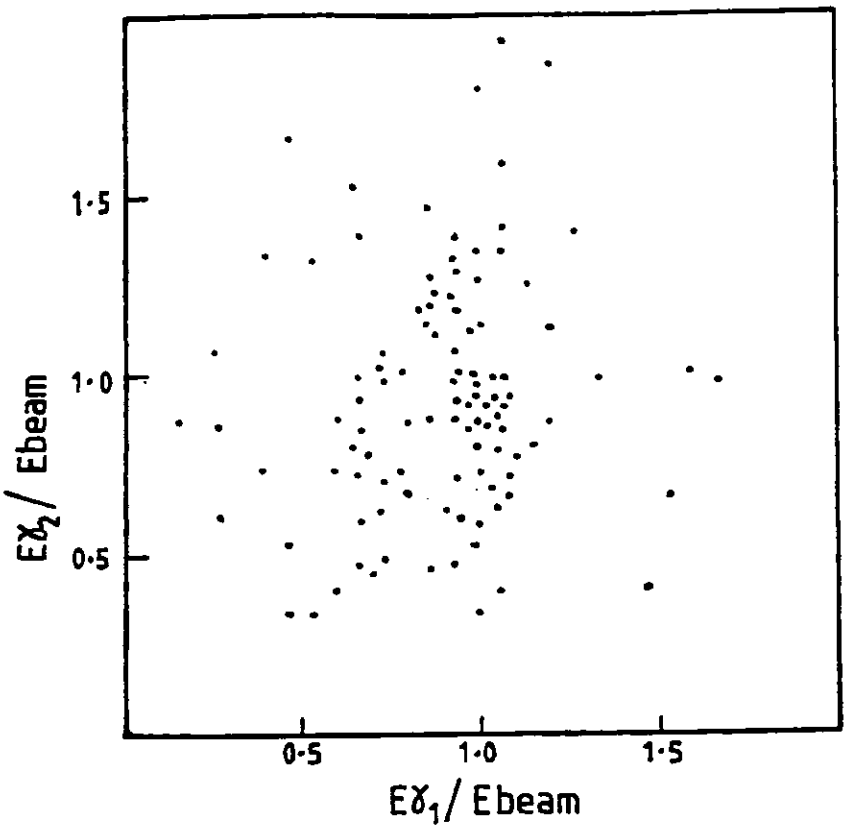


Fig 7·11 E_{γ_1}/Ebeam v. E_{γ_2}/Ebeam (class A events)

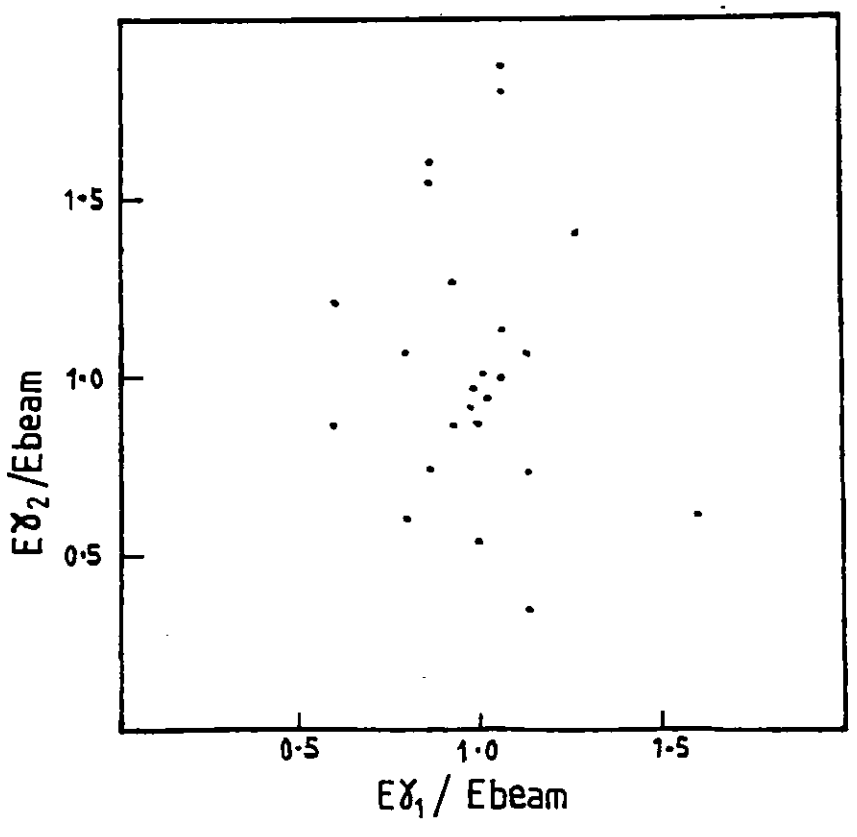


Fig 7·12 E_{γ_1}/Ebeam v. E_{γ_2}/Ebeam (class B events)

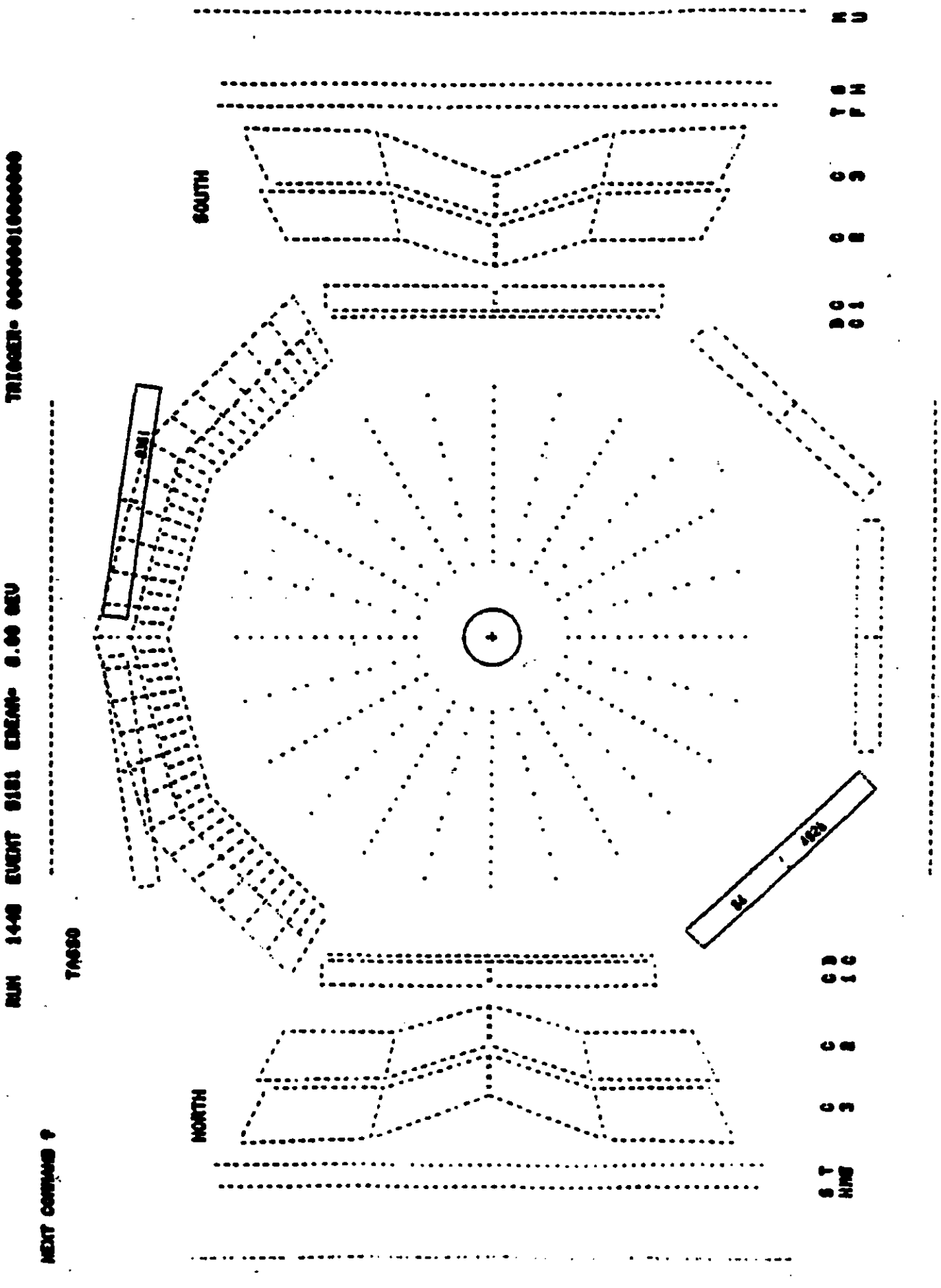


Fig 7·13 $(e^+e^- \to \gamma\gamma)$ event (Ebeam = 6 GeV)

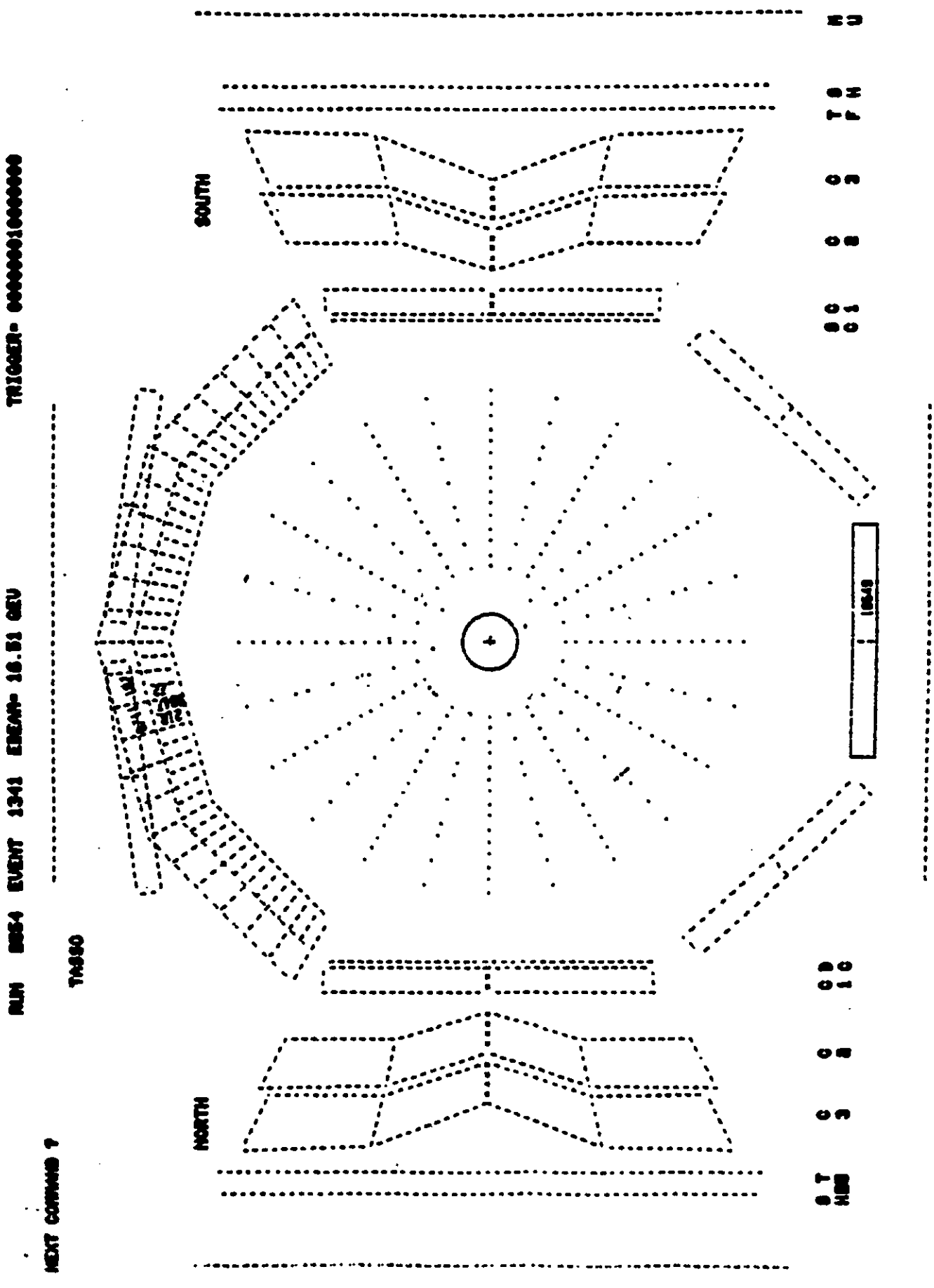


Fig 7·14 $(e^+e^- \to \gamma\gamma)$ event (Ebeam = 16.51 GeV)

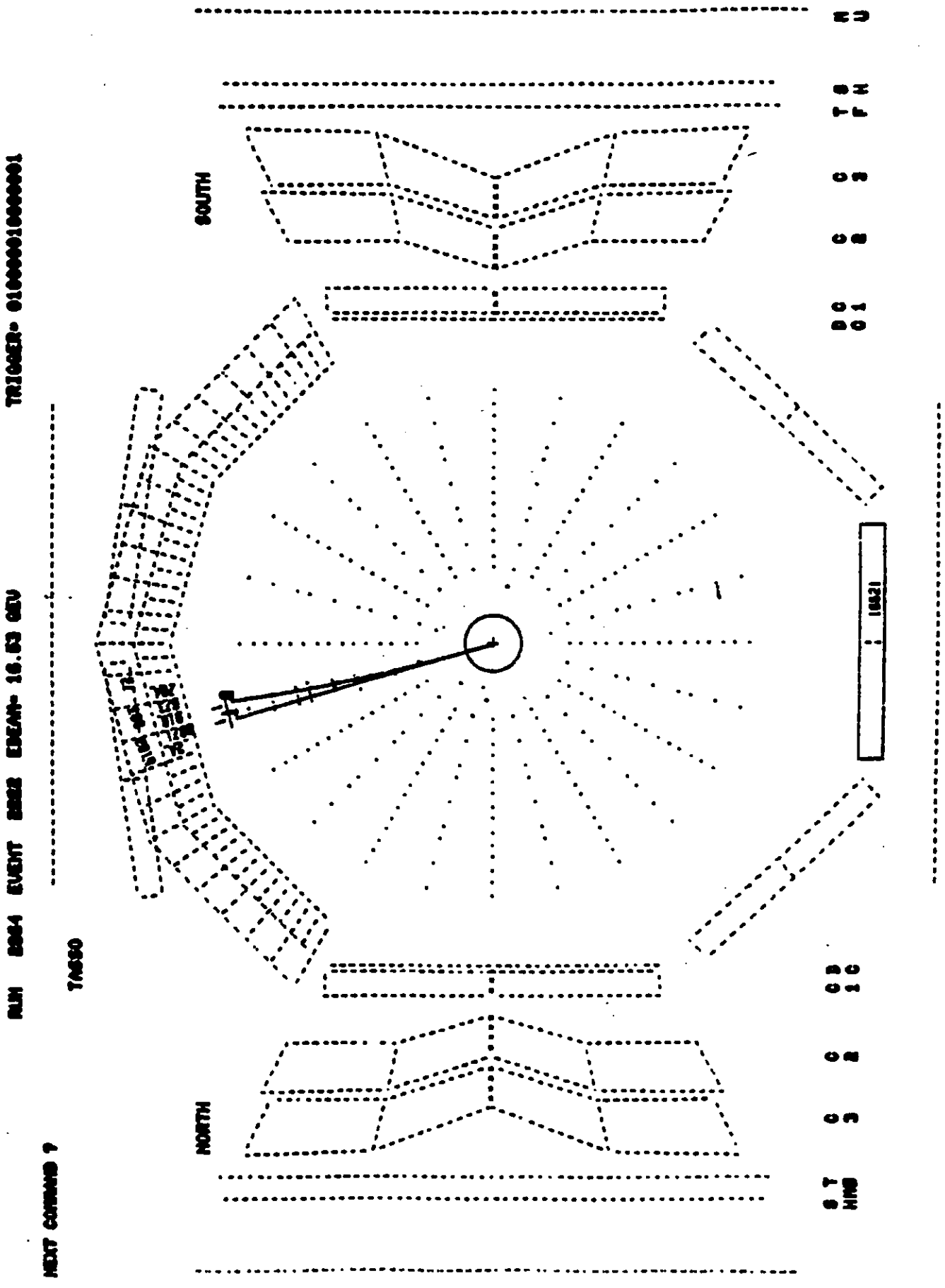


Fig 7·15 ($e^+e^- \to \gamma\gamma$) event with a converted photon (Ebeam = 16.53 GeV)

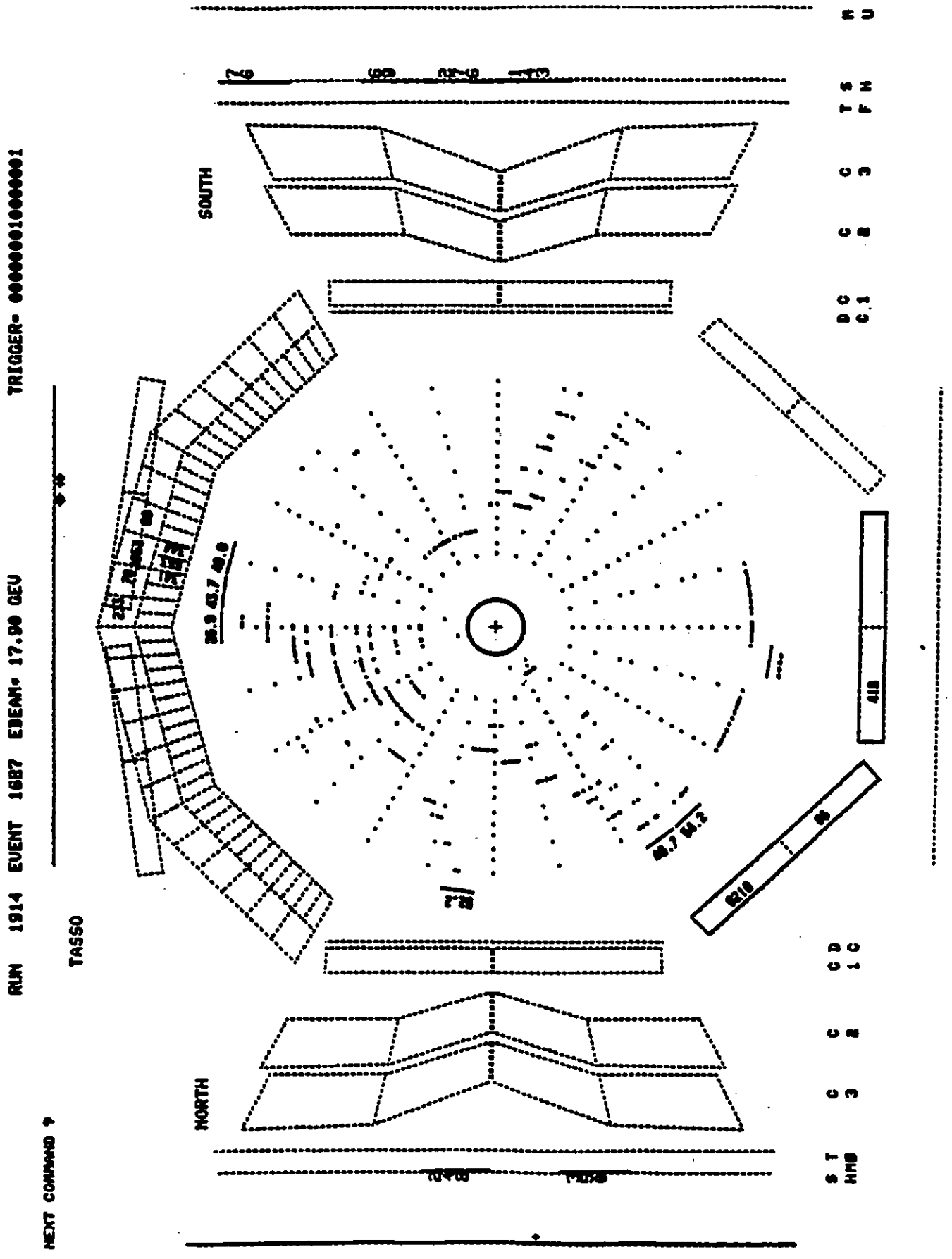


Fig 7·16 background event with drift chamber tracks

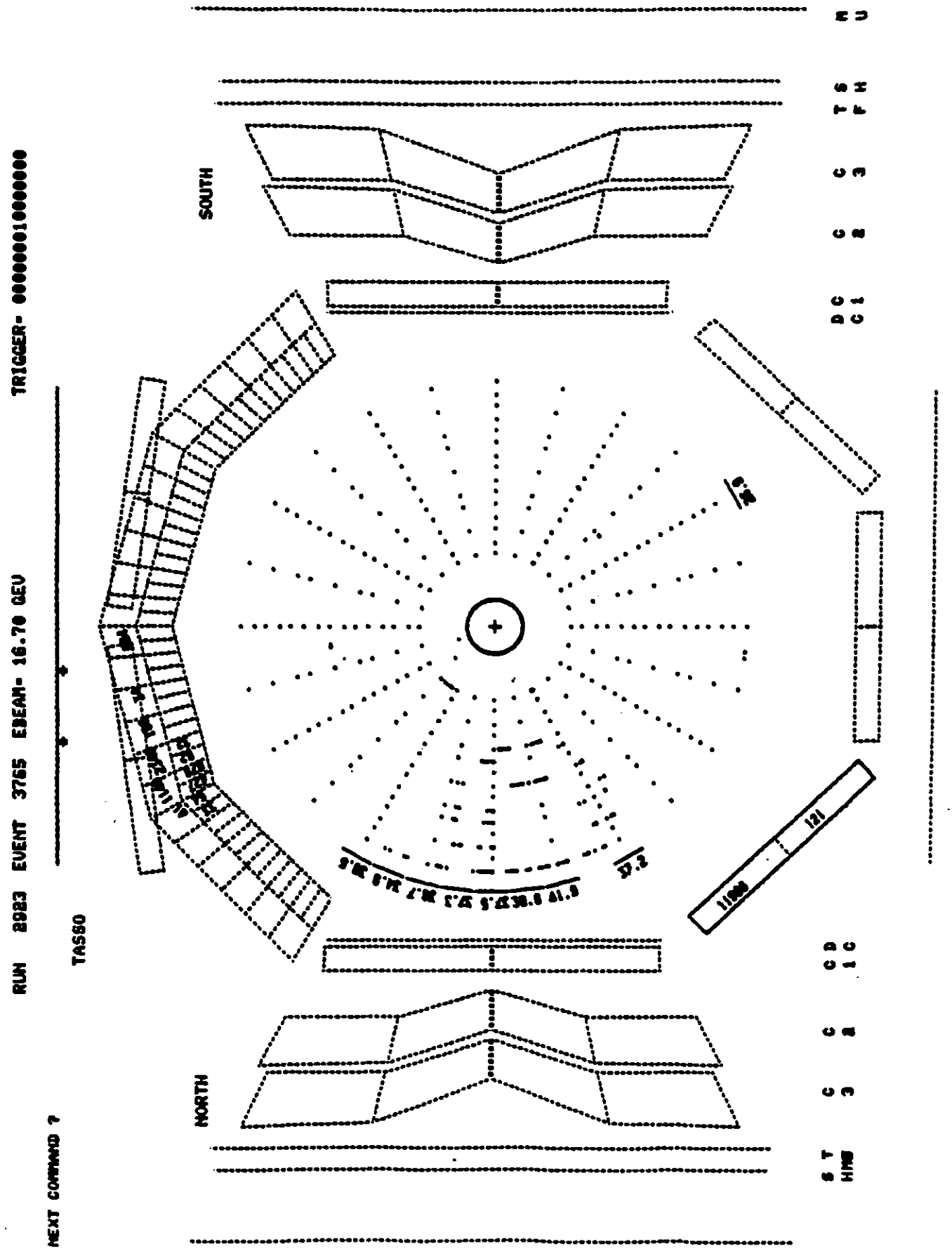
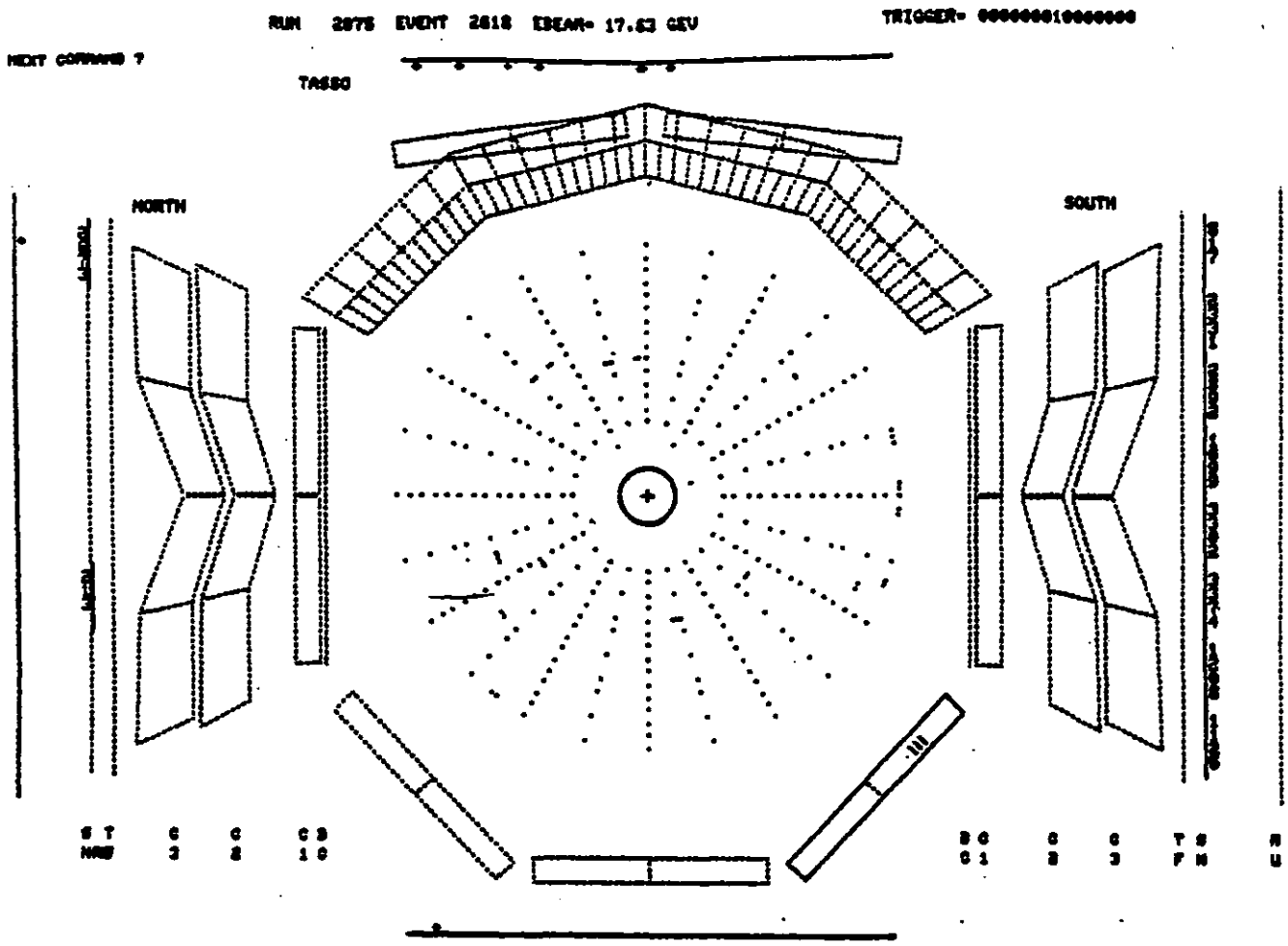


Fig 7·17 background event with a particle grazing the drift chamber



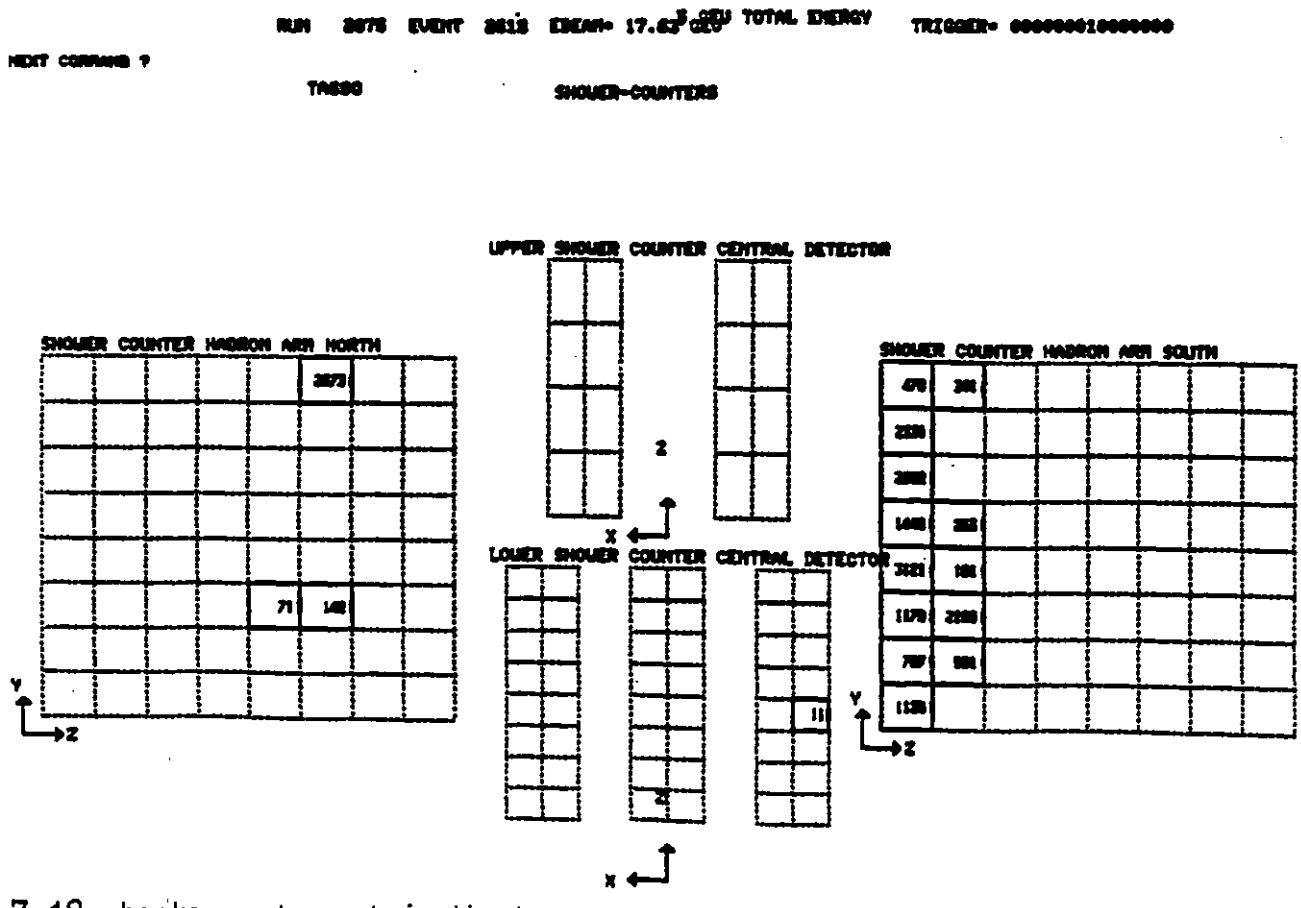


Fig. 7.18 background event in the hadron arms

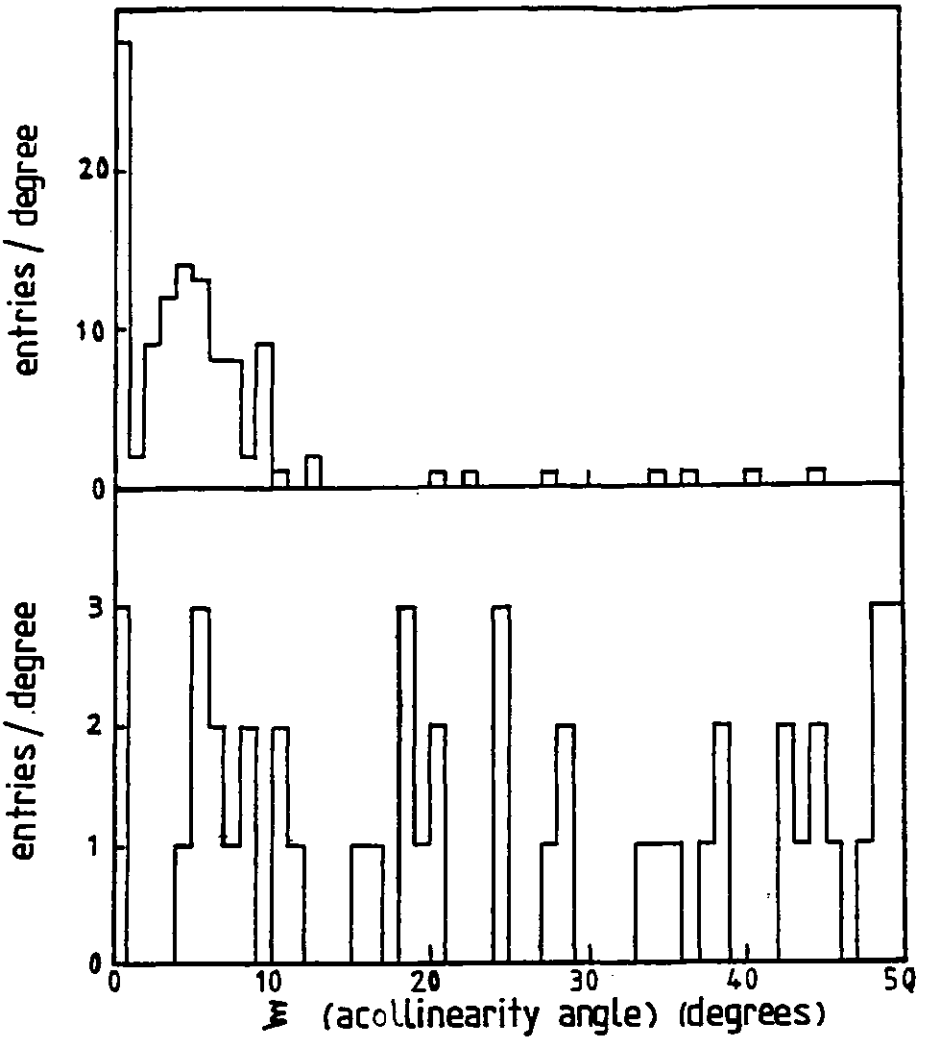


Fig 7·19 a) acollinearity angle distribution of class A events

b) acollinearity angle distribution of background events

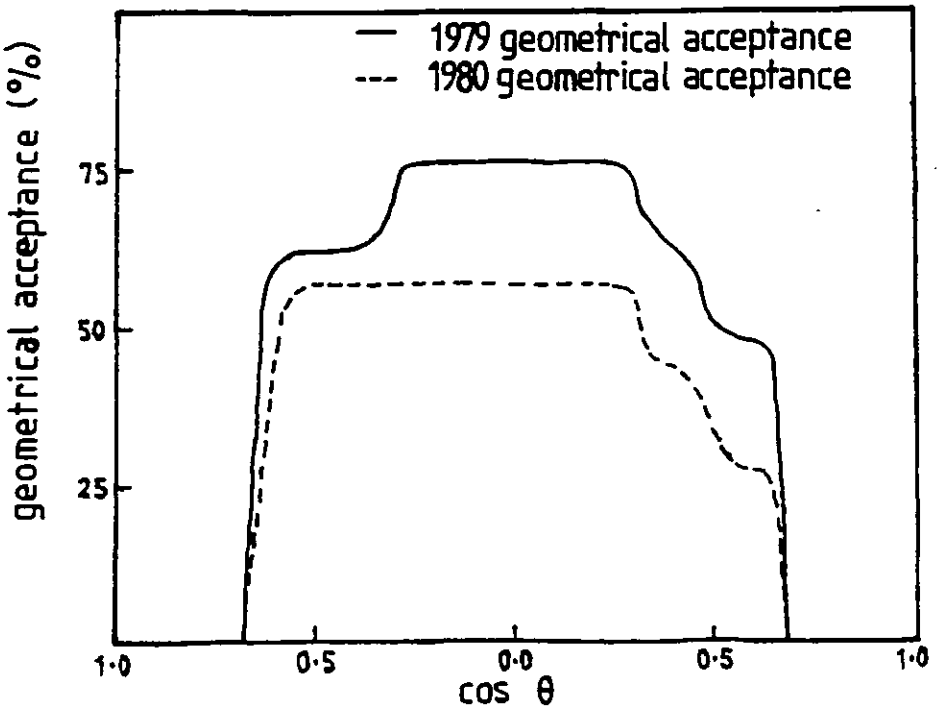


Fig 7·20 geometrical acceptance of the shower counters

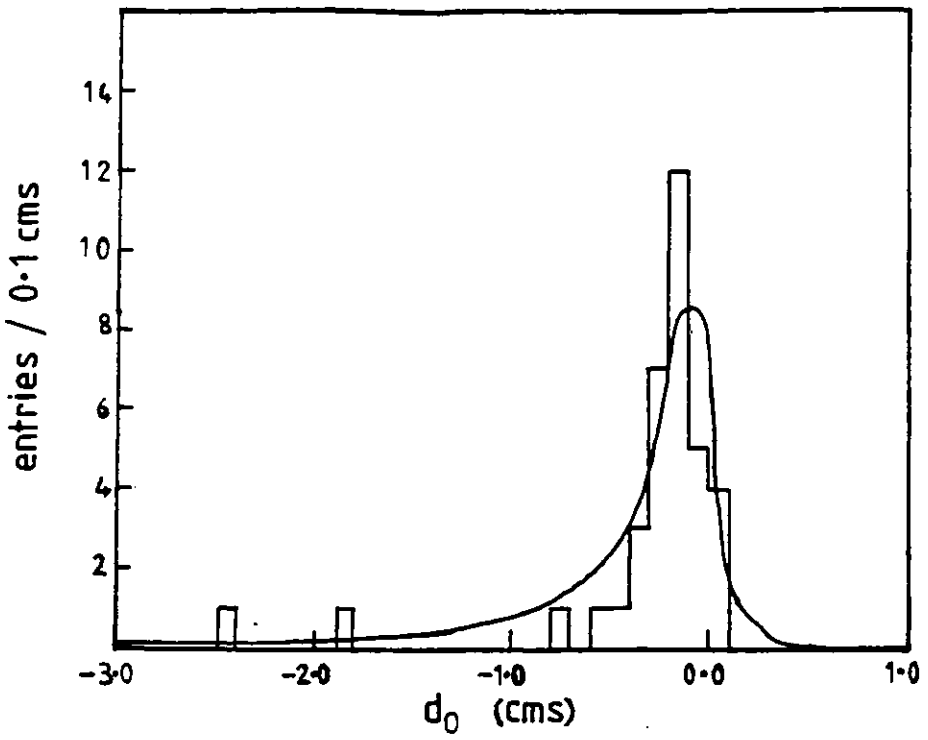


Fig 7·21 d_0 distribution of class B data (the solid curve is the Monte Carlo prediction)

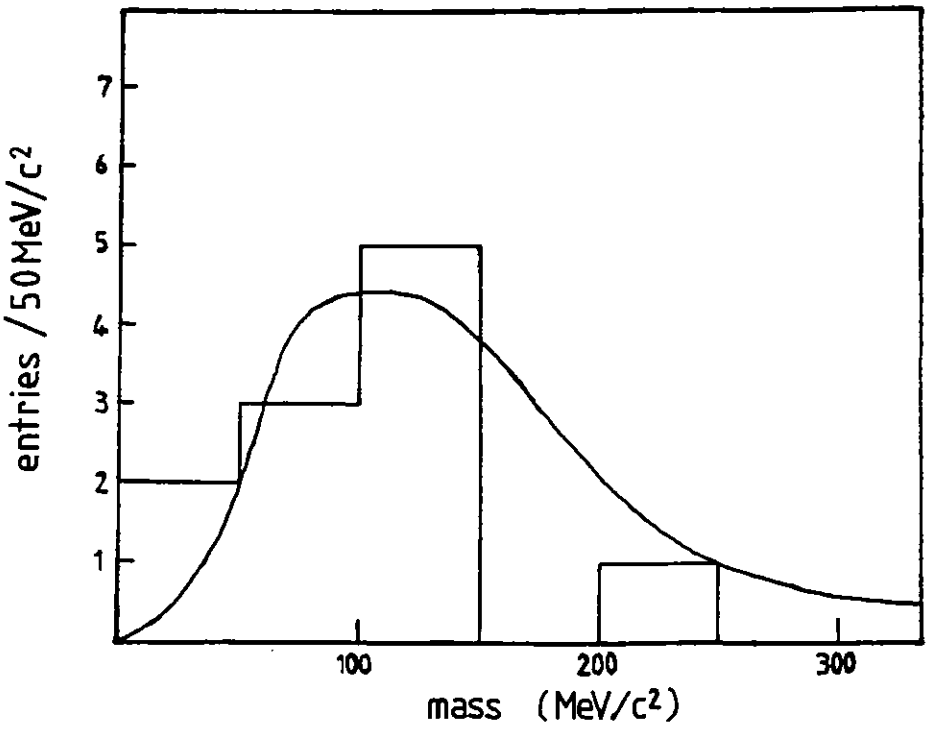


Fig 7·22 effective mass distribution of track pairs (the solid curve is the Monte Carlo prediction)

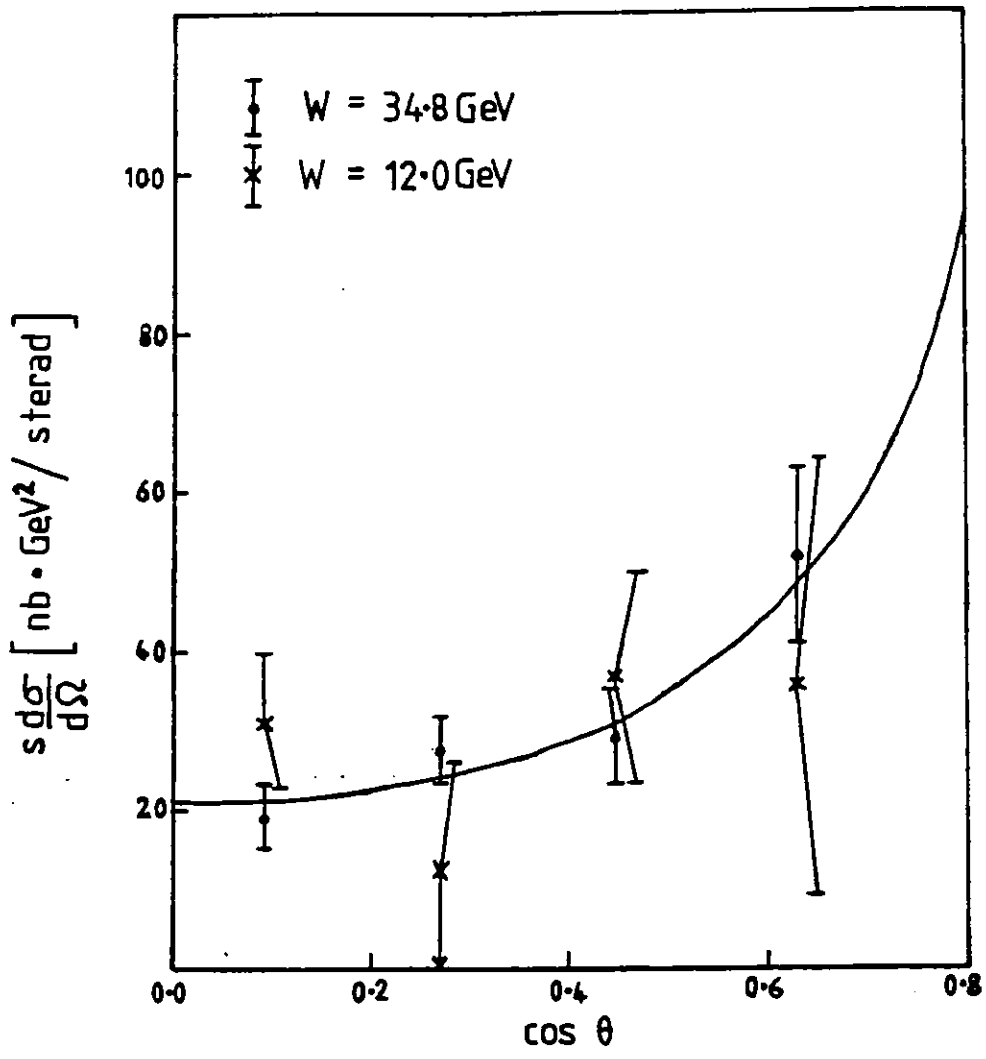


Fig 7·23 s dσ/dΩ v. cosθ for W = 12 GeV and W = 34.8 GeV (the solid curve is the prediction of QED)

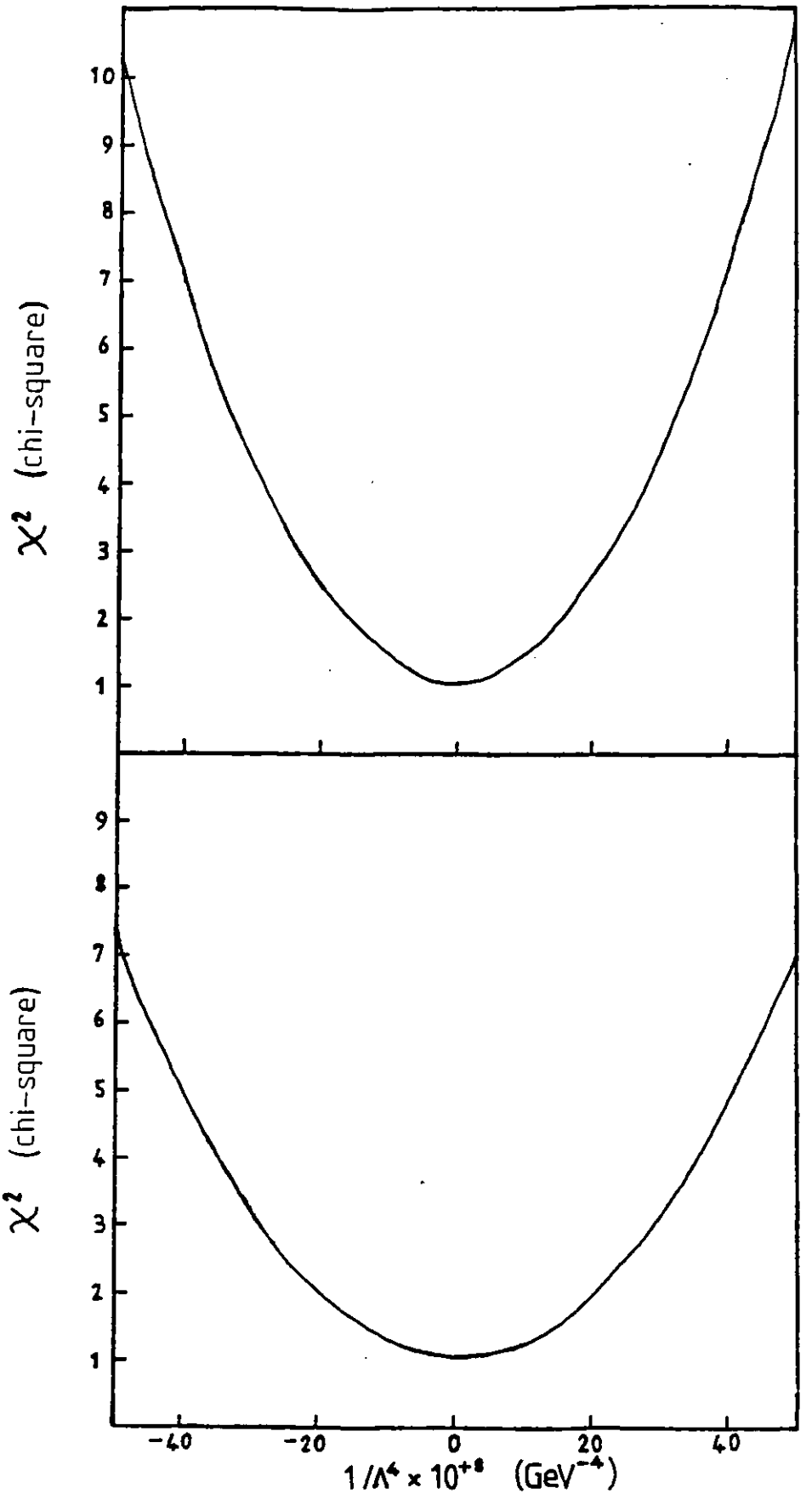


Fig 7·24 χ^2 v. $1/\Lambda^4$ a) heavy electron exchange
b) seagull diagram

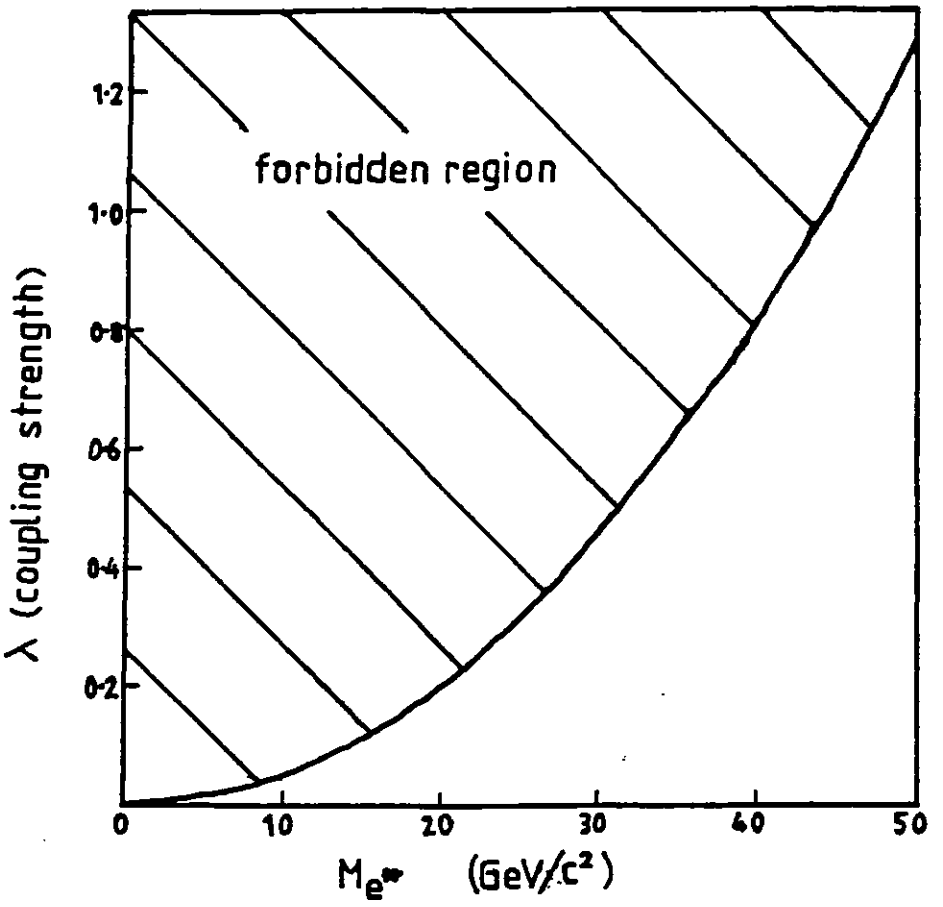


Fig 7·25 M_e^* v. λ (the shaded region is excluded at 95% confidence)

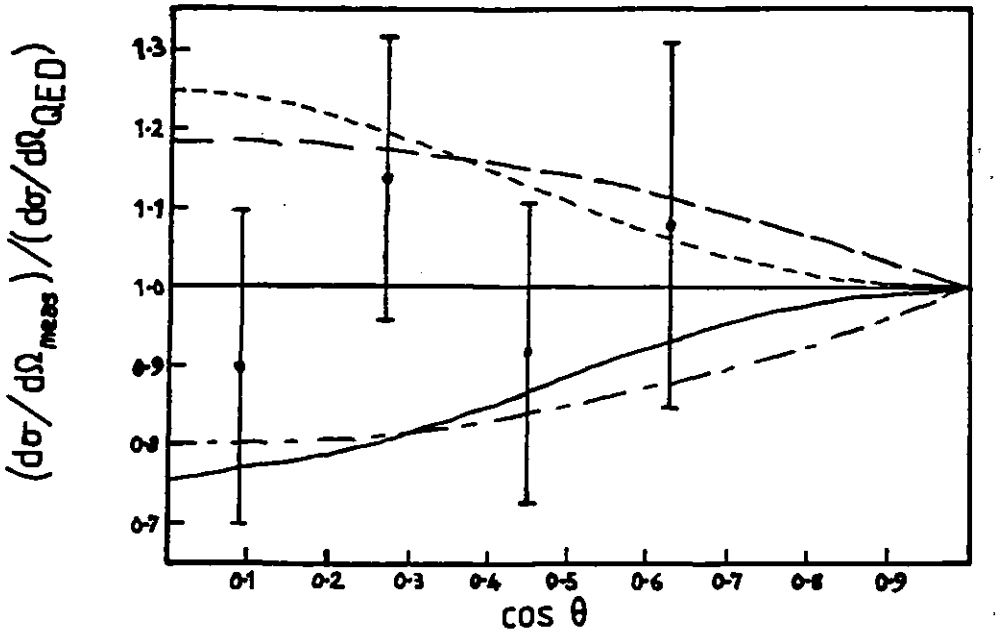


Fig 7·26 $(d\sigma/d\Omega_{meas})/(d\sigma/d\Omega_{QED})$ v. $\cos\theta$, the curves represent the modifications to QED for heavy electron exchange and the seagull diagram contribution at 95% confidence
(seagull, $\Lambda+$ ----, $\Lambda-$ —————)
(heavy electron, $\Lambda+$ — — —, Λ_- - - - -)

APPENDIX A

Simulation of electromagnetic showers

In this Appendix the procedures used to simulate the electromagnetic interactions of electrons and photons in the material before the drift chamber are described.

Photons are absorbed in matter as a consequence of the photoelectric effect, Compton scattering and pair production. In Compton scattering the photon is scattered with loss of energy while in the photoelectric effect and pair production the photon is completely absorbed. The photoelectric effect was not considered as for photon energies > 1 MeV it is negligible in comparison to the other two processes. Compton scattering was not simulated as it does not result in the production of a charged track observable in the drift chamber and for photon energies > 50 MeV it is much smaller than pair production.

The following method was adopted to treat pair production in the material before the drift chamber.

a) All photons with energy < 50 MeV were not considered.
At high photon energies the total pair production cross-section determines the absorbtion probability per radiation length, this rises rapidly from threshold (≃ 1 MeV) and approaches its asymptotic value of 7/9 for photon energies $\gtrsim$ 1 GeV.

b) In each layer the pair production probability per radiation length was given by the asymptotic form:

$$P = 1 - e^{-\frac{7}{9}\frac{x}{\sin\theta}} \qquad \text{- A.1}$$

where x is the layer thickness in radiation lengths and θ is the azimuthal angle of the photon. In the limit of complete nuclear screening the pair production cross-section is:[88]

$$\frac{d\sigma}{dp} = \frac{4\alpha r_o^2}{k}\left[\left(\frac{4V^2}{3} - \frac{4V}{3} + 1\right)\left[Z^2(L_{rad} - f) + ZL'_{rad}\right] - \frac{1V(1-V)(Z^2 - Z)}{9}\right] \qquad \text{- A.2}$$

where r_o is the radius of the electron, p is the positron energy, k is the photon energy, V is the ratio p/k, Z is the atomic weight of the radiator, f is the coulomb correction term and L_{rad},L'_{rad} are the radiation logarithms. The screening is complete if the following inequality is satisfied:

$$\gamma = \frac{100\, M_e\, Z^{-1/3}}{kv(1-v)} \ll 1 \qquad \text{- A.3}$$

At high photon energies k the screening is complete over a large range of the positron energy p.

Neglecting the coulomb correction term and substituting $L_{rad} = L'_{rad} = \ln(183Z^{-1/3})$ the probability for producing a positron of energy p per radiation length is:

$$P(p)dp = \frac{dp}{k}\left[\left(\frac{4V^2}{3} - \frac{4V}{3} + 1\right) - \frac{1}{9}\frac{V(1-V)}{\ln(183Z^{-1/3})}\right] \qquad \text{- A.4}$$

c) The energy of the positron was calculated using equation A.4 and the energy of the electron was calculated by energy conservation:

$$p_e = k - p \qquad \text{- A.5}$$

d) The direction cosines of the charged particles were defined by the direction cosines of the incident photon.

Electrons and positrons suffer electromagnetic interactions with both the atomic electrons and nuclei of the medium through which they pass which results in a loss of energy and a change in direction. For particle energies above a few MeV bremsstrahlung becomes the principle form of energy loss in the medium and dominates over the ionization loss. Only bremsstrahlung was considered when calculating the energy loss of electrons and positrons in the material before the drift chamber.

The following method was adopted to treat bremsstrahlung.

a) In each layer the bremsstrahlung probability per radiation length was given by:

$$P = 1 - e^{-\frac{x}{\sin\theta}} \qquad \text{- A.6}$$

where x is the layer thickness in radiation lengths and θ is the azimuthal angle of the particle. In the limit of complete nuclear screening the bremsstrahlung cross-section is:(88)

$$\frac{d\sigma}{dk} = \frac{4\alpha r_o^2}{k}\left[\left(\frac{4}{3} - \frac{4y}{3} + y^2\right)\left(Z^2(L_{rad} - f) + ZL'_{rad}\right) + \frac{1}{9}(1-y)(Z^2 + Z)\right] \qquad \text{- A.7}$$

where r_o is the radius of the electron, k is the photon energy, p_e is the electron energy, y is the ratio k/p_e, Z is the atomic weight of the radiator, f is the coulomb correction term and L_{rad}, L'_{rad} are the radiation logarithms. The screening is complete if the following inequality is satisfied:

$$\gamma = \frac{100\, M_e\, Z^{-1/3}\, y}{(1-y)p_e} \ll 1 \qquad \text{- A.8}$$

For high electron (positron) energies the screening is complete over a large range of the photon energy k.

Neglecting the coulomb correction and substituting $L_{rad} = L'_{rad} = \ln(183Z^{-1/3})$ the probability for radiating a photon of energy k per radiation length is:

$$P(k)dk = \frac{dk}{k}\left[\left(\frac{4}{3} - \frac{4y}{3} + y^2\right) + \frac{1}{9}\frac{(1-y)}{\ln(183Z^{-1/3})}\right] \qquad \text{- A.9}$$

b) The energy of the radiated photon was calculated using equation A.9 and the final momentum of the electron (positron) $\underline{p}_{ef}$ was calculated by momentum conservation

$$\underline{p}_{ef} = \underline{p}_e - \underline{p}_\gamma \qquad \text{A.10}$$

c) Only one interaction per layer of material was generated.

d) The direction of the radiated photon was defined by the direction cosines of the radiating electron (positron).

The angular distributions in pair production and bremsstrahlung are mostly determined by multiple coulomb scattering rather than the production mechanism. The angular distribution of the bremsstrahlung emission is peaked around a value $\theta = {}^{1}/_{\gamma} = M_e c^2/p_e$ and the average angle between the electron (positron) created in pair production is also $\theta \approx M_e c^2/k$.

Multiple coulomb scattering was treated in the following way. The resultant space angle ϕ compounded of a large number of small scatterings is approximately Gaussian with a mean square deflection given by:

$$\langle \phi^2 \rangle = \left(\frac{E_s}{p\beta c} \right)^2 t \qquad \text{- A.11}$$

where E_s = 21 MeV, p is the momentum of the particle, βc is the particle velocity and t is the material thickness in radiation lengths.

Equation A.11 was used to calculate the deflection, assuming a gaussian distribution, in each layer and the electron (positron) direction was redefined by rotating through this angle.

APPENDIX B

Photon reconstruction program

In this Appendix a program designed to identify the pair of charged tracks coming from the conversion of a photon in the material of the detector before the drift chamber is described.

The pair produced electron and positron appear as a 'V' with an extremely small angle between the tracks, the average angle θ between either of the tracks and the photon is $\theta \sim M_e c^2/E$, where M_e is the mass of the electron and E is the energy of the photon.

Photons were identified by a cut on the effective mass of each pair of oppositely charged tracks, as the effective mass of the e^+e^- pair produced by a photon conversion should be zero.

Track momenta were calculated by the track reconstruction program at the interaction point and not at the pair conversion point. To correctly calculate the effective mass of each track pair the momenta were recalculated at the conversion point, a process known as swimming. The conversion point was calculated by intersecting the pair of circles defined by the projection of the tracks in the R-ϕ plane. There are three possible cases which are shown diagramatically in Fig B.1 and each case was treated in a slightly different way.

For case a) where the tracks just touch the conversion point was defined as the point of contact. For case b) where the tracks do not intersect the track pair was rejected if, r_1, the distance between the circles at their closest point of intersection was greater than 2 cm. For accepted pairs the conversion point was defined to be the midpoint of the line r, which is shown in Fig B.1 b). Case c) where the tracks cross each other has two solutions which can in some cases be on either side of the interaction point. The solution closest to the interaction point was defined to be the conversion point unless it was behind the interaction point when the other solution was used.

The following method was used to determine if the intersection point was behind the interaction point. The angle α between the vector joining the intersection point and interaction point and the momentum vector of the track pair was calculated, this is shown diagramatically in Fig B.2. If α' is greater than $\pi/2$ then the intersection point is behind the interaction point.

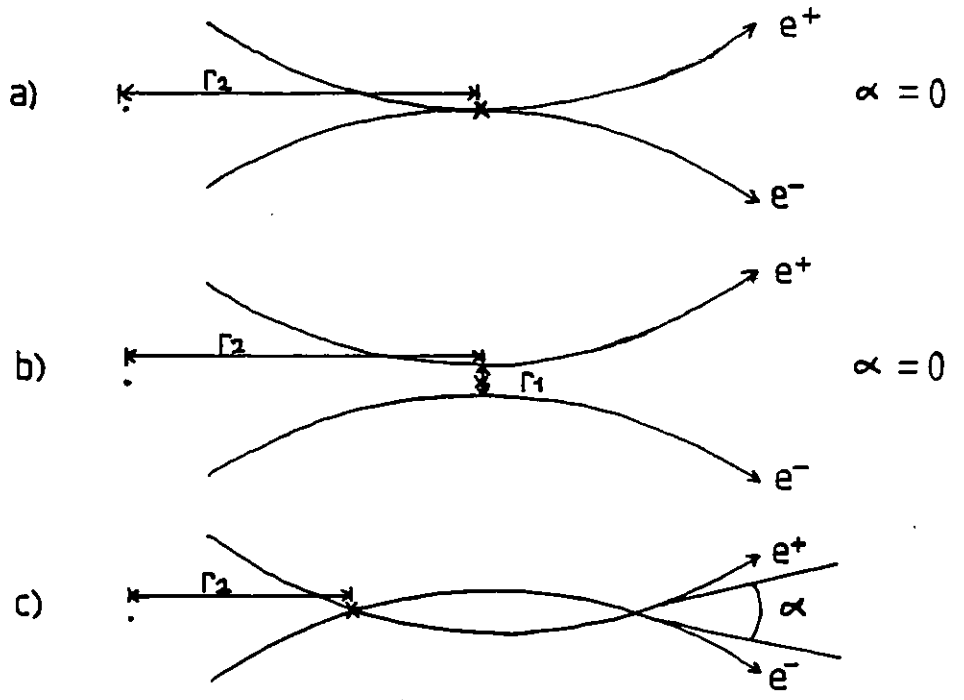
A number of cuts were applied to each solution before the effective mass was calculated.

The number of hits present before and the number of hits absent, up to six layers from the conversion point, was calculated for each track, with a tolerance of 2 cm allowed on the conversion point. The track pair was rejected if there were more than 4 hits missing after the vertex or more than 2 hits present before the vertex on either of the tracks. The radial distance, r_2, between the interaction point and the conversion point was required to be in the range $0 \leq r_2 \leq 45$ cm and the opening angle, α, between the tracks at the conversion point should satisfy $\alpha \leq 30°$. For case c) above, the second solution was considered if the first solution had been rejected by any cut provided that $\alpha' < \pi/2$ was satisfied. Using Monte Carlo events generated using the program described in section 7.8, 2% of track pairs were rejected by these cuts.

In all cases the z-coordinate of the conversion point was defined as the average value of the track z-coordinates at the intersection point.

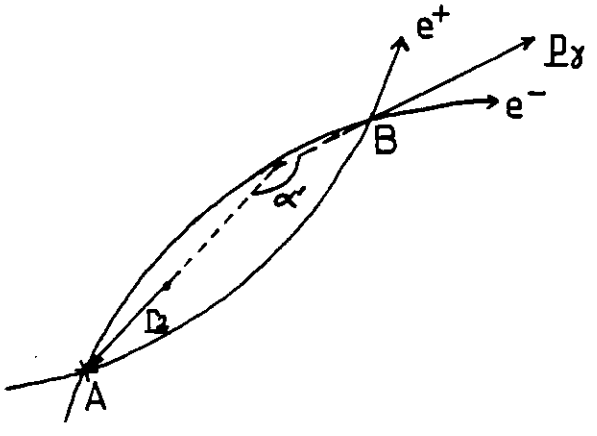
The effective mass of the track pair was then calculated at the conversion point for all remaining track pairs. The track pair was considered to come from a photon if the invariant mass of the pair was ≤ 250 MeV/c^2.

The effective mass of track pairs from the class B data set described in chapter 7, has been calculated using this program and is shown in Fig 7.22.



• = beam intersection point
α = opening angle
× = conversion point
r_1 = track separation
r_2 = distance to conversion point

Fig B·1 3 solutions for track intersections



• = beam intersection point
A and B are the two intersection points

Fig B·2 definition of the angle α', (in this case $\alpha' > \pi/2$ and solution B is defined to be the conversion point)

APPENDIX C

The TASSO collaboration

R. Brandelik, W. Braunschweig, K. Gather, V. Kadansky, F.J. Kirschfink, H.-U. Martyn, G. Peise, J. Rimkus, H.G. Sander, D. Schmitz, A. Schultz von Dratzig, D. Trines, W. Wallraff.
I. Physikalisches Institut der RWTH Aachen, Germany†

H. Boerner, H.M. Fischer, H. Hartmann, E. Hilger, W. Hillen, G. Knop, H. Kolanoski, P. Leu, R. Wedemeyer, N. Wermes, M. Wollstadt.
Physikalisches Institut der Universität Bonn, Germany†

H. Burkhardt, S. Cooper, D. Heyland, H. Hultschig, P. Joos, W. Koch, U. Kötz, H. Kowalski*, A. Ladage, D. Lüke, H.L. Lynch**, P. Mättig, K.H. Mess***, D. Notz, J. Pyrlik, D.R. Quarrie****, R. Riethmüller, A. Shapira*****, P. Söding, B.H. Wiik, G. Wolf.
Deutsches Elektronen-Synchrotron, DESY, Hamburg, Germany†

R. Fohrmann, M. Holder, H.L. Krasemann, G. Poelz, O. Römer, P. Schmüser.
II. Institut für Experimental physik der Universität Hamburg, Germany†

I. Al-Agil, R. Beuselinck, D.M. Binnie, A.J. Campbell, P.J. Dornan, D.A. Garbutt, T.D. Jones, W.G. Jones, S.L. Lloyd, D. Pandoulas, J.K. Sedgbeer, R.A. Stern, S. Yarker.
Department of Physics, Imperial College London, England††

M.G. Bowler, I.C. Brock, R.J. Cashmore, R. Devenish, P. Grossmann, J. Illingworth, M. Ogg, G.L. Salmon, J. Thomas, T.R. Wyatt, C. Youngman.
Department of Nuclear Physics, Oxford University, England††

K.W. Bell, B. Foster, J.C. Hart, J. Proudfoot, D.H. Saxon, P.L. Woodworth.
Rutherford Appleton Laboratory, Chilton, England††

E. Duchovni, Y. Eisenberg, U. Karshon, G. Mikenberg, D. Revel, E. Ronat.
Weizmann Institute, Rehovot, Israel†††

T. Barklow, J. Freeman+, T. Meyer++, G. Rudolph, E. Wicklund, S.L. Wu,
G. Zobernig.
Department of Physics, University of Wisconsin, Madison, Wisconsin, USA††††

* Now at CERN, Geneva, Switzerland

** On leave at UC Santa Barbara, USA

*** On leave from CERN, Geneva, Switzerland

**** On leave from Rutherford Appleton Laboratory, England

***** Minerva fellow, on leave from Weizmann Institute, Rehovot, Israel

\+ Now at FNAL, Batavia, USA

++ Now at A & M University, Texas, USA

† Supported by the Deutsches Bundesministerium für Forschung und Technologie

†† Supported by the UK Science and Engineering Research Council

††† Supported by the Minerva Gesellschaft für die Forschung mbH, München

†††† Supported in part by the US department of Energy contract WY-76-C-02-0881

REFERENCES

1. B.H. Wiik and G. Wolf, Springer Tracts in Modern Physics, 86 (1979); B.H. Wiik, Proc. 21st Scottish Univ. Summer School in Physics (1980); M.L. Perl SLAC-PUB-2615 (1980).
2. J. Perez-y-Jorba, Proc. 4th Int. Symp. on Electron and Photon Interactions at high energies, Liverpool (1969).
3. J.J. Aubert et al., Phys. Rev. Lett. 33, (1974) 1404.
4. J.E. Augustin et al., Phys. Rev. Lett. 33, (1974) 1406.
5. G.S. Abrams et al., Phys. Rev. Lett. 33, (1974) 1453.
6. Y. Hara, Phys. Rev. 134 (1964) B701; J.D. Bjorken and S.L. Glashow, Phys. Lett. 11, (1969) 265.
7. S.L. Glashow, J. Iliopoulos and L. Maiani, Phys. Rev. D2, (1970) 1285.
8. G. Goldhaber et al., Phys. Rev. Lett. 37, (1976) 255; R. Brandelik et al., Phys. Lett. 70B, (1977) 132 and Phys. Lett. 80B, (1979) 412.
9. M. Perl et al., Phys. Rev. Lett. 35, (1975) 1489.
10. S.W. Herbet et al., Phys. Rev. Lett. 39, (1977) 252; W.R. Innes et al., Phys. Rev. Lett. 39, (1977) 1240.
11. Ch. Berger et al., Phys. Lett. 76B, (1978) 243; C.W. Darden et al., Phys. Lett. 76B, (1978) 246; J.K. Bienlein et al., Phys. Lett. 78B, (1979) 360.
12. K. Berkelman, Proc., XX Int. Conf. on High Energy Physics, Madison (1980) p.1499.
13. R.F. Schwitters et al., Phys. Rev. Lett. 35, (1975) 1320; G. Hanson et al., Phys. Rev. Lett. 35, (1975) 1609.
14. B.H. Wiik, Proc. Int. Neutrino Conf., Bergen (1979); P. Söding, Proc. EPS Int. Conf. on High Energy Physics, Geneva (1979); R. Brandelik et al., Phys. Lett. 83B (1979) 261.

15. R. Brandelik et al., Phys. Lett. 97B, (1980) 453.

16. H. Fritzsch, M. Gell-Mann and H. Leutwyer, Phys. Lett. 47B (1973) 365; D.J. Gross and F. Wilczek, Phys. Rev. Lett. 30, (1973) 1343; H.D. Politzer, Phys. Rev. Lett. 30, (1973) 1346; S. Weinberg, Phys. Rev. Lett. 31, (1973) 31.

17. D. Cords, Proc. XX Int. Conf. on High Energy Physics, Madison (1980) p.590.

18. R. Brandelik et al., DESY 81/005 (1981).

19. G. Flügge, Zeit. Phys. C1, (1979) 121; M.L. Perl, Ann. Rev. Nucl. Part. Sci. 30, (1980) 299.

20. D.P. Barber et al., Phys. Rev. Lett. 45, (1980) 1904; R. Brandelik et al., Phys. Lett. 99B (1981) 163 and DESY 82/032 (1982); Ch. Berger et al., DESY 81/001 (1981); H.-J. Behrend et al., DESY 82/021 (1982).

21. L. Paoluzi et al., Lett. al Nuovo Cimento 10 (1974) 435.

22. H.J. Besch et al., Phys. Lett. 81B, (1979) 79; G.S. Abrams et al., Phys. Rev. Lett. 43, (1979) 477.

23. F.F. Low, Phys. Rev. 120, (1960) 582; F. Calogero and C. Zemach, Phys. Rev. 120, (1960) 1860.

24. Ch. Berger et al., Phys. Lett. 94B (1980) 254; C.J. Biddick et al., Phys. Lett. 97B, (1980) 320; A. Roussarie, Proc. XX Int. Conf. on High Energy Physics, Madison (1980) p.573; R. Brandelik et al., DESY 81/026 (1981).

25. Ch. Berger et al., Phys. Lett. 89B, (1979) 120; E. Hilger, Springer Lecture Notes in Physics 134, (1980); Ch. Berger et al., Phys. Lett. 99B, (1981) 287.

26. R. Brandelik et al., Phys. Lett. 97B, (1980) 448.

27. W. Wagner, Proc. XX Int. Conf. on High Energy Physics, Madison (1980) p.576.

28. R. Hofstadter, Proc. Int. Symp. on Lepton and Photon Interactions at High Energies, Stanford (1975) p.869; F.H. Combley, Proc. Int. Synp. on Lepton and Photon Interactions at High Energies, Stanford (1975) p.913.

29. R.S. Van Dyck et al., Phys. Rev. Lett. 38 (1977) 310.

30. J. Bailey et al., Nucl. Phys. B150 (1979) 1.

31. W. Barber, B. Gittelman, G.K. O'Neill, B. Richter, Phys. Rev. Lett. 16 (1966) 1127.

32. J.E. Augustin et al., Phys. Rev. Lett. 34, (1975) 233; T. Himel et al., Phys. Rev. Lett. 41, (1978) 449; L.H. O'Neill et al., Phys. Rev. Lett. 37 (1976) 395; B.L. Beron et al., Phys. Rev. D17, (1978) 2187 and Phys. Rev. D17 (1978) 2839; R. Brandelik et al., Z-Phys. C1, (1979) 233.

33. P. Dittmann and V. Hepp, DESY 81/030 (1981).

34. S.L. Glashow, Nucl. Phys. 22 (1961) 579; A. Salam, Phys. Rev. 127 (1962) 331; S. Weinberg, Phys. Rev. Lett. 19 (1967) 1264.

35. P. Duinker, DESY 81/012 (1981).

36. J.G. Branson, DESY 81/073 (1981); R. Marshall, RL-82-029 (1982).

37. H. Georgi and S. Weinberg, Phys. Rev. D17, (1978) 275; J.D. Bjorken, Phys. Rev. D19, (1979) 335.

38. V. Barger, W.Y. Keung and E. Ma, Phys. Rev. Lett. 44, (1980) 1169; E.H. de Groot and D. Schildknecht, Phys. Lett. 95B (1980) 128.

39. N. Wright and J.J. Sakuri, Phys. Rev. D22, (1980) 220.

40. C. Jarlskog and F.J. Yndurain, Phys. Lett. 63B, (1976) 215.

41. R. Budny, Phys. Lett. 55B, (1975) 227.

42. N.M. Kroll, Nuovo Cim. 45A (1966) 65.

43. A. Litke, Harvard University, Ph.D. Thesis (1970), unpublished.

44. M. Capdequi-Peyranere et al., Montpellier PM/78/8 (1978) and PM/80/9 (1980); F.M. Renard, CERN TH.3244 (1982).

45. PETRA proposal, DESY, Hamburg (November 1974); PETRA proposal (updated version), DESY, Hamburg (February 1976).

46. TASSO proposal, DESY PRC-76/14 (1976); Addendum to the TASSO proposal, TASSO Note 8 (1977).

47. C. Youngman, Ph.D. Thesis, University of London (1980), RL-HEP/T/82.

48. H. Boerner et al., NIM 176 (1980) 151; H. Boerner, Ph.D. Thesis, University of Bonn (1981), BONN-IR-81-27.

49. D. Heyland, Ph.D. Thesis, University of Hamburg (1981), DESY (Internal Report) F1-81/01.

50. R. Brandelik et al., DESY 81/069 (1981).

51. M. Ogg, Ph.D. Thesis, University of Oxford (1981), RL-HEP/T/89.

52. W. Hillen, Ph.D. Thesis, University of Bonn (1981), BONN-IR-81-7.

53. J.F. Crawford et al., NIM 127, (1975) 173.

54. V. Kadansky et al., Physica Scripta 23 (1981) 680.

55. H. Burkhardt et al., DESY 80/100 (1980).

56. K.W. Bell et al., NIM 179 (1981) 27.

57. H. Frese et al., IEEE Trans. Nucl. Sci. NS24 (1977) 1792.

58. D.J. White, RL-80-006 (1980).

59. S. Jarowslavski, NIM 176 (1980) 263.

60. D.R. Quarrie, RL-81-048 (1981).

61. V. Blobel, DESY (Internal Report), F14-79/02 (1979).

62. D.G. Cassel and H. Kowalski, DESY 80/107 (1980).

63. G. Mikenberg, TASSO Note 17 (1977); Addendum to Proposal 190 (TASSO), RL-PPESP 190 (1977).

64. G. Mikenberg, Private Communication.

65. W.A. Shurcliff, J. Opt. Soc. of America 41 (1951) 209.

66. R.L. Garwin, Rev. Sci. Instr. 31 (1960) 1010.

67. G. Keil, Jour. App. Phys. 40 (1969) 3544; G. Keil, NUM 83 (1970) 145 and NIM 89 (1970) 111.

68. W.B. Atwood et al., SLAC-TN-76-7 (1976); B. Barish et al., CALT 68-623 (1977); W. Selove et al., NIM 161 (1979) 233.

69. Manufactured by POLIVAR, Italy.

70. Manufactured by ROHM, Germany.

71. H.P. Klasen, Diplomarbeit, University of Dortmund (1978).

72. R.L. Ford and W.R. Nelson, SLAC-210 (1978).

73. J.C. Hart, RL-79-064 (1979).

74. U. Karshon, Private Communication.

75. F.A. Berends, K.J.F. Gaemers and R. Gastmans, Nucl. Phys. B63 (1973) 381; and Nucl. Phys. B68 (1974) 541; F.A. Berends and R. Kleiss, DESY 80/66 (1980); Bhabha event generator provided by F.A. Berends and R. Kleiss.

76. F.A. Berends and G.J. Komen; Phys. Lett. 63B, (1976) 432.

77. R. Hofstadter, Proc. Int. Symp. on Lepton and Photon Interactions at High Energies, Stanford (1975) p.869.

78. Particle Data Group, Rev. Mod. Phys. 52 (1980) No. 2, Part II.

79. J.A.M. Vermaseren, Private Communication.

80. C. Youngman, Private Communication.

81. S.L. Lloyd and B. Foster, Private Communication.

82. S. Cooper, Private Communication.

83. F.A. Berends and R. Gastmans, Nucl. Phys. B61, (1973) 414; F.A. Berends and R. Kleiss, DESY 80/122 (1980).

84. F.E. Low, Phys. Rev. Lett. 14 (1965) 238.

85. J.A. McClure and S.D. Drell, Nuovo Cim. 37, (1965) 1638.

86. Y. Takahashi, Nuovo Cim. 6, (1957) 371.

87. F.E. Low, Phys. Rev. 110, (1958) 974.

88. Y.S. Tsai, Rev. Mod. Phys. 46, (1974) 815.

ACKNOWLEDGEMENTS

I thank all the members of the TASSO collaboration for the continuing success of this experiment especially Dr. G. Mikenberg for explaining the intricacies of the shower counter analysis program to me.

I am indebted to my supervisor Dr. D.A. Garbutt for his encouragement and friendly advice. My thanks also to Dr. P.L. Woodworth for reading the draft of this thesis.

I also wish to thank Professor I. Butterworth for the opportunity of working in the High Energy Physics Group at Imperial College and the DESY Directorium for their hospitality during my stay at DESY.

The Science Research Council provided financial support for a period of three years.

Finally I thank Kathy Thompson for her excellent typing of this thesis.